Origin of the enhancement of tunneling probability in non-integrable systems

Yasutaka Hanada

Department of Physics,
Tokyo Metropolitan University

Thesis submitted for the degree of Dector of Philosophy in Physics

2015

Abstract

Chaos-assisted tunneling and resonance-assisted tunneling have been proposed and well recognized as mechanisms to explain the enhancement of tunneling probability in nonintegrable systems. In both mechanisms, quantum resonance plays a key role. In this thesis, we revise and reconsider of quantum tunneling in nonintegrable systems in particular to explore the origin of enhancement of the tunneling probability by studying quantum maps whose corresponding classical phase space is nearly integrable. For this purpose, we introduce renormalized integrable Hamiltonians and examine the nature of eigenfunctions under such bases. We found that, in addition to the enhancement due to quantum resonances, the persistent enhancement appears as a result of nontrivial broad couplings of a reference state with states whose supports lie around the unstable fixed points and associated separatrix in classical phase space. We also clarified that the successive switching of dominant contributors, which is linked to the fundamental frequency of the external driving force, gives rise to the staircase structure of the tunneling probably typically observed in tunneling splitting. On the basis of these investigations, we claimed that essential differences exist in the nature of tunneling between completely integrable and nonintegrable systems.

Contents

1 Introduction **1**

2 Classical and quantum dynamics **5**

2.1 Classical mechanics 5

2.2 Classical dynamics of kicked Hamiltonian 10

2.3 Quantum dynamics of kicked Hamiltonian 12

3 Theory of tunneling splitting **19**

3.1 Tunneling splitting in the double well system 20

3.2 Resonance-assisted tunneling 26

3.3 Resonance-assisted tunneling in the integrable system 32

4 Tunneling effect in non-integrable systems **41**

4.1 Natural boundaries and tunneling effect 41

4.2 Instanton-noninstanton transition 46

5 Origin of the enhancement of tunneling probability in the nearly integrable system **57**

5.1 Enhancement of tunneling probability 58

5.1.1 Resonance spikes and the third states 62

5.2 Staircase structure with resonance spikes 65

5.2.1 Absorbing operator 65

5.2.2 Staircase structure 69

5.3 Mechanism generating the staircase structure 70

5.3.1 Instanton-noninstanton transition 71
5.3.2 Anomaly of eigenfunctions in the action representation 78
5.4 Splitting curves in integrable systems 84

6 Summary and outlook **89**

Appendix A Absorbing operator for quantum map **95**
A.1 Time evolution with absorbing operator 95
A.2 Eigenvalue problem with absorbing operator 100
A.3 The relation between the decay rate and tunneling splitting 105

Appendix B Symplectic integrator for Hamiltonian systems **109**

Acknowledgements **117**

Chapter 1

Introduction

The penetration of wave function through classically forbidden regions is referred to as quantum tunneling. As explained in standard textbooks on quantum dynamics, quantum tunneling is peculiar to quantum mechanics and no counterparts exist in classical mechanics. Nevertheless, it is known that describable in terms of classical mechanics if it is extended to the complex space. Such complexified classical path is called *instanton*. For more than one-dimensional Hamiltonian systems, however, the nature of classical dynamics is completely different from the one-dimensional one. An essential difference in classical dynamics between one- and multi-dimensional systems is the following: in the former case, the classical dynamics at most shows regular behaviors such as periodic or ballistic motions. But in the latter case, in generic situations, the system is nonintegrable and so the classical dynamics exhibits not only (quasi-)periodic but also chaotic motions which are unpredictable despite the deterministic dynamics. The phase space is a mixture of regular and chaotic components and each component plays the role of barrier since the orbits contained in the regular region are not allowed to transit to chaotic regions and vice versa. Therefore such barriers inherent in multidimensional nature is called *dynamical barriers*. The penetration of the wave packet through dynamical barriers is referred to as *dynamical tunneling* [Davis and Heller 1981]. It has been reported that the tunneling probability in multi-dimensional systems exhibiting chaotic motions is enhanced compared with one-dimensional one. The study of dynamical tunneling is one of the central issues in multi-dimensional quantum systems [Keshavamurthy and Schlagheck 2011].

There are several pioneering works on quantum tunneling in nonintegrable systems, and roughly divided

into two directions. The first direction is to investigate the nature of tunneling in stationary quantum states, that is, to examine the eigenstates. The first scenario concerns how chaos comes into play in the tunneling process. A simplest situation would be, for example, a doublet appearing in the system with symmetric double well potential, and suppose that chaos exists between the states supporting the both wells. As one varies an external parameter of the system, it can happen that states forming the doublet and a state supported by the chaotic region come close to each other in the energy space and form avoided crossing. Within the interaction regime, the energy splitting between the doublet becomes large through couplings with the chaotic state, meaning that the tunneling amplitude between one torus to the other is enhanced. *Chaos-assisted tunneling* (CAT) occurs in this way [Bohigas et al. 1993b, Tomsovic and Ullmo 1994]. A similar mechanism would work if the doublet interacts with the state supported by classical nonlinear resonances, which are also important ingredients in multi-dimensional phase space. The latter mechanism is called *resonance-assisted tunneling* (RAT) [Brodier et al. 2001; 2002]. They both would be reasonable scenarios for quantum tunneling in nonintegrable systems, but there is a lack of direct evidence showing that chaos or nonlinear resonances certainly gives rise to the enhancement of tunneling because there are no semiclassical analyses, which are to date supposed to a unique tool to bridge classical and quantum phenomena, behind their arguments.

The second direction is to investigate quantum tunneling in the time domain, and developed in a serious of works [Shudo and Ikeda 1994; 1995; 1998, Shudo et al. 2009a;b]. A big advantage in the time domain approach is that one can employ the semiclassical method, by which the role of chaos and other classical phase space objects can directly be linked to quantum mechanics. They indeed discovered that chaos in complex plane, which manifests itself especially as the Julia set in cases of discrete dynamical systems, controls the tunneling process in nonintegrable systems. A disadvantage of the time domain analysis is, on the other hand, that there remains initial and final condition dependence in the description and so it is not suitable to develop a canonical argument.

Energy and time domain approaches both imply the enhancement of tunneling, certainly originating from nonintegrability of the system, but the issue is not yet settled although more than 20 years have passed since such a question was first addressed. A main technical obstacle is that there exists no energy-domain semiclassical formulation, as derived in strongly chaotic systems, but lack of our understanding for classical mixed phase space is also a source of slow progress of this issue.

In this thesis, we focus on the enhancement of the tunneling probability as a function of Planck's constant as discussed in RAT and revisit the origin of such enhancement from a different standpoints of RAT. In the following, we will examine the tunneling probability by evaluating tunneling splitting. Note however that there is no legitimate way or one should even say that providing a proper definition for the tunneling probability itself is an issue to be explored in nonintegrable systems.

As is well known [Brodier et al. 2002, Roncaglia et al. 1994], in nonintegrable systems, the tunneling splitting as a function of Planck's constant becomes large as several or several tens of magnitude compared with integrable one, and splitting curves typically form characteristic structures: plateaus and spikes. According to RAT theory, the plateau structure is consider to be a result of accumulation of quantum resonance and a bunches of spikes is interpreted as the origin of the enhancement of the tunneling probability [Mouchet et al. 2006, Schlagheck et al. 2011].

Our strategy to explore the origin of enhancement is as follows. First, in order to see how quantum energy resonances are related to the appearance of plateau structures, we introduce a local absorbing potential to suppress the effect of quantum resonance in the splitting curve. Our results show that the spikes in the splitting curve disappear, but plateaus and associated staircase structures still remain. This implies that the quantum resonance does not play a key role in the enhancement of tunneling probability. Knowing that the staircase does not appear in completely integrable systems, one expects that the staircase structure is unique in non-integrable systems.

Next, we develop renormalized approximation method to clarify the nature of tunneling couplings. Our motivation to consider renormalization approximation is to identify remainder effects due to nonintegrability as sharp as possible, and to see whether the observed enhancement has a truly nonintegrability origin. Our analysis reveals that tunneling components are composed of two characteristic ones; the one essentially attributable to instanton and the other ones, which represent highly nontrivial broad couplings with the states supported by classical unstable periodic points and associated separatrix. We find that the switching of the dominant contributor from instanton to broad components happens, which we call the instanton-noninstanton transition, and this invokes the enhancement. We further identify successive switching of dominant contributors, which is linked to the fundamental frequency of the external driving force, gives rise to the staircase structure of the tunneling. By closer looking at eigenfunctions under the basis of renormalized Hamiltonian, we further find that there appears an anomalous nature in tunneling tails, which would no

be reproduced by the leading order semiclassical approximation.

The organization of this thesis is as follows: In chapter 2, we will outline the classical and quantum dynamics in multi-dimensional Hamiltonian systems. In chapter 3, we will explain the tunneling splitting and review theory of resonance assisted tunneling and its semiclassical description for the integrable system. In chapter 4, we discuss some backgrounds of why quantum tunneling in nonintegrable systems can qualitatively be different from the integrable one by explaining the nature of classical invariant structures, especially the emergence of natural boundaries of invariant manifolds. Then we show the mechanism of the instanton-noninstanton transition by introducing renormalized approximation method. In chapter 5, we explore the origin of the tunneling probability in non-integrable systems. In chapter 6, we summarize this thesis and mention outlook for future works.

Chapter 2

Classical and quantum dynamics

Quantum mechanics reflects the corresponding classical mechanics, so classical mechanics is often used to understand quantum phenomena. However classical dynamics is not easy to understand when chaos appears. The aim of section 2.1 is a brief review of classical dynamics in non-integrable systems. In section 2.2, we introduce the classical map as a simple model of the chaotic systems . In section 2.3, we introduce the quantum map which is a quantized version of the associated classical map.

2.1 Classical mechanics

For the N-dimensional autonomous Hamiltonian system $H(\boldsymbol{p}, \boldsymbol{q})$, the time evolution of the system is described by the Hamilton's equations of motion

$$\dot{p}_i = -\frac{\partial H}{\partial q_i}, \qquad \dot{q}_i = \frac{\partial H}{\partial p_i}, \tag{2.1}$$

where $\boldsymbol{q} = (q_1, \cdots, q_N)$ and $\boldsymbol{p} = (p_1, \cdots, p_N)$ denote the generalized coordinates and conjugated momenta, respectively. The phase space trajectory of the Hamilton's equations of motion is confined in a $2N - 1$ dimensional subspace since the total energy of the autonomous Hamiltonian systems is a constant

of motion:

$$\begin{aligned}\frac{d}{dt}H &= \sum_{i=1}^{N}\left(\frac{\partial H}{\partial q_i}\frac{dq_i}{dt}+\frac{\partial H}{\partial p_i}\frac{dp_i}{dt}\right)\\ &= \sum_{i=1}^{N}\left(\frac{\partial H}{\partial q_i}\frac{\partial H}{\partial p_i}-\frac{\partial H}{\partial p_i}\frac{\partial H}{\partial q_i}\right)=0.\end{aligned}$$

The Hamilton equations (2.1) are written as

$$\frac{d}{dt}z = \{z, H\}, \tag{2.2}$$

where we write a set of canonical variable as $z = (\boldsymbol{p}, \boldsymbol{q})$, and $\{,\}$ denotes the Poisson bracket given as

$$\{g, h\} = \sum_{i=1}^{N}\left(\frac{\partial g}{\partial q_i}\frac{\partial h}{\partial p_i}-\frac{\partial g}{\partial p_i}\frac{\partial h}{\partial q_i}\right), \tag{2.3}$$

where g and h are some function of $(\boldsymbol{q}, \boldsymbol{p})$. If a function $\Phi(\boldsymbol{p}, \boldsymbol{q})$ is conserved under the time evolution, *i.e.*,

$$\frac{d}{dt}\Phi = \{\Phi, H\} = 0, \tag{2.4}$$

the function Φ is also called a constant of motion. If the system has independent N constants of motion, $\Phi_1, \cdots, \Phi_N$, which are functionally independent with each other and Poisson commutable, then the Hamilton's equation are integrable within quadrature and such a system is called as the completely integrable system. For the completely integrable system, there is a canonical transformation from $(\boldsymbol{q}, \boldsymbol{p})$ to action-angle variables $(\boldsymbol{I}, \boldsymbol{\theta})$ and the new Hamiltonian depends only on action variables $\boldsymbol{I}$ [Arnold, Lichtenberg and Lieberman, Reichl, Tabor, Onuki and Yoshida]. Then, the equations of motion are rewritten as

$$\frac{d}{dt}\theta_i = \Omega_i(\boldsymbol{I}), \qquad \frac{d}{dt}I_i = 0, \tag{2.5}$$

where $\Omega_i \equiv \frac{\partial H}{\partial I_i}$ is the intrinsic frequency of the Hamiltonian $H(\boldsymbol{I})$. The theorem of Arnold has shown that the motion described by Eq. (2.5) is at most quasi-periodic on the N-dimensional tours in $2N$-dimensional phase space [Arnold, Lichtenberg and Lieberman, Reichl, Tabor, Onuki and Yoshida].

As was suggested by [Poincaré 1892], completely integrable systems are exceptional and generic Hamil-

tonians do not have enough constants of motion. In generic Hamiltonian systems, the solution of Hamilton's equation shows not only quasi-periodic motions but also chaotic motions.

To illustrate chaotic dynamics, we consider the two-dimensional Hamiltonian [Creagh 1998]

$$H(q_1, q_2, p_1, p_2) = \frac{1}{2}(p_1^2 + p_2^2) + V(q_1, q_2), \tag{2.6}$$

where the potential function is given by

$$V(q_1, q_2) = (q_1^2 - 1)^2 + q_2^2 + \varepsilon q_1^2 q_2^2. \tag{2.7}$$

The potential function has two local minima at $(q_1, q_2) = (\pm 1, 0)$ with energy $E = 0$ and a local maximum at the potential saddle point $(q_1, q_2) = (0, 0)$ with energy $E = 1$. When $\varepsilon = 0$, the Hamiltonian (2.6) is separable

$$H(q_1, q_2, p_1, p_2) = H_1(q_1, p_1) + H_2(q_2, p_2), \tag{2.8}$$

where

$$H_1(q_1, p_1) = \frac{p_1^2}{2} + (q_1^2 - 1)^2, \qquad H_2(q_2, p_2) = \frac{p_2^2}{2} + q_2^2. \tag{2.9}$$

Since the Hamiltonian (2.8) is completely integrable, the flow of classical dynamics is confined on two dimensional tori in phase space with frequencies $\mathbf{\Omega} = (\Omega_1, \Omega_2)$, where Ω_i $(i = 1, 2)$ denotes intrinsic frequencies along the angle coordinate defined by Eq. (2.5). If the trajectory satisfies the resonance condition, $\Omega_1/\Omega_2 = r/s$, where r, s are an integer values, the tours is called *resonant tours*. On the other hand, the tours is called *off-resonant tours*, if each frequency is incommensurable.

For $\varepsilon > 0$, the Hamiltonian (2.6) is no longer integrable, the nature of classical dynamics may drastically change. A typical aspect is illustrated in Fig. 2.1. Figures 2.1(a) and (b) show different types of trajectories in configuration space (q_1, q_2), where we give the energy $E = 3/2$ and use different initial conditions for each trajectory. When the energy of classical trajectory is greater than the potential saddle energy $E_{\rm sad} = 1$, it may seem like that the trajectories can freely move between left $(q_1 < 0)$ and right $(q_1 > 0)$ wells. As shown in Fig. 2.1(a), however, the classical dynamics shows a quasi-periodic motion and confines the trajectory to one side of the wells. On the other hand, the trajectory in Fig. 2.1(b) goes back and forth between both wells at random.

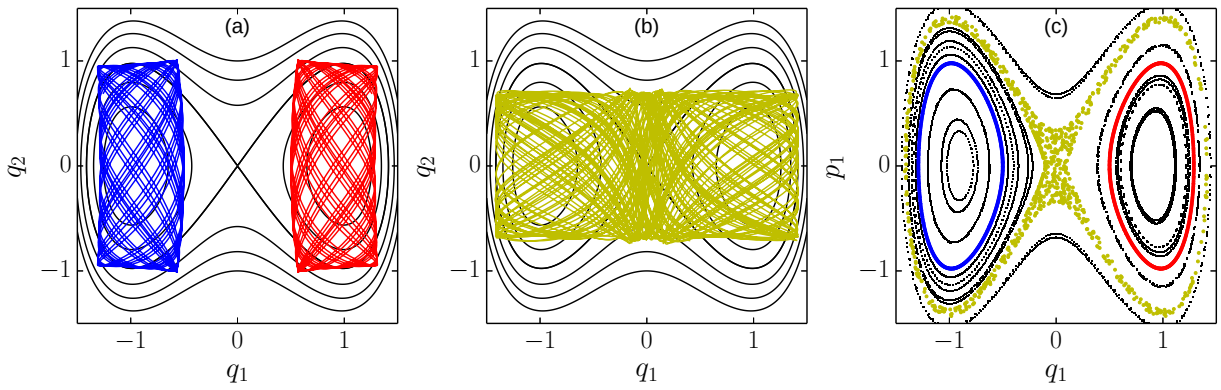

Figure 2.1: Typical trajectories of (a) the regular and (b) chaotic motion with energy $E = 3/2$ in configuration space are shown with the contour curves of the potential function (2.7). In (c) the Poincaré surface of section at the same energy is shown. The red, blue and yellow dots denote sequences of intersection points with the Poincaré surface of section for the associated trajectories shown in (a) and (b).

Such behaviors could be more clearly understood by introducing the Poincaré surface of section Σ [Arnold, Lichtenberg and Lieberman, Reichl, Tabor, Onuki and Yoshida]. As discussed above, the trajectories are confirmed on a 3-dimensional subspace in the four-dimensional phase space due to the total energy conservation. Especially in the Hamiltonian (2.6) case, the variable p_2, for example, is expressed as

$$p_2 = p_2(q_1, q_2, p_1; E) = \pm\sqrt{2\left(E - \frac{1}{2}p_1^2 - V(q_1, q_2)\right)}. \tag{2.10}$$

In the three-dimensional subspace (q_1, q_2, p_1), we introduce a surface section $\Sigma = (q_1, p_1)$ at $q_2 = 0$, for example. If the classical motion is bounded, the trajectories may repeatedly pass through the surface of section Σ.

Figure 2.1(c) demonstrates successive intersections of trajectories with the surface of section Σ with positive momenta $p_2 > 0$. The trajectories illustrated in Fig. 2.1(a) are restricted on a tours in phase space, and the sequence of intersection points lie on some smooth invariant curve (see blue and red curves in Fig. 2.1(c)). According to Kolmogorov-Arnold-Moser (KAM) theory, there exist invariant tori, if the frequency for the associated tours is sufficiently far from the resonance, *i.e.*, they satisfy the so-called Diophantine condition $|\boldsymbol{m}\cdot\boldsymbol{\Omega}| > C/|\boldsymbol{m}|^{\alpha}$, for all integer vectors $\boldsymbol{m}$, where C and $\alpha > N$ are positive constants [Arnold, Lichtenberg and Lieberman, Reichl]. If KAM tori survive, the successive intersections with the surface of section lie on a closed invariant curve. Since such an invariant curve dynamically prevents the

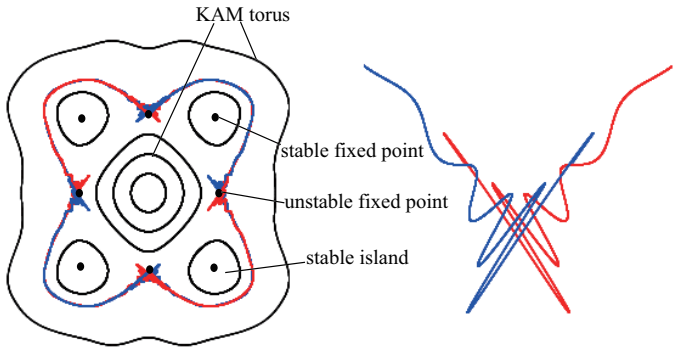

Figure 2.2: Left panel shows typical phase space structure on the surface of section around a stable/unstable periodic (fixed) point with associated homoclinic tangles of stable and unstable manifolds. Right panel shows the homoclinic tangle around an unstable fixed point.

passage between the left and the right well, it is often referred to as *dynamical barrier*.

On the other hand, the sequence of intersection points of trajectories shown in Fig. 2.1(b) seem to be random (see yellow dots in Fig. 2.1(c)). This is because the trajectories are not restricted on tori. The surface of section enables one to distinguish between the regular orbits, which lie on smooth curves on the surface of section, and the irregular or chaotic ones, which give rise to the random-looking patterns.

In general, the tours satisfying the resonant condition is broken by slight perturbation. After breaking up, the resonant torus is bifurcated into pair of stable and unstable periodic orbits. They appear as stable and unstable periodic (or fixed) points on the corresponding surface of section. The trajectories around stable fixed points are quasi-periodic, so there appear the invariant curves centered at the stable fixed point, which are referred to as *stable island chains* or *classical resonances*. On the other hand, the successive intersections of trajectories close to the unstable fixed points typically form a tangle of intersections between stable and unstable manifolds, which are called homoclinic/heteroclinic intersections. The homoclinic/heteroclinic structure is a manifestations of chaos in general. The schematic figure of the dynamics on the surface of section around the classical resonance is depicted in Fig. 2.2.

2.2 Classical dynamics of kicked Hamiltonian

As discussed the previous section 2.1, the classical dynamics with more than one degree of freedom exhibits regular and chaotic motions. The dynamics on the surface of the section allows us to introduce the *mapping* of the motion from the surface of section to itself, *i.e.*, let $f : \Sigma \to \Sigma$ be the map that gives the point in the surface of section

$$f : (q_n, p_n) \mapsto (q_{n+1}, p_{n+1}), \tag{2.11}$$

where (q_n, p_n) denotes the n-th intersection points on the surface of section hereafter.

Although the Poincaré surface of section displays generic features of the non-integrable in two-dimensional Hamiltonian systems, it is not an easy task to construct the associated mapping f explicitly. Therefore, instead of considering the Poincaré map induced from the continuous Hamiltonian flow, we introduce a one-dimensional kicked Hamiltonian

$$H(q, p, t) = T(p) + V(q) \sum_{n \in \mathbb{Z}} \tau \delta(t - \tau n), \tag{2.12}$$

as an alternative model for the mapping on the Poincaré surface of section. Here $T(p)$ and $V(q)$ are kinetic and potential functions, respectively. For the kicked Hamiltonian, the Hamilton's equations can explicitly be integrated from n-th kick to $n + 1$-th kick over period τ and the map f is then expressed as

$$p_{n+1} = p_n - \tau \frac{dV(q_n)}{dq}, \qquad q_{n+1} = q_n + \tau \frac{dT(p_{n+1})}{dp}. \tag{2.13}$$

This is nothing but the mapping on the Poincaré surface of section for the kicked Hamiltonian (2.12).

As an example, let us consider the case where $T(p) = p^2/2$ and $V(q) = k \cos q$. Here k denotes the strength of the kick. The classical map is expressed as

$$p_{n+1} = p_n + \tau k \sin q_n, \qquad q_{n+1} = q_n + \tau p_{n+1}. \tag{2.14}$$

Applying a scale transformation $P = p\tau, Q = q$, the map (2.14) is rewritten as

$$P_{n+1} = P_n + \varepsilon \sin Q_n, \qquad Q_{n+1} = Q_n + P_{n+1}, \tag{2.15}$$

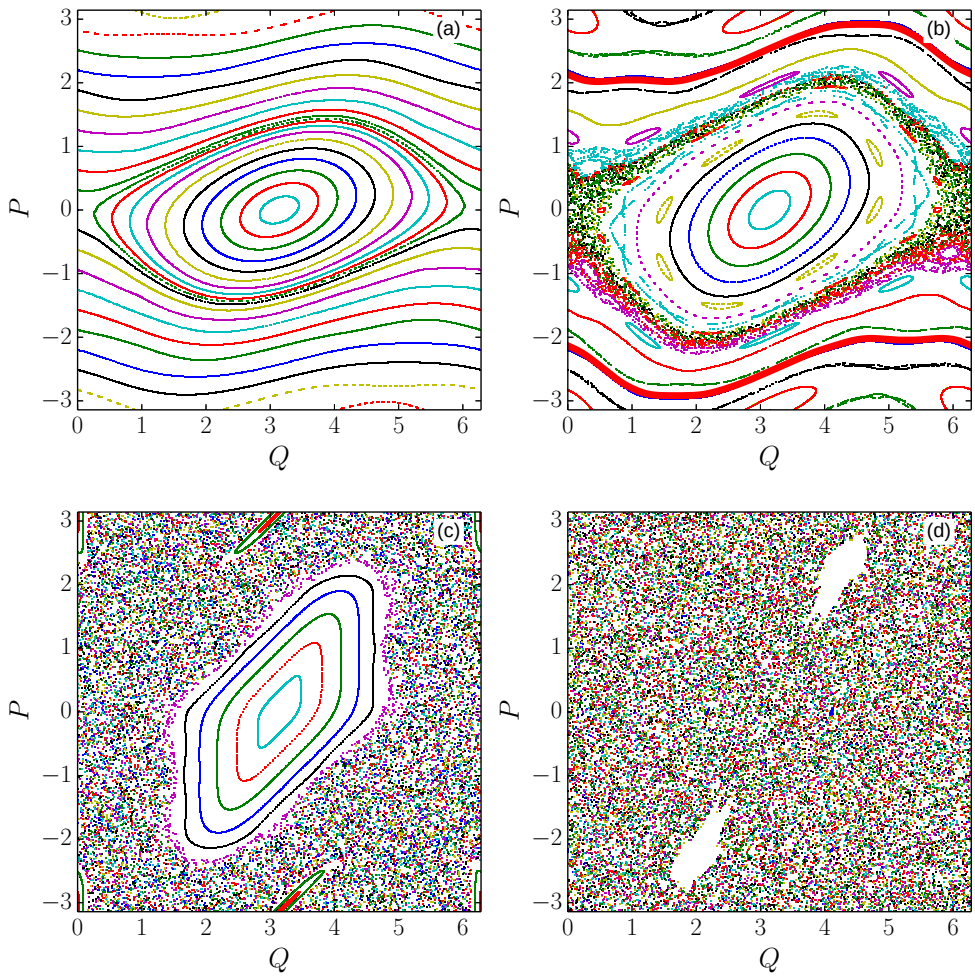

Figure 2.3: Classical phase space for the standard map (2.15) with (a) $\varepsilon = 0.5$, (b) $\varepsilon = 0.9$, (c) $\varepsilon = 2$ and (d) $\varepsilon = 5$.

where we take the perturbation strength as $\varepsilon = k\tau^2$. This map (2.15) is known as the *standard map* [Chirikov 1969; 1979], which is regarded as a generic model to exhibit all typical features of Hamiltonian systems.

Figure 2.3 shows the phase space portrait for the standard map. For a weak perturbation regime ($\varepsilon = 0.5$), most of trajectories follow the regular motions and the phase space is filled with the KAM curves (see Fig. 2.3(a)). On the other hand, chaotic regions gradually grows with increase in the perturbation strength ε, and for some intermediate value, say $\varepsilon = 0.9$, the phase space shows very complicated structures with regular and chaotic orbits (see Fig. 2.3(b)). As discussed in the previous section 2.1, the phase space of generic Hamiltonian systems typically forms a mixture of regular and chaotic orbits. Such phase space is

called as mixed-type phase space. For a more large ε regime, chaotic regions gradually dominates the phase space, and finally regular regions disappear (see Fig. 2.3(c) and (d)).

For KAM curves in a weak perturbation regime ε, it is possible to introduce a conjugating function which transforms the original dynamics into a constant rotation with rotation numbers $\nu = \Omega/2\pi$, where Ω is the frequency of the classical motion on KAM curves. The conjugating function can be expanded into the Fourier series of the angle variable

$$q = q(\theta) = \sum_k Q_k e^{ik\theta}, \qquad p = p(\theta) = \sum_k P_k e^{ik\theta}, \tag{2.16}$$

which is absolutely convergent for $\theta \in \mathbb{R}$, according to the KAM theorem. Since a single forward time evolution on the KAM curve leads to a constant shift $\theta \to \theta + 2\pi\nu$, the mapping relation (2.13) requires the following functional equations to hold:

$$p(\theta + 2\pi\nu) - p(\theta) = -\tau \frac{d}{dq} V(q(\theta)), \qquad q(\theta + 2\pi\nu) - q(\theta) = \tau \frac{d}{dp} T(p(\theta + 2\pi\nu)), \tag{2.17}$$

which can be solved by transforming them into a set of simultaneous algebraic equations for the Fourier coefficients in some cases [Shiromoto et al.]. Especially in the standard map, these coefficients of the Fourier series Q_k and P_k are expressed using by the double recurrence relation [Greene and Percival 1981]. The solid red curves in Fig. 2.3(b) depict the KAM curve with the golden mean rotation number $\nu = (\sqrt{5}-1)/2$, for which the convergence in terms of the continued fractional expansion is the slowest. The KAM tours with the golden mean frequency is believed to be most robust against perturbation and it is known that it breaks at the critical $\varepsilon = 0.971635\cdots$ [Greene 1979, Greene and Percival 1981, MacKay 1983]. Invariant tori are break up into so-call cantori [Aubry 1978, Mackay et al. 1984, Percival 1980].

2.3 Quantum dynamics of kicked Hamiltonian

In this section, we consider the quantum dynamics on the surface of section. As is the case in the previous section 2.2, we introduce the quantized kicked Hamiltonian [Casati et al. 1979]

$$\hat{H}(\hat{q}, \hat{p}, t) = \hat{T}(\hat{p}) + \hat{V}(\hat{q}) \sum_{n \in \mathbb{Z}} \tau \delta(t - n\tau), \tag{2.18}$$

where $\hat{q}$ and $\hat{p}$ are the position and the momentum operators, which satisfy the commutation relation $[\hat{q}, \hat{p}] = i\hbar$. For the kicked Hamiltonian, the time-dependent Schrödinger equation

$$i\hbar\frac{\partial}{\partial t}\psi(t) = \hat{H}|\psi(t)\rangle, \tag{2.19}$$

can be integrated from n-th kick to $n+1$-th kick over period τ, and the time evolution of wave function $|\psi_n\rangle$ is expressed using the evolution operator $\hat{U}$ as

$$|\psi_{n+1}\rangle = \hat{U}|\psi_n\rangle, \qquad \hat{U} = \exp\left(-\frac{i}{\hbar}\tau\hat{T}(\hat{p})\right)\exp\left(-\frac{i}{\hbar}\tau\hat{V}(\hat{q})\right). \tag{2.20}$$

Since the time evolution (2.20) is also expressed as $\hat{U} : |\psi_n\rangle \mapsto |\psi_{n+1}\rangle$, it is often referred to as the *quantum maps* [Berry et al. 1979, Tabor].

The τ time step evolution starting from an initial condition $\langle q_0|\psi_0\rangle$ is given by

$$\langle q_1|\psi_1\rangle = \int dq_0\; K(q_1, q_0; \tau)\langle q_0|\psi_0\rangle, \tag{2.21}$$

where

$$K(q_1, q_0; \tau) \equiv \langle q_1|\hat{U}|q_0\rangle. \tag{2.22}$$

is the so-called Feynman kernel. By inserting the completeness conditions

$$\int dq\; |q\rangle\langle q| = \mathbb{1}, \quad \text{or} \quad \sum_q |q\rangle\langle q| = \mathbb{1}, \tag{2.23}$$

into the Eq. (2.22), the 1 step Feynman kernel can be expressed as

$$\begin{aligned}
\langle q_1|\hat{U}|q_0\rangle &= \int dp_1 \langle q_1|e^{-\frac{i}{\hbar}T(\hat{p})\tau}|p_1\rangle\langle p_1|e^{-\frac{i}{\hbar}V(\hat{q})}|q_0\rangle \\
&= \frac{1}{2\pi\hbar}\int dp_1 \exp\left[\frac{i\tau}{\hbar}\left\{\frac{q_1 - q_0}{\tau}p_1 - T(p_1) - V(q_0)\right\}\right] \\
&= \frac{1}{2\pi\hbar}\int dp_1 \exp\left[\frac{i}{\hbar}S_1(p_1, q_1; q_0)\right],
\end{aligned} \tag{2.24}$$

where S_1 stands for the discrete action. The discrete action is expressed as $S_1 = \mathcal{L}\tau$ using a discrete

Lagrangian [Haake, Reichl, Tabor]

$$\mathcal{L}(p_1, q_1; q_0) = \frac{q_1 - q_0}{\tau} p_1 - T(p_1) - V(q_0). \tag{2.25}$$

We notice that in the continuous time limit $\tau \to 0$, the discrete Lagrangian $\mathcal{L}$ takes a typical form as

$$\mathcal{L} = p\dot{q} - H, \tag{2.26}$$

via Legendre transformation of the Hamiltonian.

For the multiple time evolution, the Feynman kernel $K_n(q_n, q_0)$ is expressed as

$$\begin{aligned}
K_n(q_n, q_0) &\equiv \langle q_n | \hat{U}^n | q_0 \rangle \\
&= \langle q_n | \prod_{j=0}^{n-1} \left[e^{-\frac{i}{\hbar} T(\hat{p_j})} e^{-\frac{i}{\hbar} V(\hat{q_j})} \right] | q_0 \rangle \\
&= \int dq_1 \cdots dq_{n-1} \int dp_1 \cdots p_{n-1} \prod_{j=0}^{n-1} \langle q_{j+1} | e^{-\frac{i}{\hbar} T(p_{j+1})} | p_{j+1} \rangle \langle p_{j+1} | e^{-\frac{i}{\hbar} V(q_j)} | q_j \rangle \\
&= \left(\frac{1}{2\pi\hbar} \right)^n \int \prod_{j=0}^{n-1} dq_j \int \prod_{j=0}^{n-1} dp_j \exp \left[\frac{i\tau}{\hbar} \sum_{j=0}^{n-1} \left\{ \frac{q_{j+1} - q_j}{\tau} p_{j+1} - T(p_{j+1}) - V(q_j) \right\} \right] \\
&= \left(\frac{1}{2\pi\hbar} \right)^n \int \prod_{j=0}^{n-1} dq_j \int \prod_{j=0}^{n-1} dp_j \exp \left[\frac{i}{\hbar} S_n(\{q_j\}, \{p_j\}) \right]
\end{aligned} \tag{2.27}$$

where $\{q_j\}, \{p_j\}$ denotes the set of the variable $\{q_0, q_1 \cdots\}$ and $\{p_0, q_1 \cdots\}$, respectively. Equation (2.27) is nothing less than the Path integral formulation [Feynman and Hibbs, Schulman] for the mapping systems.

Since the dynamics of the quantum map is described as the sequence of the periodic time evolution, the Floquet theorem [Reichl, Saito] allows us to introduce the stationary state under the operator $\hat{U}$, *i.e.*, the eigenvalue u_m and eigenstate $|\Psi_m\rangle$ are given as

$$\hat{U} |\Psi_m\rangle = u_\ell |\Psi_m\rangle, \tag{2.28}$$

where the eigenvalue is expressed as $u_m = e^{iE_m \tau/\hbar}$ and E_m is called the quasi-energy. Knowing the

eigenvalues and eigenstates, the Feynman kernel takes another form as

$$K_n(q_n, q_0; \tau) = \sum_m e^{-\frac{i}{\hbar} n\tau E_m} \langle q_n|\Psi_m\rangle\langle\Psi_m|q_0\rangle. \tag{2.29}$$

Here we use the completeness condition for the eigenstate $\sum_m |\Psi_m\rangle\langle\Psi_m| = \mathbb{1}$.

As a concrete example, let us consider the eigenvalue problem for the quantized standard map $\hat{U}$, which is given by function $\hat{T}(\hat{p}) = \hat{p}^2/2$ and $\hat{V}(\hat{q}) = k\cos\hat{q}$. Here we impose a periodic boundary condition on the region $(q, p) \in (0, 2\pi] \times (-\pi, \pi]$. As a result, the area of the phase space $W = 4\pi^2$ is quantized in units of the effective Planck's constant

$$h = W/N, \tag{2.30}$$

where N is the dimension of the Hilbert space of the system.

In order to visualize wave function in the phase space, we introduce the Husimi-representation which is given by the projection of the wave function onto the coherent state

$$\langle q|\alpha(q_c, p_c)\rangle = \left(\frac{1}{\pi\hbar^2}\right)^{1/4} e^{-(q-q_c)^2/2\hbar + ip_c(q-q_c)/\hbar}, \tag{2.31}$$

whose center is (q_c, p_c). The Husimi-representation is given by

$$\rho_H(q, p) = |\langle\alpha(q, p)|\Psi\rangle|^2, \tag{2.32}$$

and it represents a quasi-probability density in the phase space.

Figure 2.4 shows the eigenstate $|\Psi_m\rangle$ in the Husimi-representation. As shown in Figs. 2.4(a) and (b), some eigenstates have their supports on the corresponding elliptic invariant curves. As can be seen in Fig. 2.4(c) and (d), on the other hand, the support of some other eigenstates $|\Psi_m\rangle$ are not invariant curves but classical resonances, specified such as $1:8$, in case (c), and the chaotic region in case (d).

For the systems with mixed phase space, the semiclassical eigenfunction hypothesis [Berry 1977, Percival 1973] implies that each eigenstate $|\Psi_m\rangle$ has a support either on a regular or on a chaotic region in the semiclassical limit $\hbar \to 0$. For the finite $\hbar$ regime, on the other hand, the wave function spreads over the classical invariant curves and so the transition between regular and chaotic regions is not forbidden.

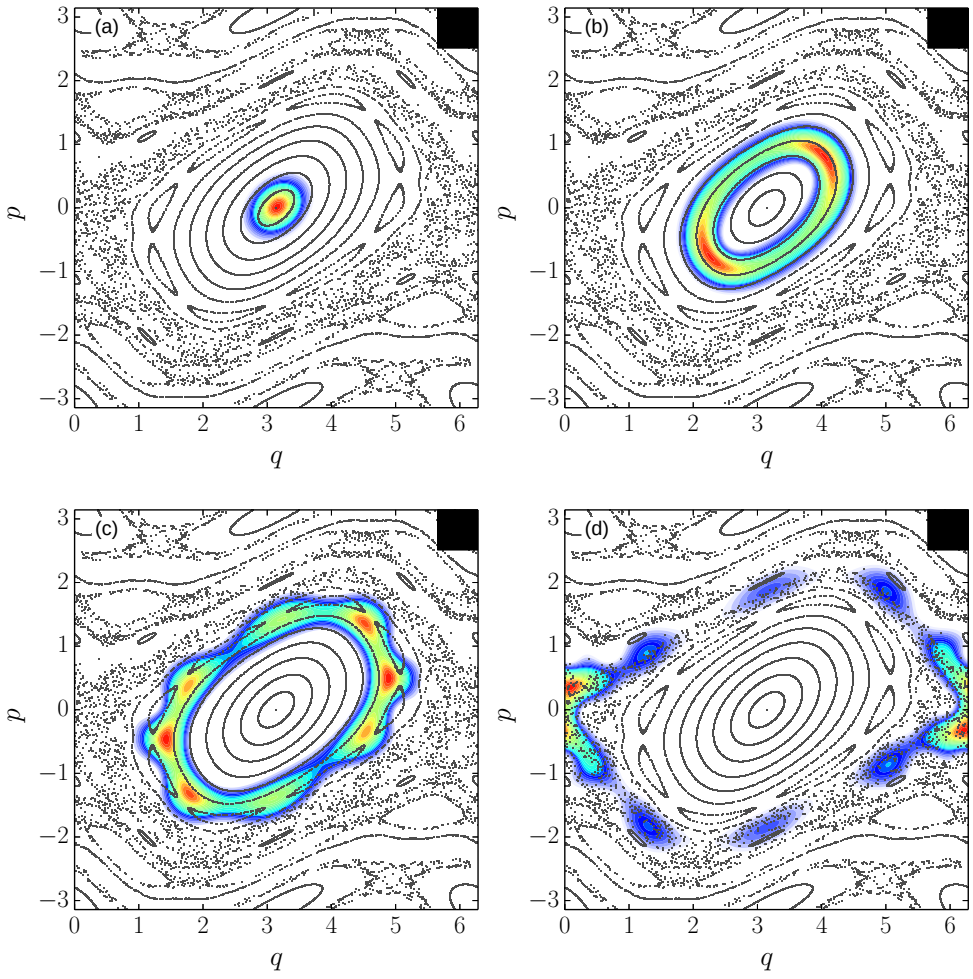

Figure 2.4: Some eigenstates in the Husimi-representation for quantized standard map with $k = 1$. Upper right box represents the size of effective Planck's cell h.

Such a process is *dynamical tunneling* [Davis and Heller 1981, Keshavamurthy and Schlagheck 2011] as a generalization of the potential barrier tunneling.

Chapter 3

Theory of tunneling splitting

The tunneling effect is peculiar to quantum mechanics and no counterparts exist in classical mechanics. The most important qualitative difference between one-and multi-dimensional systems would be that classical particles are confined not only by the energy barrier, but also by the dynamical barrier as discussed in the previous chapter 2. What is more crucial is the fact that generic multi-dimensional systems are no more completely integrable and chaos appears in the underlying classical dynamics, so one must take into account new aspects of quantum tunneling absent in completely integrable systems [Creagh 1998, Keshavamurthy and Schlagheck 2011].

In this chapter, we will consider the tunneling effect of the eigenstates. Before consideration is given to non-integrable systems, we will explain the tunneling splitting in section 3.1, which will be use to measure quantum tunneling quantitatively. In section 3.2, we will briefly review the theory *resonance-assisted tunneling* [Brodier et al. 2002, Schlagheck et al. 2011], which especially attracts a great deal of attention since it explains various important features of tunneling in non-integrable systems. In section 3.3, we outline the semiclassical description for resonance-assisted tunneling in integrable system [Le Deunff et al. 2013]. Then we will discuss the validity of applying resonance-assisted tunneling scenario to non-integrable systems.

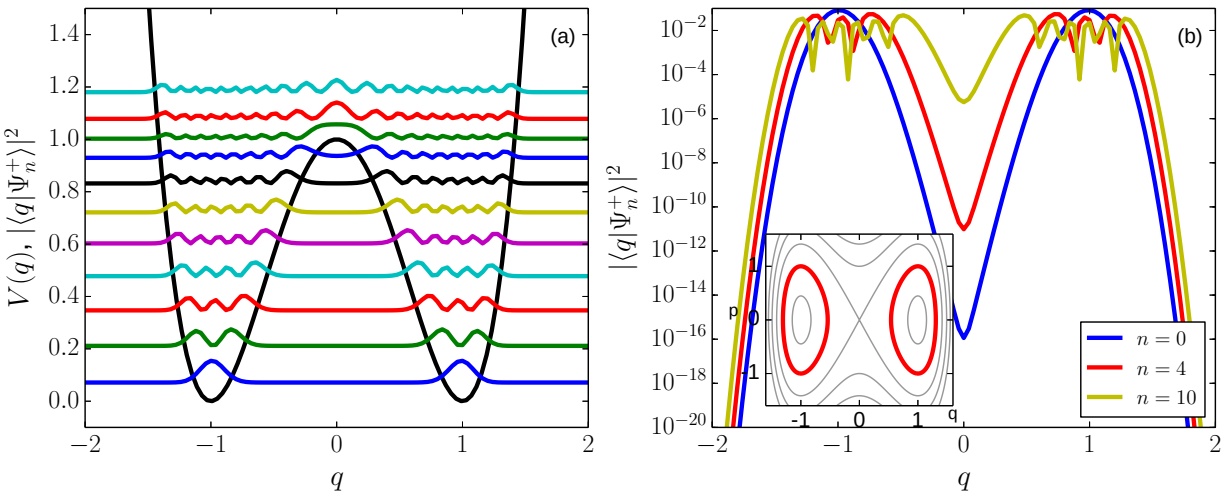

Figure 3.1: The eigenstate $|\Psi_n^+\rangle$ in the q-representation for the double well potential with $a = 1$ in (a) normal scale and (b) semi-log scale. The inset of (b) shows the classical phase space and the red curve draws energy contour with $E = 1/2$.

3.1 Tunneling splitting in the double well system

In this section, we will consider quantum tunneling observed in the eigenstates. For tunneling in eigenstates, the energy splitting associated with the symmetry of the potential function is often discussed. We explain some basic aspects of the tunneling splitting using a one-dimensional double well system, for which Hamiltonian is expressed as

$$H(q,p) = \frac{p^2}{2} + V(q), \tag{3.1}$$

with the potential function

$$V(q) = (q^2 - a)^2. \tag{3.2}$$

When the energy is less than the local maximum $E < a^2$, classical trajectories in phase space form an elliptic curves which means that the (real) classical dynamics cannot go over the potential barrier (see the red curve in the inset of Fig. 3.1(b)). On the other hand, the wave packet can penetrate the potential barrier, and such a purely quantum effect is usually referred to as *tunneling*.

We consider the tunneling problem for eigenstates in the double well system. We denote the eigenvalue equation by

$$\hat{H}|\Psi_n^\pm\rangle = E_n^\pm|\Psi_n^\pm\rangle. \tag{3.3}$$

The potential function (3.2) is symmetric with respect to the q-axis, so the eigenstate is also symmetric with respect to the q-axis, that $\Psi_n^{\pm}(q) = \pm\Psi_n^{\pm}(-q)$ is satisfied. Figure 3.1 demonstrates the eigenstates $|\Psi_n^{+}\rangle$ which have numerically been obtained. In the following discussion we consider the approximate construction of the eigenstate $|\Psi^{\pm}\rangle$[1] based on WKB theory, whose procedure follows a standard textbook such as [Landau and Lifshits].

We assume that $\Psi_{\rm loc}(q)$ is a local WKB solution only in the right-hand side $q \geq 0$ with energy $E_{\rm loc}$[2]. Here the local solution is normalized in the right-hand side as $\int_0^\infty |\Psi_{\rm loc}(q)|^2 = 1$. The eigenstates $\Psi^{\pm}(q)$ of the system are given as a linear combination of the local WKB solution

$$\Psi^{+}(q) \simeq \frac{1}{\sqrt{2}} \left(\Psi_{\rm loc}(q) + \Psi_{\rm loc}(-q)\right), \tag{3.4}$$

$$\Psi^{-}(q) \simeq \frac{1}{\sqrt{2}} \left(\Psi_{\rm loc}(q) - \Psi_{\rm loc}(-q)\right). \tag{3.5}$$

These relations lead that at $q = 0$

$$\Psi^{+}(0) = \sqrt{2}\Psi_{\rm loc}(0), \qquad \Psi^{-}(0) = 0, \tag{3.6a}$$

$$\Psi'^{+}(0) = 0, \qquad \Psi'^{-}(0) = \sqrt{2}\Psi'_{\rm loc}(0), \tag{3.6b}$$

and

$$\int_0^\infty \Psi_{\rm loc}(x)\Psi^{\pm} dq \approx \int_0^\infty |\Psi_{\rm loc}(q)|^2 dq = 1/\sqrt{2}. \tag{3.6c}$$

Here the prime stands for the derivative with respect to q. The Schrödinger equation for the eigenstates $\Psi^{\pm}(q)$ and $\Psi_{\rm loc}(q)$ is given as

$$\Psi''^{\pm}(q) + \frac{2}{\hbar^2}(E^{\pm} - V(q))\Psi^{\pm}(q) = 0, \tag{3.7a}$$

$$\Psi''_{\rm loc}(q) + \frac{2}{\hbar^2}(E_{\rm loc} - V(q))\Psi_{\rm loc}(q) = 0. \tag{3.7b}$$

By multiplying (3.7a) by $\Psi_{\rm loc}$ and (3.7b) by $\Psi^{\pm}$ and subtracting from each other, we find

$$\frac{2}{\hbar^2}(E^{\pm} - E_{\rm loc})\Psi_{\rm loc}(q)\Psi^{\pm}(q) = \Psi_{\rm loc}(q)\Psi''^{\pm}(q) - \Psi^{\pm}(q)\Psi''_{\rm loc}(q). \tag{3.8}$$

[1] In the following discussion, we drop the quantum number n.

[2] $\Psi_{\rm loc}(q)$ is also a local solution in the left-hand side ($q \leq 0$) with energy $E_{\rm loc}$ due to the symmetry.

Integrating the both side of Eq. (3.8) from 0 to ∞, we find

$$\begin{aligned}\frac{\sqrt{2}}{\hbar^2}(E^{\pm} - E_{\rm loc}) &= \int_0^{\infty} \Psi_{\rm loc}(q)\Psi''^{\pm}(q) - \Psi^{\pm}(q)\Psi''_{\rm loc}(q)\, dq \\ &= [\Psi_{\rm loc}\Psi'^{\pm} - \Psi^{\pm}\Psi'_{\rm loc}]_0^{\infty} - \int_0^{\infty} \Psi'_{\rm loc}(q)\Psi'^{\pm}(q) - \Psi'^{\pm}(q)\Psi'_{\rm loc}(q)\, dq, \end{aligned} \tag{3.9}$$

and

$$E^+ - E_{\rm loc} = -\hbar^2\Psi_{\rm loc}(0)\Psi'_{\rm loc}(0), \tag{3.10a}$$

$$E^- - E_{\rm loc} = \hbar^2\Psi'_{\rm loc}(0)\Psi_{\rm loc}(0). \tag{3.10b}$$

Therefore the energy of the symmetric and antisymmetric state $|\Psi^{\pm}\rangle$ slightly shifts from $E_{\rm loc}$ and the amount of the energy shift is given by

$$\Delta E := E^- - E^+ \simeq 2\hbar^2\Psi'_{\rm loc}(0)\Psi_{\rm loc}(0), \tag{3.11}$$

where ΔE is referred to as *tunneling splitting*, which is regarded as representing tunneling probability for the wave packet to penetrate the potential barrier.

The splitting formula (3.11) can also be interpreted via WKB (semiclassical) wave function. The eigenfunction and its derivative in the classical forbidden region is expressed semiclassically as

$$\Psi_{\rm loc}(q) = \sqrt{\frac{\Omega}{2\pi p(q)}} \exp\left(-\frac{1}{\hbar}\int_0^{t_p} |p(q')|\, dq'\right), \quad \Psi'_{\rm loc}(q) = \frac{p(q)}{\hbar}\Psi_{\rm loc}(q), \tag{3.12}$$

where $p(q) = \pm\sqrt{2(E - V(q))}$ and t_p is a turning point [Landau and Lifshits]. Here Ω is the frequency for the oscillation of the particle. Note that the $p(q)$ takes a pure imaginary value between $-t_p < q < t_p$. Using Eq. (3.12), the tunneling splitting is semiclassically expressed as

$$\Delta E \sim Ae^{-S/\hbar}, \tag{3.13}$$

where the amplitude factor A and the classical action S are respectively given as

$$A = \frac{\Omega\hbar}{\pi}, \qquad S = \int_{-t_p}^{t_p} |p(q')|\, dq'. \tag{3.14}$$

Here the classical action S is referred to as the instanton action [Coleman 1988]. This formula tells us that the tunneling splitting ΔE decays exponentially as a function of $1/\hbar$. This is a reasonable result because the tunneling effect is supposed to be exponentially small and vanish in the semiclassical limit $\hbar \to 0$. We also notice that using the Eq. (3.12) the tunneling splitting could be written as

$$\Delta E \sim 2\hbar p(0)\Psi^2_{\rm loc}(0) = \hbar p(0)\Psi^{+2}(0), \tag{3.15}$$

where we have used the relation (3.6) at $q = 0$. Therefore, the splitting ΔE correlates with the amplitude of the symmetric eigenstate $\Psi^+(q)$ at $q = 0$. The splitting formula in multidimensional (quasi-)integrable systems without classical resonances, has been derived in [Wilkinson 1986] as

$$\Delta E \sim Ae^{-S/\hbar}, \tag{3.16}$$

where the amplitude factor A is in proportion to $\hbar^{3/2}$ and S denotes the instanton action in multi-dimensional space.

Figure 3.2 shows the analytic continuation of the curve

$$p(q) = \pm\sqrt{2(E - V(q))}, \qquad V(q) = (q^2 - 1)^2, \tag{3.17}$$

into the imaginary energy. In Eq. (3.17), the integration between turning points $-t_p < q < t_p$ is evaluated along the red curve whose imaginary energy is zero. The so-call instanton path is a complex orbit connecting the symmetrically situated two wells.

So far, we have derived the tunneling splitting based on the eigenstate in the q-representation. For the convenience of the formulation, we here provide another derivation for the tunneling splitting. We assume a one dimensional time-independent Hamiltonian H that exhibits two main symmetric regions in phase space, in analogy with the double well system. Suppose the local WKB solution of the left $|L\rangle$ and right $|R\rangle$ wells

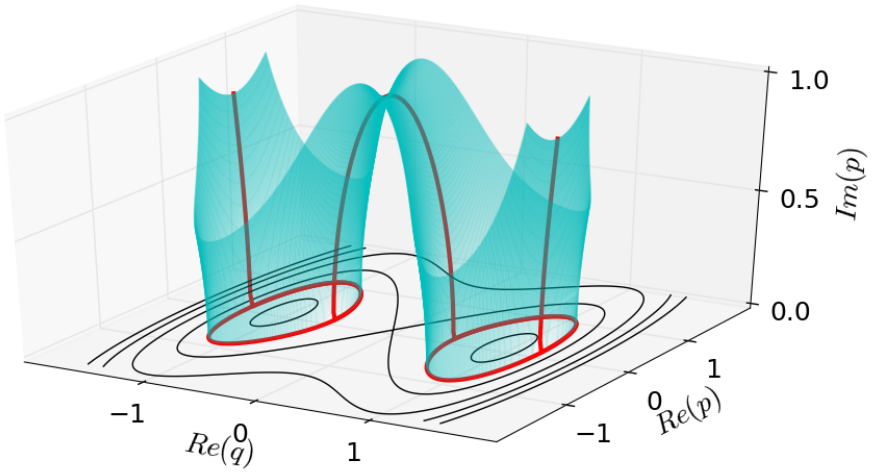

Figure 3.2: The analytic continuation of the curve (3.17) for the real energy $E = 1/2$. The cyan surface has an imaginary energy and the red curves represent the manifolds with a real energy.

with degenerate energy E_0. The eigenstates $|\Psi^{\pm}\rangle$ of the Hamiltonian H are given as a linear combination

$$|\Psi^{\pm}\rangle \simeq \frac{1}{\sqrt{2}}(|L\rangle \pm |R\rangle). \tag{3.18}$$

This suggests that the Hamiltonian $\hat{H}$ is simply expressed by the two-dimensional matrix in which $|L\rangle$ and $|R\rangle$ are taken as the basis functions has. The corresponding energies $E^{\pm}$ are given as

$$\langle\Psi^{\pm}|\hat{H}|\Psi^{\pm}\rangle = E^{\pm}. \tag{3.19}$$

Substituting $|\Psi^{\pm}\rangle$ given in (3.18) into Eq. (3.19),

$$\begin{aligned} E^{\pm} &\simeq \frac{1}{2}\langle L \pm R|\hat{H}|L \pm R\rangle \\ &= \frac{1}{2}\Big(\langle L|\hat{H}|L\rangle + \langle R|\hat{H}|R\rangle \pm \langle L|\hat{H}|R\rangle \pm \langle R|\hat{H}|L\rangle\Big) \\ &= \frac{1}{2}\Big(2E_0 + \langle L|\hat{H} - \hat{H}_0|L\rangle + \langle R|\hat{H} - \hat{H}_0|R\rangle \pm 2\langle L|\hat{H}|R\rangle.\Big) \end{aligned} \tag{3.20}$$

Subtracting from each other, the energy splitting

$$\Delta E = E^+ - E^- \simeq 2\langle L|\hat{H}|R\rangle, \tag{3.21}$$

is evaluated as the off-diagonal term. The diagonal matrix elements are given as

$$\begin{aligned}\langle L|\hat{H}|L\rangle &\simeq \frac{1}{2}\langle \Psi^+ + \Psi^-|\hat{H}|\Psi^+ + \Psi^-\rangle \\ &= \frac{1}{2}\left(\langle\Psi^+|\hat{H}|\Psi^+\rangle + \langle\Psi^-|\hat{H}|\Psi^-\rangle + 2\langle\Psi^+|\hat{H}|\Psi^-\rangle\right) \\ &= \frac{1}{2}\left(E^+ + E^-\right) = E_0 \simeq \langle R|\hat{H}|R\rangle. \end{aligned} \tag{3.22}$$

Therefore the Hamiltonian matrix is represented by

$$\hat{H} = \begin{pmatrix} E_0 & \Delta E/2 \\ \Delta E/2 & E_0 \end{pmatrix}, \tag{3.23}$$

and the eigenvalues are expressed as $E_0 \pm \Delta E/2$ as expected.

Now we consider the dynamics of the state $|R\rangle$, which localizes in the right-hand side of the well. The time-evolution of $|R\rangle$ is expressed as

$$\begin{aligned}|\psi(t)\rangle = e^{-\frac{i}{\hbar}t\hat{H}}|R\rangle &= \frac{1}{\sqrt{2}}\left(e^{-\frac{i}{\hbar}(E_0-\frac{\Delta E}{2})t}|\Psi^+\rangle + e^{-\frac{i}{\hbar}(E_0+\frac{\Delta E}{2})}|\Psi^-\rangle\right) \\ &= \frac{1}{2}e^{-\frac{i}{\hbar}E_0 t}\left\{e^{\frac{i\Delta E}{2\hbar}t}(|R\rangle + |L\rangle) + e^{-\frac{i\Delta E}{2\hbar}t}(|R\rangle - |L\rangle)\right\} \\ &= e^{-\frac{i}{\hbar}E_0 t}\left\{\cos\left(\frac{\Delta E}{2\hbar}t\right)|R\rangle + i\sin\left(\frac{\Delta E}{2\hbar}t\right)|L\rangle\right\}. \end{aligned} \tag{3.24}$$

At $t = \pi\hbar/\Delta E$, the right state $|R\rangle$ moves to the left state $|L\rangle$. Therefore the state $|R\rangle$ periodically oscillates between the two wells with period of

$$T = \frac{h}{\Delta E}. \tag{3.25}$$

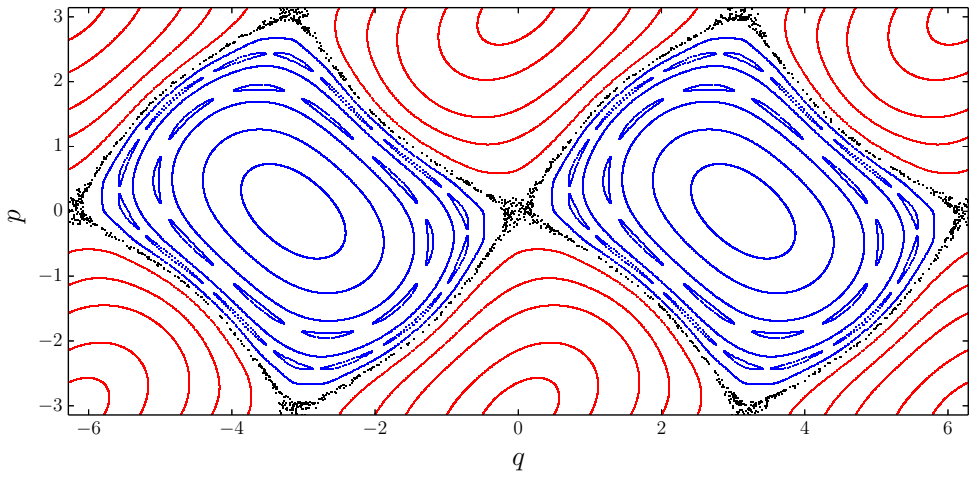

Figure 3.3: The classical phase space of the Harper map corresponding to Eq. (3.26)

3.2 Resonance-assisted tunneling

A two level approach in Eq. (3.23) breaks down, if the chaotic region appears in the phase space. The role of chaos in quantum tunneling has first been discussed in the observation of the wave packet dynamics [Lin and Ballentine 1990], and then is clearly recognized in the behavior of the tunneling splitting of eigenenergies [Bohigas et al. 1990; 1993a;b, Roncaglia et al. 1994, Tomsovic and Ullmo 1994]. In non-integrable systems, a doublet forming a tunneling splitting is not isolated in the whole energy space. It can happen that the states forming a doublet and a state supported by the chaotic region come close to each other and form avoided crossings. Within the interaction regime of energy resonance, the energy splitting between the doublet becomes large through the coupling with the chaotic state, meaning that the tunneling amplitude between one tours to the other is enhanced. *Chaos-assisted tunneling* (CAT) occurs in this way [Bohigas et al. 1993b, Tomsovic and Ullmo 1994]. The enhancement of the tunneling due to the energy level resonance is often called *resonant tunneling*, which is reduced to a one-dimensional triple-well potential [Le Deunff and Mouchet 2010, Schlagheck et al. 2011].

A more direct explanation for the tunneling in non-integrable systems was given based on the time-domain semiclassical analysis [Onishi et al. 2003, Shudo and Ikeda 1994; 1995; 1998, Shudo et al. 2009a;b]. In particular, the complex dynamical systems could explain the tunneling effect in non-integrable systems. This semiclassical analysis tells us that exponentially many complex orbits connecting the tours and chaotic

region give rise to the enhancement of the tunneling probability. This tunneling effect is called *chaotic tunneling*. Especially, chaos in complex domain, the so-called *Julia sets*, plays a fundamental role in the tunneling in non-integrable systems [Shudo et al. 2009a;b].

The enhancement of the tunneling probability has been reported not only in the strongly chaotic regime but also in the nearly-integrable regime. The phase space of the latter is almost filled with KAM tori like Fig. 3.3. Such enhancement of the tunneling splitting was first reported by [Roncaglia et al. 1994]. Then the authors of Ref. [Bonci et al. 1998] pointed out that the energy level resonances are induced by not only chaos but classical nonlinear resonances.

The authors of Ref. [Brodier et al. 2001; 2002] conjectured that the complexified KAM curve does not seem to provide an appropriate frame work for the semiclassical study of nearly-integrable regime, because the analytic continuations of the invariant KAM curve with each symmetric wells do not meet each other unlike the double well potential system (see Fig. 3.2). In general, KAM curves specified as Eq. (2.16) has the radius of convergence in complex angle variable at θ^* and singularities accumulate along θ^* [Berretti and Chierchia 1990, Berretti et al. 1992, Greene and Percival 1981]. Such a border of analyticity is conjectured to form the natural boundary. The instanton connection along the complexified KAM curve is interrupted by the natural boundary of the KAM curve. (This topic revisits in section 4.1)

Instead of overcoming issues arising from the existence of the natural boundary, the authors of Ref. [Brodier et al. 2002] investigated the coupling mechanism between low lying and excited states, which is referred to as *resonance-assisted tunneling* (RAT). RAT has been shown to successfully reproduce the splitting curve not only in the nearly-integrable regime but also in the strongly chaotic regime [Eltschka and Schlagheck 2005, Keshavamurthy 2005, Löck et al. 2010, Mouchet et al. 2006, Schlagheck et al. 2011, Sheinman et al. 2006]. We should note that the study of tunneling in the system with nonlinear resonances was first made in the work of [Ozorio de Almeida 1984]. So far, it has been believed that the origin of the enhancement of the splitting could be explained in the framework of RAT.

Before we explain theory of RAT more precisely, we actually demonstrate how the enhancement of tunneling splitting is observed in non-integrable systems. Let us consider the quantized Harper map

$$\hat{U} = \exp\left(\frac{i}{\hbar}\cos\hat{p}\right)\exp\left(\frac{i}{\hbar}\cos\hat{q}\right), \tag{3.26}$$

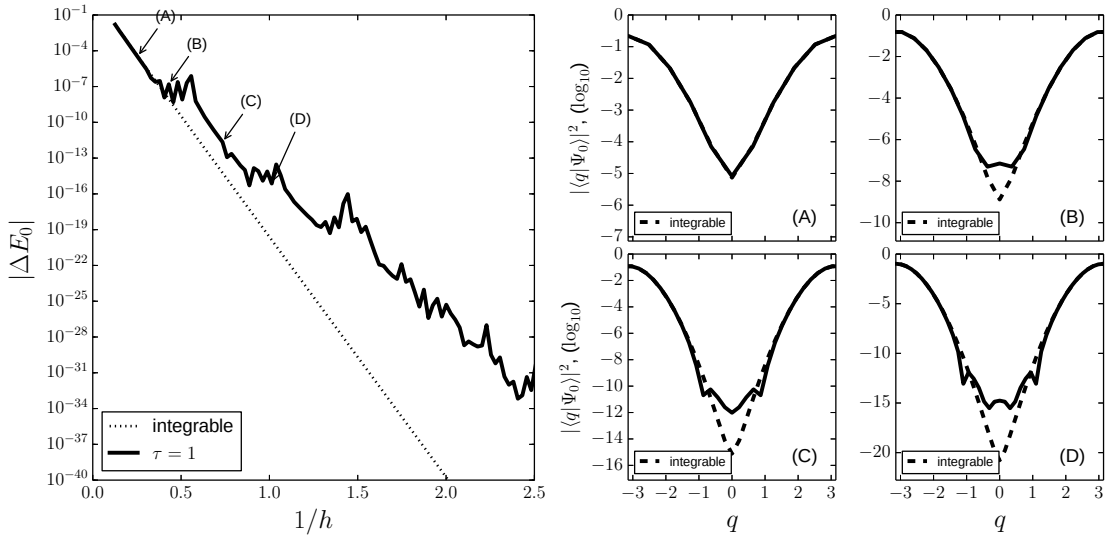

Figure 3.4: Left panel shows the tunneling splitting ΔE_0 as a function of the effective Planck's constant $1/h$ for the ground state and first excited of the quantized Harper map with $\tau = 1$. Dashed curve denotes the tunneling splitting for the associated integrable Hamiltonian $\hat{H}_{\rm eff}^{(M)}$ with $M = 5$. Right panels (A)-(D) show the eigenstate $|\Psi_0^+\rangle$ in q-representation with $1/h$, each of which is indicated in the Left panel.

for which the associated classical phase space is shown in Fig. 3.3. We then consider the tunnel splitting ΔE of bounded states localizing at $(q, p) = (\pm\pi, 0)$. Left panel in Fig. 3.4 shows the tunneling splitting as a function of the effective Planck's constant $1/h$. For reference, Fig. 3.4 shows the splitting of the corresponding integrable one, which is given by the effective integrable Hamiltonian $\hat{H}_{\rm eff}^{(M)}$ (see Appendix B). We notice that the tunneling splitting ΔE in a small $1/h$ regime for the quantized Harper map coincides with that of the integrable one. On the other hand, the splitting ΔE in the Harper map becomes larger than that in the corresponding integrable one by several orders of magnitude. The splitting curve typically forms *plateaus* accompanied by spikes due to the energy resonance and rapidly decaying region. We refer to the structure of plateau and rapidly decaying region as the *staircase structure*. It would be worth mentioning that the characteristic pattern of the eigenstate appears around $q = 0$: the eigenstate takes a convex structure in the plateau of the splitting curve (see Fig. 3.4(B) and (D))[3], and a concave structure in the rapidly decaying regime (see Fig. 3.4(A) and (C)).

In what follows, we review RAT theory developed in [Brodier et al. 2002, Schlagheck et al. 2011]. As

[3]In Fig. 3.4(A), the convex structure is difficult to see but it possible to decompose the component which makes a convex structure using contribution decomposition discussed in sections 4.2 and 5.3

shown in Fig. 3.3, classical phase space in non-integrable systems has classical resonance chains. Theory of RAT begins with performing integrable approximation around classical resonance chains. For this purpose, we formally introduce an integrable Hamiltonian $H_0(I)$ expressed by action variable I, and consider the time-dependent perturbed Hamiltonian

$$H(I, \theta, t) = H_0(I) + \varepsilon V(I, \theta, t), \tag{3.27}$$

where ε is the perturbation strength. We here assume the periodic time dependent perturbation $V(I, \theta, t) = V(I, \theta, t + \tau)$ with period of τ. Besudes, we assume that there exist two symmetric regular regions in phase space, each of them contains $r : s$ resonance island chains (like a situation in Fig. 3.3). First, we consider the classical motion around the resonant tours $I = I_{r:s}$, which satisfies the resonance condition between the external frequency $\omega = 2\pi/\tau$ and the intrinsic frequency of the Hamiltonian $H_0(I)$, that is,

$$r\Omega_{r:s} = s\omega, \tag{3.28}$$

where

$$\Omega_{r:s} := \left.\frac{dH_0}{dI}\right|_{I=I_{r:s}}. \tag{3.29}$$

This resonant condition means that the angle variable shifts as $\theta \to \theta + 2\pi s$ after the time evolution $t \to t + r\tau$ on the tours $I = I_{r:s}$. In other words, the angle variable rotates $\theta \to \theta + 2\pi s/r$ during $t : 0 \to \tau$. As discussed in section 2.1, such a resonant condition gives rise to breakdown of tori and form classical resonance islands.

To approximate of the classical motion around the classical resonance, we introduce co-rotating frame [Lichtenberg and Lieberman], which is performed by introducing a new angle variable

$$\vartheta = \theta - \Omega_{r:s} t. \tag{3.30}$$

After the corresponding transformation given as $H \mapsto \mathcal{H} = H - \Omega_{r:s} I$, we obtain the new Hamiltonian with action-angle variable (I, ϑ) as

$$\mathcal{H}_{r:s}(I, \vartheta, t) = \mathcal{H}_0(I) + \mathcal{V}(I, \vartheta, t), \tag{3.31}$$

where

$$\mathcal{H}_0(I) = H_0(I) - \Omega_{r:s} I, \qquad \mathcal{V}(I, \vartheta, t) = \epsilon V(I, \vartheta + \Omega_{r:s} t, t). \tag{3.32}$$

If the ϑ varies on a time scale that is rather large compared to the period $2\pi/\omega$ of the external driving, we can apply the time average over r periods

$$\bar{\mathcal{V}}(I, \vartheta) = \frac{1}{r\tau} \int_0^{r\tau} \mathcal{V}(I, \vartheta, t)\, dt, \tag{3.33}$$

according to the adiabatic perturbation theory [Lichtenberg and Lieberman], and expand the time-averaged perturbation term in a Fourier series,

$$\bar{\mathcal{V}}(I, \vartheta) = \sum_{\ell=1}^{\infty} 2V_\ell(I) \cos(j\ell\vartheta + \phi_\ell). \tag{3.34}$$

Next, we perform a Taylor expansion $\mathcal{H}_0$ around $I = I_{r:s}$ as,

$$\mathcal{H}_0(I) \simeq \mathcal{H}_0^{(0)} + \frac{(I - I_{r:s})^2}{2m_{r:s}} + O[(I - I_r : s)^3], \tag{3.35}$$

where $\mathcal{H}_0^{(0)} \equiv H_0(I_{r:s}) - \Omega_{r:s} I_{r:s}$ is a constant and the quadratic term is characterized by the effective "mass" parameter $1/m_{r:s} \equiv d^2 H_0/dI^2$ at $I = I_{r:s}$. Finally, the classical dynamics around classical resonance is approximately expressed by the generalized pendulum Hamiltonian

$$H_{\rm pen}(I, \vartheta) \equiv \frac{(I - I_{r:s})^2}{2m_{r:s}} + \sum_{\ell=1}^{\infty} 2V_\ell(I) \cos(\ell r\vartheta + \phi_\ell). \tag{3.36}$$

Here we absorb constant terms in the left-hand side. Note that the Hamiltonian (3.36) is integrable and theory of RAT is based on this integrable Hamiltonian (3.36).

Assuming the perturbation strength ε or the second term of (3.36) as being small, we next apply the quantum perturbation theory. The Hamiltonian (3.36) is quantized via canonical quantization with the commutation relation $[\hat{I}, \hat{\vartheta}] = i\hbar$, and the quantum Hamiltonian is given as

$$\hat{H}_{\rm pen}(\hat{I}, \hat{\vartheta}) = \hat{H}_0(\hat{I}) + \hat{V}(\hat{I}, \hat{\vartheta}), \tag{3.37}$$

where

$$\hat{H}_0 = \frac{(\hat{I} - I_{r:s})^2}{2m_{r:s}}, \qquad \hat{V}(\hat{I}, \hat{\theta}) = \sum_{\ell=1}^{\infty} 2V_\ell(\hat{I}) \cos(r\ell\hat{\vartheta} + \phi_\ell). \tag{3.38}$$

The unperturbed eigenstate $|n\rangle$ of the operator $\hat{I} = -i\hbar d/d\vartheta$ fulfills the relation

$$\hat{I}|n\rangle = I_n|n\rangle = \hbar(n + 1/2)|n\rangle, \quad \hat{H}_0(\hat{I})|n\rangle = E_n^{(0)}|n\rangle, \tag{3.39}$$

where

$$E_n^{(0)} = \frac{\hbar^2}{2m_{r:s}}(n - n_{r:s}), \tag{3.40}$$

with $n_{r:s} + 1/2 \equiv I_{r:s}/\hbar$. The unperturbed eigenstate $|n\rangle$ is expressed using the plain waves in the ϑ-representation

$$\langle\vartheta|I\rangle = \frac{1}{\sqrt{2\pi}} \exp(i(n + 1/2)\vartheta). \tag{3.41}$$

Using this basis, we can apply the time-independent quantum perturbation theory. The matrix elements of the perturbation operator $\hat{V}$ are evaluated as

$$\begin{aligned}
V_{m,n} &\equiv \langle m|\hat{V}(\hat{I}, \hat{\vartheta})|n\rangle \\
&= \langle m| \sum_{\ell=1}^{\infty} 2V_\ell(\hat{I}) \cos(r\ell\hat{\vartheta} + \phi_\ell)|n\rangle \\
&= \sum_{\ell=1}^{\infty} \int_0^{2\pi} \int_0^{2\pi} d\vartheta' d\vartheta \; \langle m|2V_\ell(\hat{I})|\vartheta'\rangle\langle\vartheta'| \cos(r\ell\hat{\vartheta} + \phi_\ell)|\vartheta\rangle\langle\vartheta|n\rangle \\
&= \sum_{\ell=1}^{\infty} 2V_\ell(I_m) \int_0^{2\pi} \int_0^{2\pi} d\vartheta' d\vartheta \; \langle m|\vartheta'\rangle\delta_{\vartheta',\vartheta}\langle\vartheta|n\rangle \cos(r\ell\vartheta + \phi_\ell) \\
&= \frac{1}{2\pi} \sum_{\ell=1}^{\infty} 2V_\ell(I_m) \int_0^{2\pi} d\theta \; e^{-i(n-m)\theta} \cos(r\ell\vartheta + \phi_\ell) \\
&= \sum_{\ell=1}^{\infty} V_j(I_m)\delta_{|n-m|,r\ell}.
\end{aligned} \tag{3.42}$$

Therefore the matrix $V_{m,n}$ becomes a sparse one due to the selection made by delta function. Here we have used the formula

$$\int_0^{2\pi} d\theta \; e^{-im\theta} \cos(n\theta) = \pi\delta_{m,n}. \tag{3.43}$$

The first order perturbation formula for the wave function gives

$$|\Psi_n\rangle \simeq |n\rangle + \sum_{\ell \neq n} B_{n,r\ell} |n + r\ell\rangle, \tag{3.44}$$

where

$$\mathcal{B}_{n,r\ell} = \frac{V_{n+r\ell,n}}{E_n^{(0)} - E_{n+r\ell}^{(0)}}. \tag{3.45}$$

This result tells us that the state $|n\rangle$ directly couples with the excited states $|n+r\ell\rangle$ via the perturbation term V which represents the classical resonance.

Applying the perturbation formula (3.44) to constructing the local solution $|\Psi_L\rangle$ and $|\Psi_R\rangle$, and using the formula (3.21), we get an expression for the energy splitting as

$$\begin{aligned}
\Delta E_n &= \langle \Psi_n^L | \hat{H} | \Psi_n^R \rangle \\
&= \langle n | \hat{H} | n \rangle + \sum_{\ell \neq n} |\mathcal{B}_{n,r\ell}|^2 \langle n + r\ell | \hat{H} | n + r\ell \rangle \\
&= \Delta E_n^{(0)} + \sum_{\ell \neq n} |\mathcal{B}_{n,r\ell}|^2 \Delta E_{n+r\ell}^{(0)}.
\end{aligned} \tag{3.46}$$

The energy resonance, whose condition is given as $|E_n - E_{n+r\ell}| = 0$, leads to a strong coupling and invokes the spikes in the splitting curve. Especially, second and higher order perturbation corrections contain the coupling via a sequence of different resonance chains. Such coupling induces a bunch of spikes, which are interpreted as the origin of the enhancement of the tunneling rate in RAT theory [Mouchet et al. 2006, Schlagheck et al. 2011]. In order to improve the calculation based on such a RAT scheme, it was proposed to take into account the action dependence of the coupling coefficient $\mathcal{B}$ (see Ref. [Schlagheck et al. 2011]). However we do not go into details as we will mention the reason for it in the next section.

3.3 Resonance-assisted tunneling in the integrable system

As discussed above, RAT has been understood to as a mechanism accounting for the tunneling enhancement and is now widely accepted as a computational scheme to reproduce the splitting in non-integrable systems, Recently, the authors of [Le Deunff et al. 2013] pointed out that the predictability of RAT based on the

perturbation has some limitation, even if the systems is completely integrable. Additionally, they unveiled, based on semiclassical theory, that the tunneling splitting in an integrable system exhibits exponential dependence as a function of $\hbar$ accompanied by spikes. This result implies that staircase structures do not appear in integrable systems and the nature of tunneling in non-integrable systems are quite different from the integrable one.

To explore the origin of such a difference, let us consider the following one-dimensional Hamiltonian [Le Deunff et al. 2013]

$$H(q,p) = H_0(q,p) + \varepsilon H_1(q,p), \tag{3.47}$$

with

$$H_0(q,p) = \frac{1}{2}(\cos^2 p + \cos^2 q) + a(\cos^2 p + \cos^2 q)^2, \tag{3.48}$$

and

$$H_1(q,p) = (\cos^4 p - 6\cos^2 p \cos^2 q + \cos^4 q)\cos\phi - 4(\cos^3 p \cos q - \cos p \cos^3 q)\sin\phi. \tag{3.49}$$

Since the Hamiltonian (3.47) is one-dimensional, it is completely integrable. As shown in Fig. 3.5, the phase space portraits exhibit four symmetric wells in $(q,p) \in [-\pi,\pi) \times [-\pi,\pi)$ when we take $a < 0$. Each well has a local minimum energy $E = 0$ at centers $(q,p) = (\pm\pi/2, \pm\pi/2)$ and there is a local maximum between the stable fixed points $(q,p) = (\pm\pi/2, \pm\pi/2)$ and the unstable fixed points $(q,p) = (0, \pm\pi/2)$ and $(\pm\pi/2, 0)$. When $\varepsilon > 0$, a classical $r : s = 4 : 1$ resonance chain appears close to the local maximum. The relative orientation of the classical resonance chains is controlled by the parameter ϕ.

Since RAT theory does not take into account the orientation of the classical resonance, the treatment base on RAT could not explain differences originating from it. On the other hand, it was shown in [Le Deunff et al. 2013] that semiclassical (WKB) approximation well reproduces the splitting behavior.

To be concrete let us consider the eigenvalue problem

$$\hat{H}(\hat{q},\hat{p})|\Psi_n^{\pm}\rangle = E_n^{\pm}|\Psi_n^{\pm}\rangle, \tag{3.50}$$

for the quantized Hamiltonian (3.47). Since the Hamiltonian contains the cross terms of the variables q and

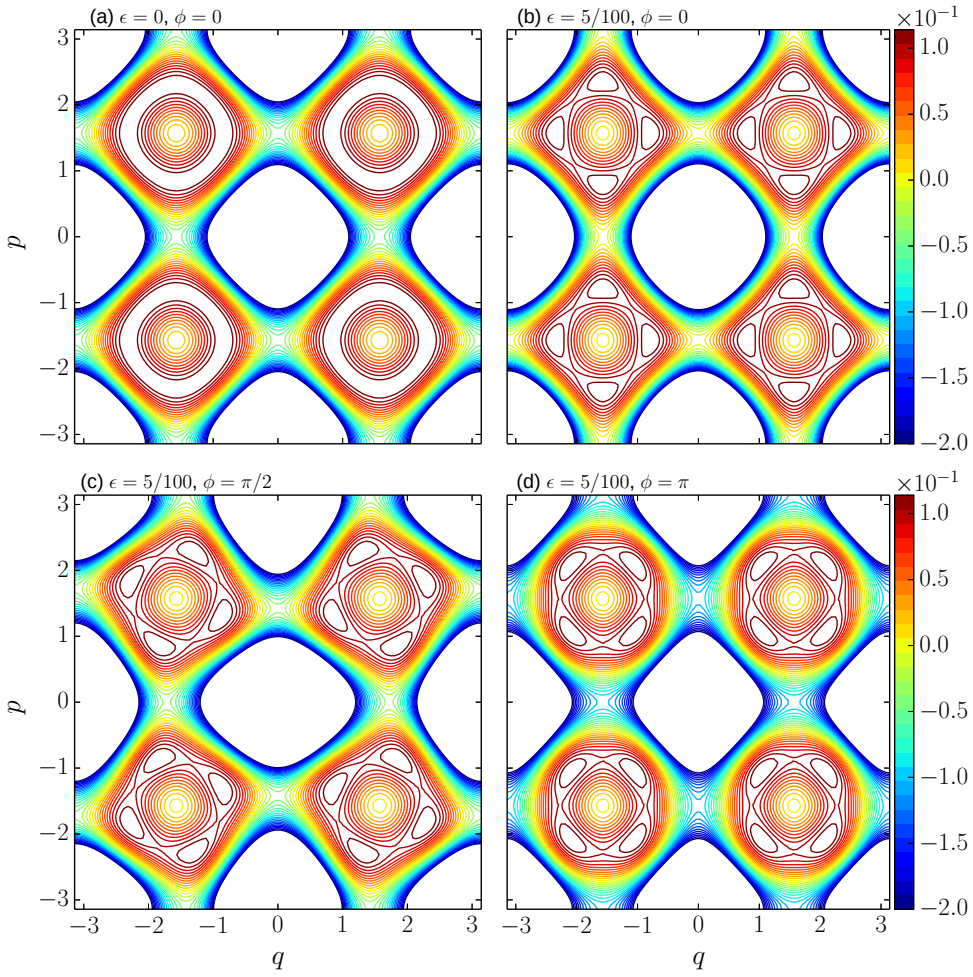

Figure 3.5: Phase space of the Hamiltonian (3.47) with the parameters (a) $\varepsilon = 0$ and $\phi = 0$, (b) $\varepsilon = 5/100$ and $\phi = 0$, (c) $\varepsilon = 5/100$ and $\phi = \pi/2$ and (d) $\varepsilon = 5/100$ and $\phi = \pi/2$. We do not draw the contour curves with $E < -0.2$ since classical resonances do not appear in this area.

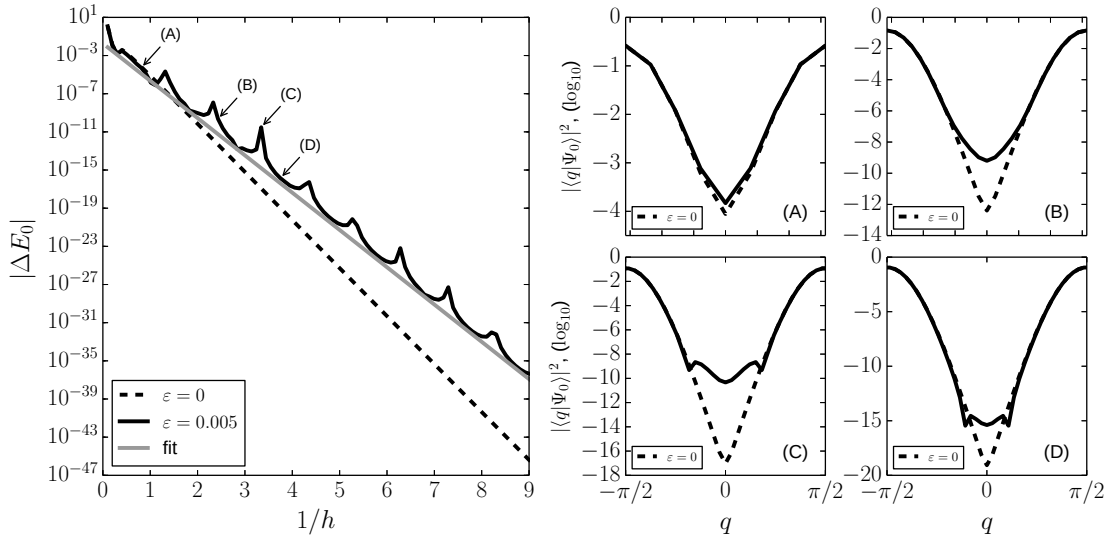

Figure 3.6: Left panel shows the tunneling splitting ΔE_0 between the ground state and the first excited state localizing at $(q, p) = (\pm\pi/2, \pi/2)$ with $\varepsilon = 5/1000$ (black solid line) and $\varepsilon = 0$ (black dashed line). Gray line indicates the curve the fitted to the splitting curve with $\varepsilon = 5/1000$ in a large $1/h$ regime. Right panels (A)-(D) show the eigenstate $|\Psi_0^+\rangle$ in q-representation for $1/h$, each of which value is indicated in the left panel.

p, we have to fix the ordering of operators to give the quantum mechanical Hamiltonian. Here we adopt

$$g(p)h(q) \mapsto \frac{1}{2}\left[g(\hat{p})h(\hat{q}) + h(\hat{q})g(\hat{p})\right], \tag{3.51}$$

for the product of two classical functions $g(p)$ and $h(q)$ [Shewell 1959, Weyl][4]. For the sake of simplicity, we only consider the parameter $\phi = 0$ case, and impose the periodic boundary condition on the region $(q, p) \in (-\pi, \pi] \times (0, \pi]$, in which phase space exhibits two symmetric wells. We then consider the tunneling splitting ΔE_0 of the ground state and the first excited state, both localizing in the center of inner well $(q, p) = (\pm\pi/2, \pi/2)$.

Figure 3.6 shows the splitting ΔE_0 as a function of $1/h$. For $\varepsilon = 0$, the splitting decays monotonically fitted by a single exponential function. However, for $\varepsilon > 0$ the splitting decays exponentially accompanied with periodic spikes. All the features have clearly been accounted for if one applies the semiclassical method

[4]If we ignore the symmetrization rule, the eigenstates do not have supports along the classical invariant curve.

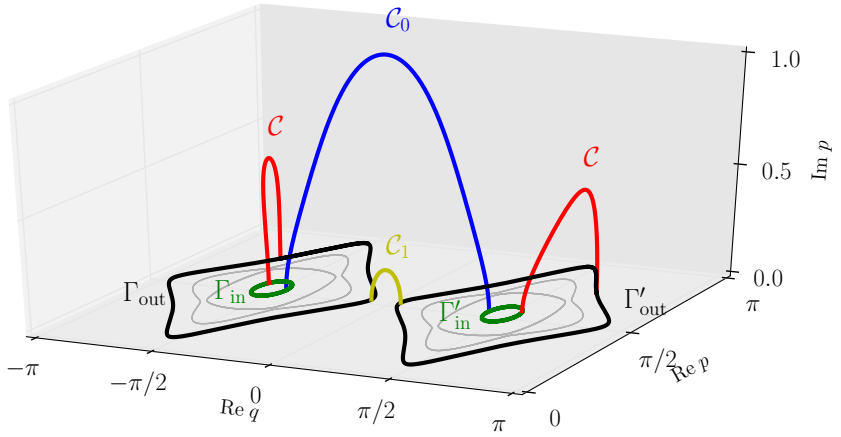

Figure 3.7: Trajectories projected onto the subspace of complex phase space $(\mathrm{Re}\, q, \mathrm{Re}\, p, \mathrm{Im}\, p)$ for Hamiltonian (3.47) with the parameters $a = -0.55$, $\varepsilon = 0.05$ and $\phi = 0$.

using complex paths [Le Deunff et al. 2013]. For $\varepsilon = 0$, the condition $H(q,p) = 0$ can be factorized into

$$\Phi(q,p) \equiv \cos^2 q + \cos^2 p = 0, \qquad \text{and} \qquad \Phi(q,p) \equiv \cos^2 q + \cos^2 p = -1/2a. \tag{3.52}$$

This function $\Phi(q,p)$ represents the invariant curves on the opposite side of the local maxima, which implies that the invariant curves are not connected even in the complex plane. Thus no tunneling connection between the inner and outer regions exists even though both are the surfaces with the same energy [Harada and Shudo private communications; 2015]. For $\varepsilon > 0$, the spikes appear as a result of the energetic resonance between the states localized in the inner well and outer region. The coupling strength could be evaluated using the imaginary action of complex trajectories which bridge classical disjointed equi-energy surfaces. Such trajectories are shown in Fig. 3.7.

As shown in Ref. [Brodier et al. 2002, Le Deunff et al. 2013], the coupling constant $\mathcal{B}$ is semiclassically evaluated as

$$\mathcal{B} = \frac{e^{-\sigma_{\mathcal{C}}/\hbar}}{2\sin\left\{(S_{\rm in} - S_{\rm out})/(2\ell\hbar)\right\}}, \tag{3.53}$$

where $\sigma_{\mathcal{C}}$, $S_{\rm in}$ and $S_{\rm out}$ are given using the contour integral

$$S_{\rm in} = \oint_{\Gamma_{\rm in}} \mathrm{Re}\, p\, d(\mathrm{Re}\, q), \qquad S_{\rm out} = \oint_{\Gamma_{\rm out}} \mathrm{Re}\, p\, d(\mathrm{Re}\, q), \tag{3.54a}$$

$$\sigma_{\mathcal{C}} = \frac{1}{2}\oint_{\mathcal{C}} [\mathrm{Re}\, p\, d(\mathrm{Im}\, q) + \mathrm{Im}\, p\, d(\mathrm{Re}\, q)], \tag{3.54b}$$

along the curves $\Gamma_{\rm in}$, $\Gamma_{\rm out}$ and $\mathcal{C}$ which are shown in Fig. 3.7. Note that the complex paths $\mathcal{C}_0$, $\mathcal{C}$ and $\mathcal{C}_1$ are shown in Fig. 3.7 are given as the time evolution of the classical trajectory in the pure imaginary time direction. Recall that the semiclassical expression for the splitting is given by Eq. (3.13) as discussed in section 3.1, we finally reach the semiclassical perdition for the splitting

$$\begin{aligned}\Delta E &= \Delta E_{\rm in} + |\mathcal{B}|^2 \Delta E_{\rm out} \\ &\sim A_0 e^{-\sigma_{\mathcal{C}_0}/\hbar} + \left\{ 4\sin^2\left(\frac{S_{\rm in} - S_{\rm out}}{2\ell\hbar}\right)\right\}^{-1} A_1 e^{-(\sigma_{\mathcal{C}_1}+2\sigma_{\mathcal{C}})/\hbar},\end{aligned} \tag{3.55}$$

where $\sigma_{\mathcal{C}_0}$ and $\sigma_{\mathcal{C}_1}$ are given by the contour integrals

$$\sigma_{\mathcal{C}_0} = \frac{1}{2}\oint_{\mathcal{C}_0} [\mathrm{Re}\, p\, d(\mathrm{Im}\, q) + \mathrm{Im}\, p\, d(\mathrm{Re}\, q)], \quad \sigma_{\mathcal{C}_1} = \frac{1}{2}\oint_{\mathcal{C}_1} [\mathrm{Re}\, p\, d(\mathrm{Im}\, q) + \mathrm{Im}\, p\, d(\mathrm{Re}\, q)], \tag{3.56}$$

along the complex curve $\mathcal{C}_0$ and $\mathcal{C}_1$. Also the amplitude factors A_0 and A_1 are given by Eq. (3.14) and these factors are in proportion to $\hbar$.

Typically, the imaginary action $\sigma_{\mathcal{C}_0}$ associated with the connection $\Gamma_{\rm in}$ and $\Gamma'_{\rm in}$ is greater than the imaginary action $\sigma_{\mathcal{C}_1} + 2\sigma_{\mathcal{C}}$ which represents bypassing route via classical resonances. Therefore, the slope of the splitting curve is determined by the minimum imaginary action for the latter in the semiclassical limit $\hbar \to 0$. We also notice the condition $|S_{\rm in} - S_{\rm out}| = 2\ell\hbar$ (ℓ is an integer) makes the coupling constant $\mathcal{B}$ diverge, which invokes spikes in the splitting curve. As discussed above, the classical resonance induces the coupling between the inner well and the outer region, which gives the different slop in the splitting curve compared to the system without classical resonances ($\varepsilon = 0$). RAT is realized in this way. Therefore, we may say that the overall slope of splitting curve becomes large if classical resonance are present.

It would be worth mentioning that the splitting curve for $\varepsilon > 0$ exhibits a crossover from one slope to another. In a small $1/h$ regime, the slope can be well fitted by the one for $\varepsilon = 0$, whereas the best fit curve, colored in gray in Fig. 3.6, shows another slope in the large $1/h$ regime. This behavior might be understood

from Eq. (3.55), if semiclassical approximation works in the large $\hbar$ regime. As discussed above, there exist two different instanton complex paths with different imaginary actions. In a small ε regime, it can happen that the splitting curve $\Delta E_{\rm in}$ is larger than $\Delta E_{\rm out}$ in spite of the magnitude relation of imaginary actions. This is because the coupling amplitude comes into play in a relatively small $1/h$ regime. This crossover may invoke the plateau discussed in the previous section 3.2 (see also Fig. 3.4). However the origin and underlying mechanism entirely differs from the non-integrable one. This topic will be discussed in chapter 5 closely.

Right panels in Fig. 3.6 show the eigenstate of the integrable system (3.47). As shown in Fig. 3.6(A) the eigenstate for $\varepsilon = 5/1000$ and the eigenstate for $\varepsilon = 0$ coincide with each other. On the other hand, the amplitude of the eigenstate ($\varepsilon > 0$) around $q = 0$ becomes large compared to the $\varepsilon = 0$ one. This behavior could also be understood based on the semiclassical argument. The WKB solution $|\Psi_n^{L/R}\rangle$ localizing on the left/right well is written as a linear combination

$$|\Psi_n^{L/R}\rangle \simeq |\Psi_{\rm in}\rangle + \mathcal{B}|\Psi_{\rm out}\rangle, \tag{3.57}$$

where $|\Psi_{\rm in}\rangle$ and $|\Psi_{\rm out}\rangle$ denote the WKB wave functions associated with the curves $\Gamma_{\rm in}$ and $\Gamma_{\rm out}$, respectively. For a large $\hbar$ regime, the WKB solution $|\Psi_{\rm in}\rangle$ might come into play in the whole q regime as discussed above (see Fig. 3.6(A)) For a small $\hbar$ regime, on the other hand, the contribution $\mathcal{B}|\Psi_{\rm out}\rangle$ emerges around $q = 0$ (see Fig. 3.6(B)-(D)). We also notice that the characteristic structure of the eigenstate around $q = 0$ does not change significantly after the crossover of the splitting curve with $1/h$, and all of the eigenstates form a concave structure around $q = 0$. These behaviors imply that the WKB solution $|\Psi_{\rm out}\rangle$ exhibits a exponential decaying tail at $q = 0$ as expected.

On the other hand, it should be noted that the eigenstate of the quantized Harper map forms a convex structure at $q = 0$ on the plateau of the splitting curve, as shown in Fig. 3.4. The integrable (WKB) eigenstates localizing in the inner well (blue region in Fig. 3.3) can not make a concave structure, because such integrable eigenstates take the exponentially decaying tail since the position $q = 0$ is classically forbidden. Therefore, the convex structure implies the coupling with the state localizing in the outer well (see the red region in Fig. 3.3)[5]. In contrast, RAT theory is not capable of treating the tunneling beyond the separatrix

[5] As demonstrated by the one-dimensional double well system (see Fig. 3.1), the eigenstates a convex structure at $q = 0$, since $q = 0$ is classically allowed region for energy greater than saddle point energy.

or the chaotic sea. On the basis of these observations, we reach a quite different perspective for tunneling in the non-integrable system, which will be closely discussed in the following sections:

(i) The authors of Ref. [Brodier et al. 2002] pointed out that semiclassical theory could not make use of the instanton path because of emergence of the natural boundary. which was also conjectured in Ref. [Creagh 1998]. As an alternative to approach, RAT theory was developed performing integrable approximation around each classical resonance. The validity of RAT theory is justified in an integrable system via semiclassical theory [Le Deunff et al. 2013]. However, it is still an issue of debate whether the natural boundary is avoidable or not. We will revisit this issue in section 4.1.

(ii) One interpretation for the appearance of plateaus would be that it is a kind of phenomena that might be called quantum overlapping resonance; a bunching of spikes, each of which is associated with individual quantum resonances, turns out to create plateaus. This topic will be discussed in section 5.2 and our claim shows that the origin of the spikes and the plateau in the splitting curve have different origins.

(iii) In the theory of RAT, the coupling is only treated locally around the classical resonances, and also one cannot take into account the coupling beyond the separatrix or the chaotic sea as discussed above. In other words, the theory of RAT does not take into account the coupling between the inner (see blue regions in Fig. 3.3) and outer torus regions (see red regions in Fig. 3.3). However, we show that the coupling between the inner and outer tours regime is essential to explain the plateau structure and the origin of the enhancement of the tunneling probability in the non-integrable systems This topic will be discussed in the section 5.3.

Chapter 4

Tunneling effect in non-integrable systems

Quantum tunneling in non-integrable systems has been studied for the last two decades. We here focus on two topics. In section 4.1, we will discuss the relation between the tunneling effect and natural boundaries or KAM tori. In section 4.2, we will discuss the instanton-noninstanton transition, which characterizes the enhancement of the tunneling probability in non-integrable systems.

4.1 Natural boundaries and tunneling effect

As discussed in section 3.3, in the theory of RAT one performs the integrable approximation around the "visible" classical resonance. However, it is non-trivial whether the tunneling effect can be treated with an integrable approximation or not. In this section, we reconsider the complex structure of invariant manifolds for a pendulum Hamiltonian and the corresponding non-integrable map.

Let us consider the simple pendulum Hamiltonian

$$H(q,p) = \frac{p^2}{2} + k\cos(q). \tag{4.1}$$

We consider the eigenstate for associated energy $E > k$. The semiclassical (WKB) solution of the wave

function in the p-representation is expressed as

$$\Psi(p) \simeq \frac{A}{\sqrt{q}} \exp\left(\frac{i}{\hbar}\int^{p} dp'\, q(p')\right) + \frac{B}{\sqrt{q}} \exp\left(-\frac{i}{\hbar}\int^{p} dp'\, q(p')\right) \tag{4.2}$$

where A and B are contents and the integration is taken along a curve

$$q(p) = \pm\cos^{-1}\left(\frac{1}{k}\left\{E - \frac{p^2}{2}\right\}\right). \tag{4.3}$$

where

$$q(p) \text{ takes } \begin{cases} \text{a real value in } |E - \frac{p^2}{2}| < k \\ \text{a pure imaginary value in } |E - \frac{p^2}{2}| > k, \end{cases}$$

for $E \in \mathbb{R}$. The pure imaginary region describes the tunneling process between the symmetric regions. Figure 4.1 shows the curve (4.3) with energy $E = 0.2$ (see blue curves in Fig. 4.1) and the surface of analytic continuation of the function (4.3) into complex plane. As shown in Fig. 4.1, the symmetric curves (see blue curves in Fig. 4.1) are connected by the complexified manifold given by Eq. (4.3). The instanton path is a path running along this complexified manifold (see the red curve in Fig. 4.1).

As discussed in sections 2.1 and 3.2, KAM tori survive under a small perturbation, however, it has natural boundary in the complex plain. Due to the breaking up of complexified invariant manifolds connecting different real tori, the instanton path is disrupted somewhere in the complex space. To demonstrate it, let us consider the symmetrized version of the standard map

$$f : f_V(\frac{1}{2}) \circ f_T(1) \circ f_V(\frac{1}{2}), \tag{4.4}$$

where $f_V(\tau) : (q,p) \mapsto (q, p + \tau V'(q))$ and $f_T(\tau) : (q,p) \mapsto (q + \tau T'(p), p)$ are trivial symplectic maps (see also Appendix B). The prime stands for the derivative of the function and we take the functions as $T(p) = p^2/2$ and $V(q) = k\cos q$. In this case, phase space is almost filled by KAM tori and there are no visible classical resonance and chaotic regions.

Figure 4.2 shows the analytic continuation of a KAM curve with frequency $\Omega = 2\pi \times 0.096540293\cdots$ into the complex plain in the region satisfying $\theta < \theta^*$. Unlike the case of the integrable system the instanton path along the complexified KAM curve encounters a natural boundary. As a result of analytic connection

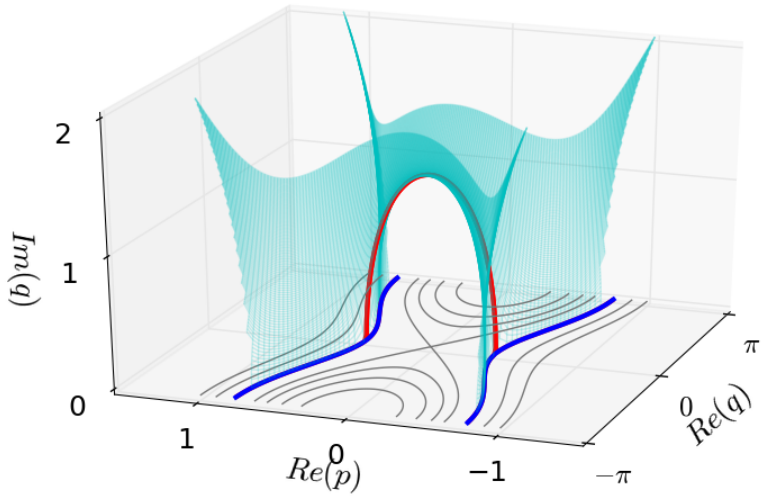

Figure 4.1: Complexified manifold (4.3) projected onto the subspace $(\mathrm{Re}\ q, \mathrm{Re}\ p, \mathrm{Im}\ p)$. The blue curves denote the invariant curves with energy $E = 0.2$. The instanton path is indicated as the red curve. Here we take a parameter as $k = 0.1$.

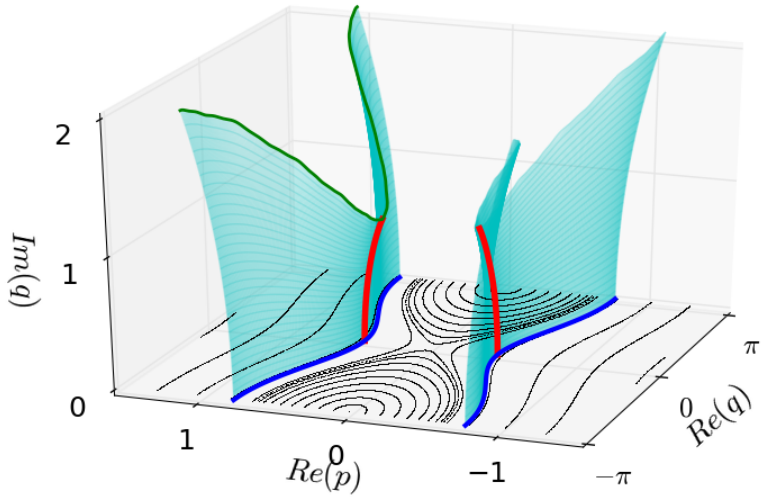

Figure 4.2: Complexified manifold of a KAM curve projected onto the subspace $(\mathrm{Re}\ q, \mathrm{Re}\ p, \mathrm{Im}\ p)$ (cyan surface) and the associated natural boundary (green curve). "Surviving" instanton path is shown in the red curve. Blue curves denote KAM curves with frequency $\Omega = 2\pi \times 0.096540293\cdots$. Here we take perturbation strength as $k = 0.1$.

between the symmetric tori breaks.

To consider the tunneling effect in this situation, let us introduce a symmetrized version of the quantum map

$$\hat{U} = e^{-\frac{i}{2\hbar}V(q)} e^{-\frac{i}{\hbar}T(p)} e^{-\frac{i}{2\hbar}V(q)}, \tag{4.5}$$

which is a quantum counterpart of the classical map (4.4). We then numerically solve the eigenvalue problem

$$\hat{U}|\Psi_n\rangle = u_n|\Psi_n\rangle. \tag{4.6}$$

For reference, we also consider the eigenvalue problem for the associated effective integrable Hamiltonian given as (4.6)

$$\hat{H}^{(M)}_{\text{eff}}|J^{(M)}_n\rangle = E_n|J^{(M)}_n\rangle. \tag{4.7}$$

The construction of the effective integrable Hamiltonian is discussed in Appendix B. Note that when $M = 1$, the effective integrable Hamiltonian is nothing more than the quantized pendulum Hamiltonian (4.1).

Figure 4.3 shows some eigenstates $|\Psi_n\rangle$ localizing in KAM curves and associated integrable eigenstates $|J^{(M)}_n\rangle$. For a large $\hbar$ regime (see Fig. 4.3(a1)), the eigenstate $|\Psi_n\rangle$ seems to be well approximated by the integrable eigenstate $|J^{(M)}_n\rangle$. For the semiclassical regime $\hbar \to 0$, on the other hand, the amplitude of $|\Psi_n\rangle$ around $p = 0$ becomes drastically large compared with the integrable one (see Fig. 4.3(b2) and (b3)). As mentioned above that natural boundaries break the instanton path, so it was conjectured that tunneling probability may be influenced [Creagh 1998]. Indeed, the authors of Ref. [Shudo and Ikeda 2012] demonstrated that the enhancement of the tunneling probability, is actually observed. They have introduced the ratio $\chi(q) = |\Psi_n(q)|^2/|J^{(M)}_n(q)|^2$, and showed that it becomes greater than unity as the position of observation comes close to natural boundaries (see Fig. 4.4 a complexified KAM curve and associated natural boundary in case of the Hénon map)

Figure 4.3 indicates that the dissociation point p, which satisfies $\chi(p) > 1$, move away from $p = 0$ toward certain $|p| > 0$ with decrease in $\hbar$. This behavior is similar to Hénon map [Shudo and Ikeda 2012] and is expected that the dissociation point comes close to natural boundaries, however, it would not be an easy task to check whether or not the same is true for the case of eigenstates localized on transversal invariant curves, since the effective integrable Hamiltonian $\hat{H}^{(M)}_{\text{eff}}$ does not provide a good approximation comparable to the inner torus case.

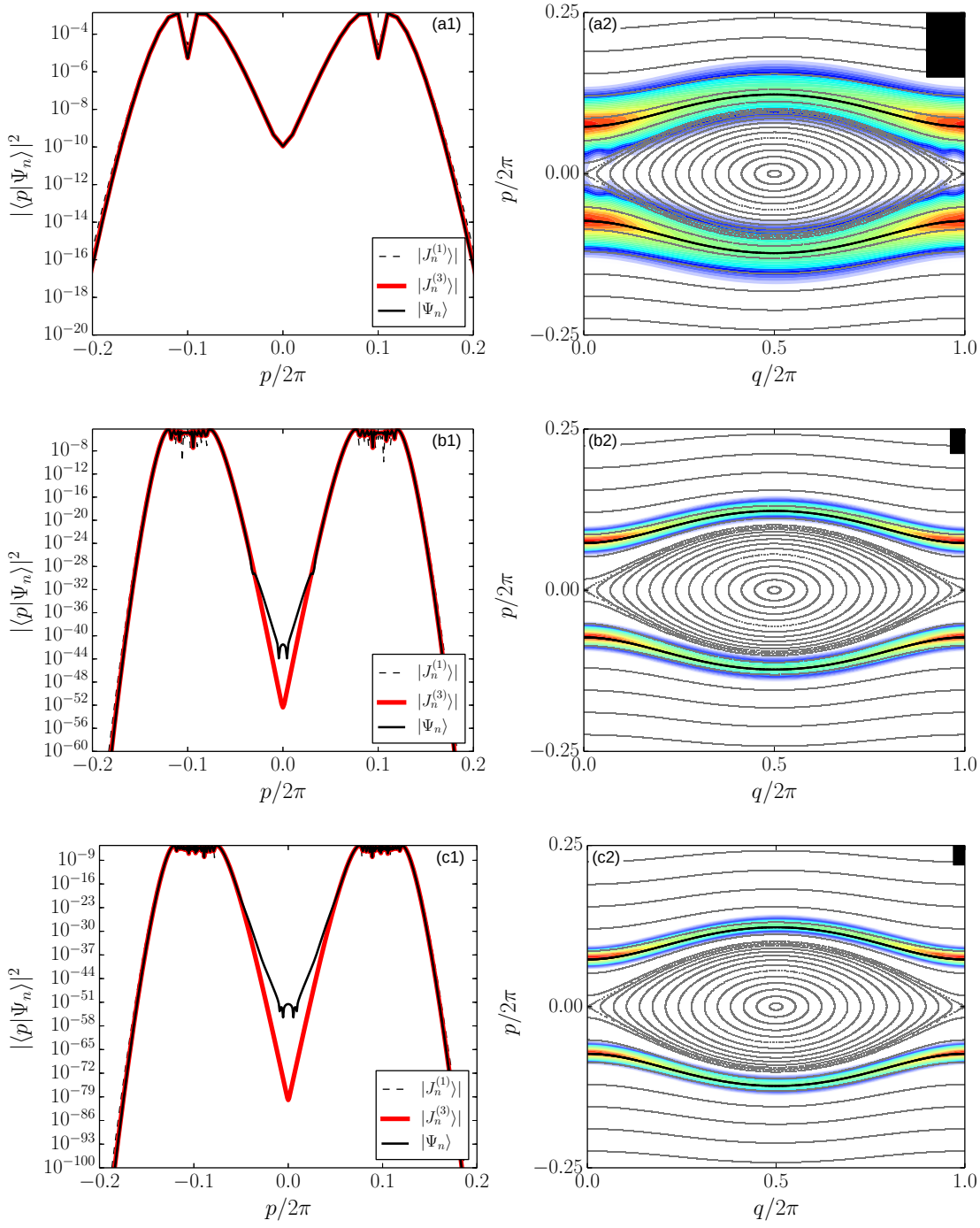

Figure 4.3: Left panels show the eigenstates $|\Psi_n\rangle$ in the p-representation for $k = 0.1$ (black solid curve) and associated integrable eigenstates $|J_n^{(M)}\rangle$ with (a1) $\hbar = 2\pi/100$, (a2) $\hbar = 2\pi/700$ and (a3) $\hbar = 2\pi/1100$. Right panels show the corresponding eigenstate $|\Psi_n\rangle$ in Husimi-representation. Each eigenstate $|\Psi_n\rangle$ localizes on a KAM curve indicated byblack curve. The black box put in the upper right corner in right panels indicates the size of the effective Planck's constant h.

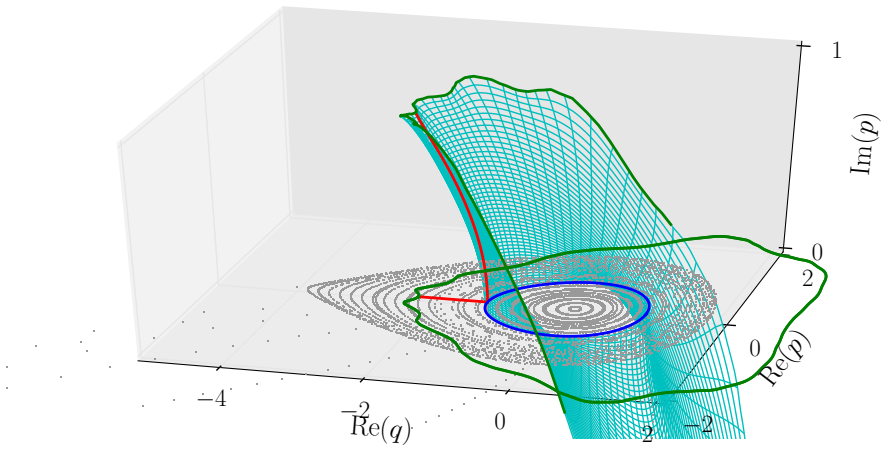

Figure 4.4: A complexified KAM curve projected onto the subspace $(\mathrm{Re}\ q, \mathrm{Re}\ p, \mathrm{Im}\ p)$ (cyan surface) for the Hńeon map in a symmetrized form. Parameters are chosen as $\epsilon = 0.1$ and $\tau = 1$. Blue and green curves denote the KAM curve with frequency $\Omega = 2\pi \times 0.6186307288139515\cdots$ and the natural boundary. "Surviving" instanton path is shown in red curve. For reference, the natural boundary and "surviving" instanton path are projected onto $(\mathrm{Re}\ q, \mathrm{Re}\ p)$-plain.

4.2 Instanton-noninstanton transition

As shown in Fig. 3.4, the tunneling probability is drastically enhanced as compared with the integrable one, and the splitting curve forms a staircase-like structure as discussed in the previous section 3.2. It is important to note that such enhancement is observed even in the system sufficiently close to the integrable limit. In this section, we show that the enhancement can be understood as a crossover from instanton tunneling to the mechanism specifically emerging in nonintegrable systems. The underling mechanism of the former is essentially the same although the instanton path no longer exists, and the origin of the latter will closely examined in the next chapter. We call such a crossover the instanton-noninstanton (I-NI) transition hereafter. Below, to explain the I-NI transition we take the quantum version of the Hénon and standard maps, each of which is defined as

$$\hat{U} = e^{-i\tau p^2/4\hbar} e^{-i\tau V(q)/\hbar} e^{-i\tau p^2/4\hbar}, \quad \text{and} \quad \hat{U} = e^{-i\tau V(q)/2\hbar} e^{-i\tau p^2/2\hbar} e^{-i\tau V(q)/2\hbar}. \tag{4.8}$$

Here we take the potential function as $V(q) = 2q^2 + q^3/3$ for the Hénon map and as $V(q) = \cos q$ for the standard map, respectively. In spite of the different nature of tunneling in the two systems, the

characteristic staircase structure found in tunneling probability is common. Our basic tool to analyze is to observe eigenfunctions under the bases obtained by renormalizing the integrable part as much as possible. Such basis functions can be constructed using the Baker-Campbell-Hausdorff (BCH) expansion, as closely explained below.

We first demonstrate aspects of tunneling probability in eigenstates both in the Hénon and standard maps. Figures 4.5(a) and (b) shows the representative tunneling probability as a function of the quantum number as a typical example of the tunneling characteristics computed for the Hénon map and the standard map. Although these examples are nonintegrable, we here examine weakly nonintegrable regimes with small τ as displayed in the right panels of Fig. 4.5. Therefore, the classical invariant tori still remain according to the celebrated KAM theory, and good quantum numbers can be assigned to each quantum eigenstate following the Einstein-Brillouin-Keller (EBK) quantization rule.

In the limit of vanishing nonintegrability $\tau \to 0$, both systems are approximated by one-dimensional systems with potential barriers which classically bound the eigenstates but quantum mechanically allow to tunnel by the instanton mechanism as is usual in one-dimensional systems, which will be discussed later. However, as the quantum number n decreases from the highest exited state with the energy just below the potential barrier height, a transition occurs at a characteristic quantum number, denoted hereafter by $n_{\rm c}$, and the tunneling probability suddenly deviates from the instanton probability forming a *plateau*. We call the first transition from the instanton tunneling to some unknown type of tunneling as the instanton-noninstanton (I-NI) transition. The common feature seems to be quite paradoxical in the sense that the low lying states distant from the saddle point located on the barrier top, which is the very origin of the classical nonintegrability exhibit non-instanton tunneling, while the highly excited states close to the saddle point obey the instanton tunneling. Moreover, in both examples the number of the eigenstates in the instanton regime $n_{\rm max} - n_{\rm c}$ is insensitive to $\hbar$, where $n_{\rm max}$ is the maximum quantum number of the classically bounded states inside the potential well.

To understand the I-NI transition the most natural way is to apply a perturbation theory based on an integrable limit which has the instanton as the tunneling mechanism. The crudest integrable approximation of symmetrized U in the small limit of the nonlinear parameter τ is $\hat{U}_1 = e^{-i\hat{H}_1\tau/\hbar}$ where $\hat{H}_1 = p^2/2 + V(q)$, but the difference $|\hat{U} - \hat{U}_1| \sim \tau/\hbar$ is too large to afford any significant result for the exponentially small tunneling effect. We therefore develop a systematic expansion with respect to the smallness parameter

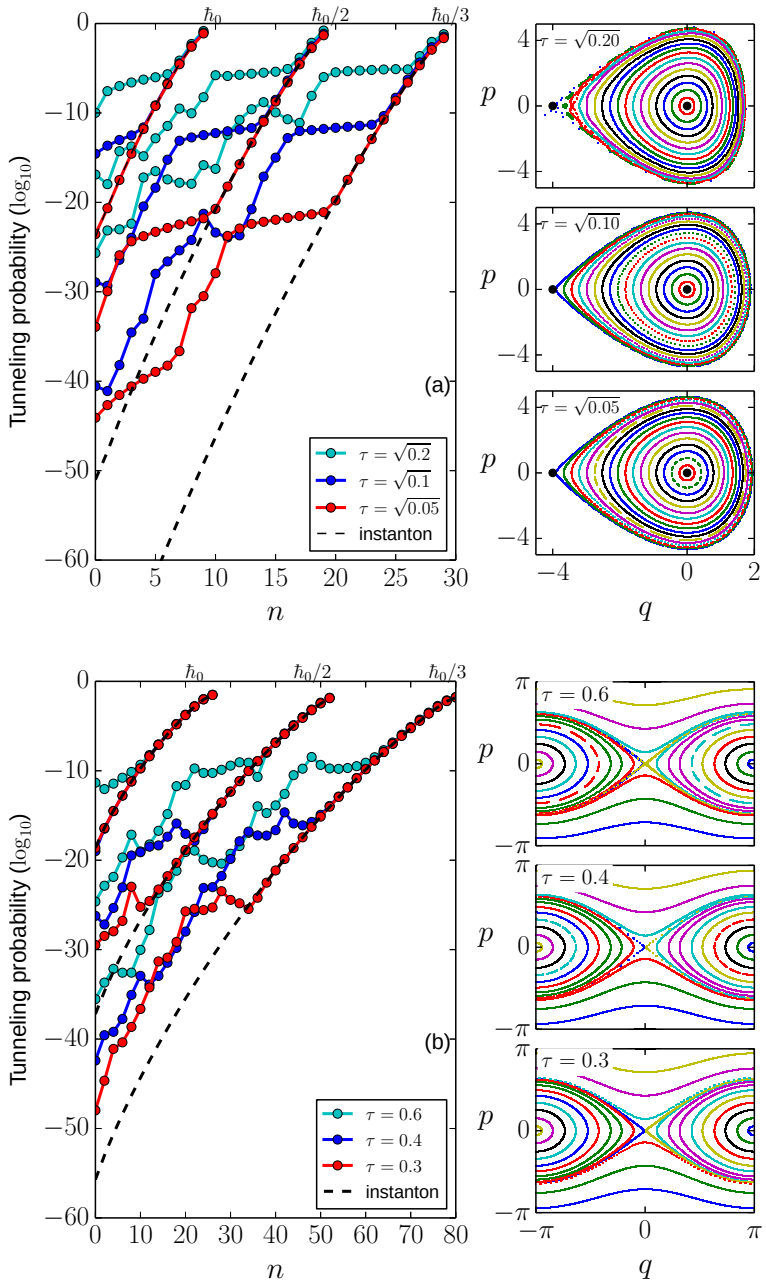

Figure 4.5: The tunneling probability (in $\log_{10}$) for the eigenstates of Eq. (4.8) vs. the quantum number n (less than $n_{\max}$) for (a) the Hénon and (b) the standard map with various values of $\hbar$ in the unit of $\hbar_0$ and the nonlinear parameter τ. The tunneling probability is computed in the asymptotic region ($q \ll -4$) for the Hénon map and at the potential top $q = 0$ for the standard map (only the even parity eigenfunctions in the q-representation are consider). Here $\hbar_0 = 0.63\tau$ for the Hénon map and $\hbar_0 = 3\pi\tau/25$ for the standard map. The right panels respectively show the phase space portrait associated classical maps.

τ which renormalizes the integrable part of $\hat{U}$ into a single effective Hamiltonian as much as possible. A possible candidate to achieve this is the BHC expansion (see also Appendix B), which approximates the product of exponential operators (4.8) systematically in terms of a single exponential operator expressed by an effective Hamiltonian, which coincides with H_1 in the lowest order approximation.

Below, we apply a renormalized perturbation theory to the Hénon and standard maps. They are both simplest classes of maps exhibiting quite different nature of tunneling, which is understood by the simplest one-dimensional Hamiltonian $H_1 = p^2/2 + V(q)$: the Hénon map has the cubic potential with the bottom at $q = 0$ and tunneling is an irreversible transport of probability toward $q = -\infty$ going over the barrier at $q = -4$. For the standard map the 4π periodic boundary condition is imposed in the q direction. Then its cosine potential gives two symmetric valleys with bottoms at $q = \pm\pi$ and separated by two symmetric barriers at $q = 0$ and $q = 2\pi$.

We can show that the BHC expansion of $\hat{U}$ leads to an effective polynomial Hamiltonian

$$H_{\rm eff}^{(M)} = \sum_{\ell=1,3,..,M} (-\tau)^{(\ell-1)} H_\ell \tag{4.9a}$$

with

$$H_\ell = \sum_{k,i,j=0}^{k_\ell, i_{\ell k}, j_{\ell k}} \hbar^k C(\ell,k,i,j) p^i q^j, \tag{4.9b}$$

where $C(n,k,i,j)$ is the set of coefficients of $O(1)$, and the terms of $k = 0$ provide the classical Hamiltonian. Note that only the odd powers of τ appear in the sum because of the symmetrized form of $\hat{U}$. The unitary operator thus induced is given as $\hat{U}_M = e^{-iH_{\rm eff}^{(M)}\tau/\hbar}$. We do not introduce any artificial absorbers and/or absorbing boundary conditions, which may crucially influence the original dynamics (see the Appendix A).

Once the renormalized Hamiltonian $H_{\rm eff}$ is obtained, we straightforwardly develop a perturbation theory taking the difference $\Delta\hat{U}_M = \hat{U} - \hat{U}_M$ as the perturbation. Then the lowest-order perturbative eigenfunction is given as

$$|\Psi_n^{(M)}\rangle = |J_n^{(M)}\rangle + |\Delta\Psi_n^{(M)}\rangle, \tag{4.10a}$$

with

$$|\Delta\Psi_n^{(M)}\rangle = \sum_\ell \frac{\langle J_\ell^{(M)}|\Delta\hat{U}_M|J_n^{(M)}\rangle}{e^{-iE_\ell^{(M)}\tau/\hbar} - e^{-iE_n^{(M)}\tau/\hbar}}|J_\ell^{(M)}\rangle, \tag{4.10b}$$

where $|J_n^{(M)}\rangle$ and $E_n^{(M)}$ are, respectively, the eigenfunction and the energy eigenvalue of the 1D integrable Hamiltonian $H_{\rm eff}^{(M)}$.

If τ is not so large, there appear two sorts of fixed points in classical phase space: stable and unstable fixed point $(0,0)$ and $(-4,0)$ for the Hénon map, and $(\pm\pi,0)$ and $(0,0)$ for the standard map respectively. As shown in the Fig. 4.5, KAM tori predominate phase space in both cases and KAM regions are encircled by the stable manifold W^s and the unstable manifold W^u of the saddle fixed point. KAM tori support quantum eigenstates, each of which satisfies the EBK quantization condition $\int q\,dq/2\pi = (n+1/2)\hbar$ $(n = 0, 1, \cdots, n_{\max})$. They all have finite tunneling life-times (Hénon map) or tunneling splittings (standard map) due to the tunneling via the instanton trajectory, which is very well approximated by the lowest order instanton solution $p = \sqrt{2(V(q) - E_n)}$ or $H_1(\mathrm{i}p, q) = E_n$ (E_n is the quantized energy). A notable feature of the renormalized Hamiltonian $H_{\rm eff}^{(M)}(p,q)$ is that tunneling tails of eigenfunctions $\langle q|J_n^{(M)}\rangle$ do not change very significantly even if one increases the order of renormalization M. However, according to Eq. (4.10), the application of perturbation changes drastically the tunneling tail of eigenstates with increase in M.

In Fig. 4.6 we show a typical result of renormalized perturbation theory. For lower-order approximation, $\hat{U} - \hat{U}_M$ is too large to control correctly the exponentially small tunneling component and so the perturbative solution yields quite absurd results. But as the order M of renormalization increases the perturbative solution converges to the exact eigenfunction $|\Psi_n\rangle$ obtained by numerical diagonalization and reproduces even the complicated oscillations at the tunneling tail as demonstrated in Figs. 4.6 (a1) and (a2). The higher-order renormalized perturbation calculation also succeeded in reproducing the exact tunneling probability in a rather wide regime including both I (instanton) and I-NI transition regions. (See Figs. 4.6 (b1) and (b2)).

The success of the perturbation theory means that the origin of the I-NI transition may be resolved into integrable bases: according to Eq. (4.10) we define the *contribution spectrum* representing the amount of

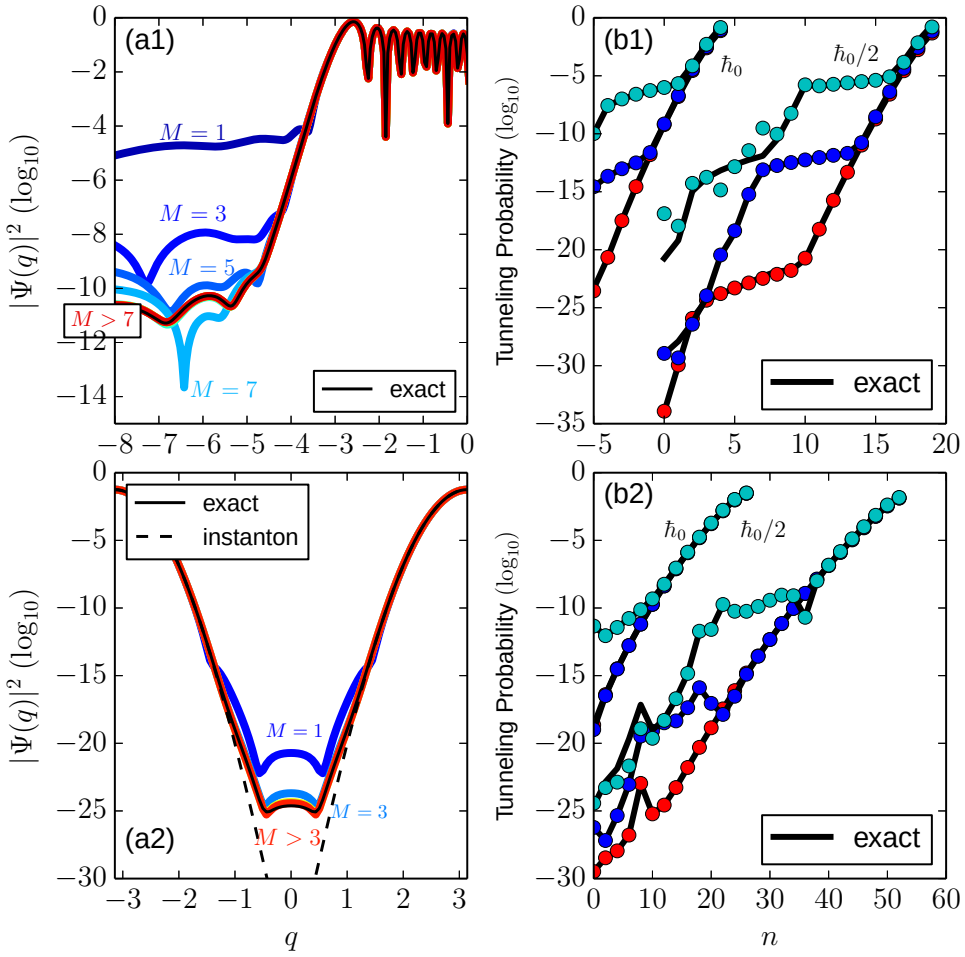

Figure 4.6: The convergence of tunneling tail to the exact numerical one (black) with increase in M in case of (a1) $n = 13$-th excited state of the Hénon map with $\tau = \sqrt{0.1}$ and $\hbar = \hbar_0/2$, and (a2) the ground state of standard map with $\tau = 0.6$ and $\hbar = \hbar_0/2$. The exact and higher order renormalized perturbative results are not distinguishable with each other. Right-hand panels show the probability amplitude of tunneling tail of exact numerical diagonalization (black lines) and of perturbation calculation as a function of quantum number (less than $n_{\max}$) in case of (b1) the Hénon map with the order $M = 21$, and (b2) the standard map with the order $M = 7$. In (b1) the quantum number is shifted by -5 for $\hbar_0$, and so $n = -5$ means $n = 0$ for $\hbar_0$.

contribution from the ℓ-th eigenstate of the integrable model to the n-th perturbative eigenfunction:

$$\begin{aligned} \mathrm{Con}_{\ell,n}^{(M)} &\equiv \langle\!\langle |\langle q|J_\ell^{(M)}\rangle| \rangle\!\rangle |\langle J_\ell^{(M)}|\Psi_n^{(M)}\rangle| \\ &\simeq \begin{cases} \langle\!\langle |\langle q|J_\ell^{(M)}\rangle| \rangle\!\rangle |\langle J_\ell|\Delta\Psi_n^{(M)}\rangle| & (\text{if } \ell \neq n), \\ \langle\!\langle |\langle q|J_\ell^{(M)}\rangle| \rangle\!\rangle & (\text{if } \ell = n), \end{cases} \end{aligned} \tag{4.11}$$

where $\langle\!\langle \cdots \rangle\!\rangle$ means to take average over a range of q in the asymptotic region (Hénon map) or around $q = 0$ (standard map).

We discuss closely how the renormalized perturbation theory describes the I-NI transition by taking the contribution spectrum of the Hénon map as an example. Figure 4.7(a) shows how the contribution spectrum $\mathrm{Con}_{\ell,n}^{(M)}$ $(0 \leq \ell \leq n_{\max})$ varies with the order of renormalization M at two representative quantum numbers n before and after the I-NI transition. A quite interesting fact is that for $M = 1$ the largest contribution comes from a broad peak centered at $\ell = n^*$, where n^* is the number of a quantum state just above the threshold of dissociation $n = n_{\max}$. However, with increase in the renormalization order M, the transition matrix elements $|\langle J_\ell^{(M)}|\Delta\hat{U}_M|J_n^{(M)}\rangle|$ are remarkably quenched, and the peak at $\ell = n^*$ is reduced in the logarithmic scale and finally overwhelmed by the very sharp peak at $j = n$, which means that the contribution from instanton of the integrable basis $\langle q|J_n^{(M)}\rangle$ is predominant in the tunneling process. On the other hand, at n less than a critical quantum number n_{c} the quenching of the transition matrix element can no longer reduce the peak at $\ell = n^*$ less than the instanton peak, and the contribution to tunneling is attributed to the broad peak around $\ell = n^*$. The competition between the two peaks explains the characteristics of I-NI transition. It should be emphasized that without remarkable quenching of the transition matrix element by renormalization the instanton phase is absent and the I-NI transition cannot be observed.

Since the above threshold state $|J_{n^*}^{(M)}\rangle$ is connected with $q = -\infty$ by real classical paths, $|\langle q|J_{n^*}^{(M)}\rangle| \sim O(1)$ and so the peak strength $\mathrm{Con}_{n^*,n}^{(M)}$ at n^* is approximated by the transition matrix element $|\langle J_n^{(M)}|\Delta\hat{U}_M|J_{n^*}^{(M)}\rangle|$. Figure 4.7(b) plots $|\langle J_n^{(M)}|\Delta\hat{U}_M|J_{n^*}^{(M)}\rangle|$ at just above the threshold for various values of M. The instanton peak strength $\langle\!\langle |\langle q|J_n^{(M)}\rangle| \rangle\!\rangle$ is also shown as a function of n, which does not significantly depend on M as mentioned above.

With increase in M, the curve $|\langle J_n^{(M)}|\Delta\hat{U}_M|J_{n^*}^{(M)}\rangle|$ vs n is largely deformed to show a very characteristic structure: it decreases steeply as n decreases below $n_{\max}$, but it reaches a definite plateau and then it

decreases again steeply. It is just on the plateau that the curve $|\langle J_n^{(M)}|\Delta\hat{U}_M|J_{n^*}^{(M)}\rangle|$ vs n intersects with the instanton peak curve, which means that tunneling using the transition to the state $n = n^*$ overwhelms the instanton tunneling and so the intersection determines $n_{\rm c}$. As M increases, the height of plateau decreases rapidly and reaches finally to a limit, which causes the instanton region $n_{\rm c} < n < n_{\rm max}$ to grow from a null region to a finite region with the width proportional to τ. Below $n_{\rm c}$, the transition matrix element controls tunneling and so the tunneling probability follows the plateau structure, which explains the characteristic plateau of the tunneling amplitude seen in Fig. 4.6.

The origin of the transition to a plateau-like characteristics of the tunneling rate from the instanton tunneling rate reported in preceding works can therefore be attributed to the formation of the plateau of the transition matrix element and a drastic decrease of plateau height in higher-order renormalization. The I-NI transition in the standard map in Fig. 4.5(b) follows the same scenario as we will discuss in the next chapter 5.

We note that if one shifts each curve in Fig. 4.5 horizontally such that the maximal quantum number $n_{\rm max}$ for each curve coincides with each other, they all show very similar characteristics, and are insensitive to the effective Planck constant $\hbar$. Such a feature can hardly be explained by classical objects *e.g.,* nonlinear classical resonances, which will be discussed in detail in our forthcoming papers [Hanada et al.] and will be discussed in the next chapter 5.

Finally, we elucidate the classical dynamical significance of the plateau region which is characteristic after the I-NI transition. The above analyses tell us that the states composed of the self-component $\ell = n$ and the ones forming the broad peak around $\ell = n^*$ play as the principal component. We define here the principal component contributing to tunneling (PCT) and observe the phase space Husimi-plot to investigate the classical interpretation for the I-NI transition. The PCT is defined as the projection of $|\Psi_n\rangle$ onto the principally contributing subspace constructed as follows. Let $|J_\ell^{(M)}\rangle$ be eigenfunctions rearranged in descending order of the magnitude ${\rm Con}_{\ell,n}$ in the contribution spectrum, and consider the K-dimensional subspace spanned by $|J_\ell^{(M)}\rangle$ $(1 \le \ell \le K)$. Let $K_{\rm min}$ be the minimum number of K which makes the relative distance between the vector $|\Psi_n^{(M)}\rangle$ and its projection onto the above introduced subspace less than a small enough threshold value r_{th} $(\ll 1)$, namely, the minimal $K = K_{\rm min}$ such that

$$\left\langle\!\!\left\langle \frac{|\langle q|\Psi_n^{(M)}\rangle - \sum_{\ell=0}^{K}\langle q|J_\ell^{(M)}\rangle\langle J_\ell^{(M)}|\Psi_n^{(M)}\rangle|}{|\langle q|\Psi_n^{(M)}\rangle|} \right\rangle\!\!\right\rangle < r_{th} \tag{4.12}$$

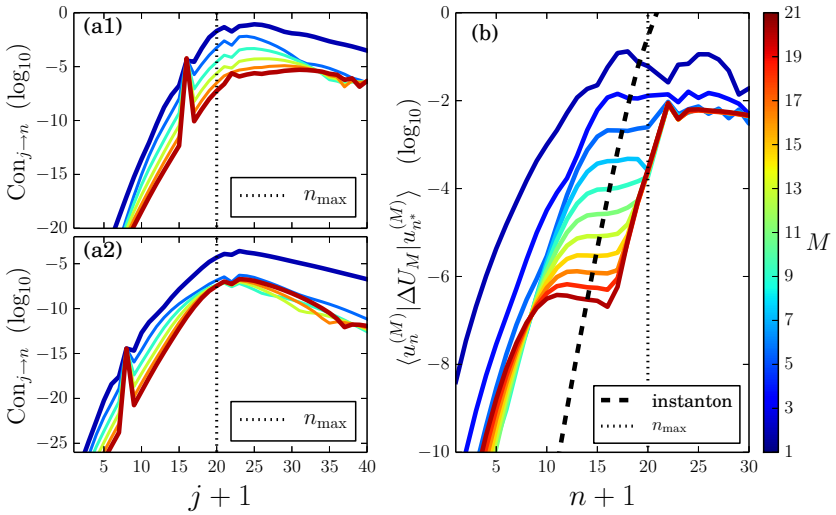

Figure 4.7: Typical contribution spectra $\mathrm{Con}_\ell^{(M)}$ of (a1) before and (a2) after the I-NI transition. Panels (a1) and (a2) respectively correspond to $n = 15$ and $n = 7$ of the Hénon map with $\sqrt{\tau} = 0.1$ and $\hbar = \hbar/2$ (see Fig. 4.6(b1)). The renormalization order grows as $M = 1, 5, 9, 14, 17, 21$. (b) The major transition matrix element $|\langle J_n^{(M)}|\Delta\hat{U}_M|J_{n^*}^{(M)}\rangle$ vs. n for the same Hénon map , where $n^* = 21 = n_{\max} + 2$. M is increased from 1 to 21. The black dotted curve denotes the instanton peak amplitude $\langle\langle|\langle q|J_n^{(M)}\rangle|\rangle\rangle$ of the n-th state. The vertical axis is drawn in the $\log_{10}$ scale.

Then the space spanned by $|J_\ell^{(M)}\rangle$ $(1 \le \ell < K_{\min})$ constitutes the principally contributing subspace to tunneling. We take $r_{th} = 0.2$, for example. We have to emphasize that M must be taken sufficiently large ($M \ge 13$ in practice) in order that the PCT is significant.

The Husimi plots of the PCT before and after the I-NI transition are depicted in Fig. 4.8. The shadowed region indicates the region with the highest probability level. In the instanton regime the PCT coincides almost with the eigenfunction $|J_n^{(M)}\rangle$ of the unperturbed integrable Hamiltonian, and the Husimi plot of PCT in Fig. 4.8(a) indeed traces the classical invariant circle shown as the shadowed region, and the tunneling component is represented by the monotonously decaying contours encircling the shaded quantized invariant circle. In particular, when observed in the q-coordinate, the tunneling tail is the line $p = 0$ passing across the saddle S, which is nothing more than the instanton.

On the other hand, Fig. 4.8(b) indicates that a drastic change occurs in PCT when the transition to NI happens: the main component, characterized by almost the same probability levels, runs along the stable manifold W^s, attracted and repelled by the saddle S, finally runs away toward $q = -\infty$ along the unstable

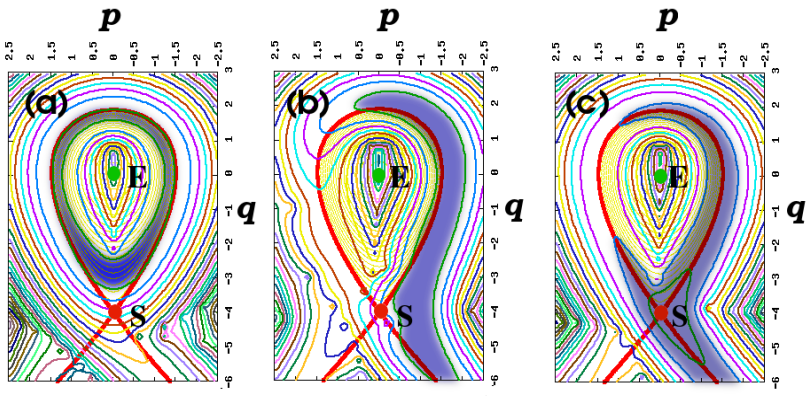

Figure 4.8: Husimi-representation of the PTC for the eigen-function of the Hénon map with $\sqrt{\tau} = 0.1$ and $\hbar = \hbar_0/2$ (see Fig. 4.6(b1)). (a) Before ($n = 15$), and (b) after ($n = 13$) the I-NI transition, and (c) is the eigenstate at the edge of plateau ($n = 7$). Panels (a) and (c) correspond to Fig. 4.7(a1) and (a2), respectively. Contours are plotted in log scale, and the shaded region indicates the highest levels. The red curve is the W^s-W^u complex of the saddle S (red circle), and the green dot E denote the stable fixed point. The Husimi level of (a) coincide entirely with the eigenfunction of $|J_{15}^{(m)}\rangle$ of $\hat{H}_{\rm eff}^{(M)}$, which has its major body winds around W^s, passes nearly to S and is blown to $-\infty$ following the W^u. The maxim level of contour is $10^{0.5}$ in (a), suddenly drops to $10^{-4.5}$ in (b) after the I-NI transition.

manifold W^u, which manifests that the PCT contributing to the tunneling tail represents classical flows just outside of the W^s-W^u complex. The PCTs for all the eigenstates forming the plateau take almost similar patterns but they approach more closely to the W^s-W^u complex, as the quantum number shifts to the edge of the plateau. Figure 4.8(c) shows that just at the eigenstate on the edge of the plateau its PCT coincides with the W^s-W^u complex. As is seen in Fig. 4.5, the tunneling amplitude decreases rapidly when n is less than the plateau edge quantum number. All the above features are common in the Hénon and standard maps, which are more further discussed in the next section 5.

In the present section we have developed a perturbation theory for nearly integrable quantum maps. This is based upon an integrable Hamiltonian which is constructed by maximally renormalizing the integrable part of the map. This was successfully applied to investigate the I-NI transition commonly observed in nearly integrable quantum maps such as the Hénon and standard maps. A remarkable quenching of the highly renormalized transition matrix elements explains the origin of the abrupt change of tunneling characteristics at the I-NI transition. The PCT analysis reveals that the tunneling mechanism in the plateau region after the I-NI transition is due to the classical flow outside of the W^s-W^u complex is responsible for the tunneling process after the transition and the flow coincides with the W^s-W^u complex at the edge of the plateau. This

suggests the crucial role of classical dynamics related to the W^s-W^u complex, and elucidating the relation to the complex stable-unstable manifolds mechanism based on the complex-domain semiclassics is strongly desired.

Chapter 5

Origin of the enhancement of tunneling probability in the nearly integrable system

In this chapter, the enhancement of tunneling probability in the nearly integrable system is closely examined, focusing on tunneling splittings plotted as a function of the inverse of the Planck's constant. On the basis of the analysis using the absorber which efficiently suppresses the coupling creating spikes in the plot, we found that the splitting curve should be viewed as the staircase-shaped skeleton accompanied by spikes. We further introduce renormalized integrable Hamiltonians, and explore the origin of such a staircase structure by investigating the nature of eigenfunctions closely. It is found that the origin of the staircase structure could trace back to the anomalous structure in tunneling tail which manifests itself in the representation using renormalized action bases. This also explains the reason why the staircase does not appear in the completely integrable system.

The organization of the chapter is as follows: In section 5.1, we introduce the system studied in this chapter, and present aspects of the enhancement of the tunneling probability by observing the quantum number and $1/h$ dependence of the tunneling probability in our model. In section 5.2, introducing an absorbing operator, which projects out a given set of integrable states, we examine which states are responsible for creating spikes typically observed in the splitting curve and whether or not the staircase structure of the splitting curve appears as a result of local

quantum resonances in the energy space. In section 5.3, we investigate the nature of eigenstates to clarify the mechanism of the enhancement by focusing on the local probability amplitude of eigenfunctions and the contribution spectrum introduced in [Shudo et al. 2014]. In section 5.4, on the basis of analyses made in section 5.3 we claim that an essential difference of the splitting curve exists between integrable and nonintegrable systems.

5.1 Enhancement of tunneling probability

We consider a quantum system described by the evolution operator in a symmetrized form:

$$\hat{U} = e^{-\frac{i}{\hbar}V(\hat{q})\tau/2} e^{-\frac{i}{\hbar}T(\hat{p})\tau} e^{-\frac{i}{\hbar}V(\hat{q})\tau/2}. \tag{5.1}$$

The corresponding classical dynamics is given as the symplectic map

$$f := f_V(\frac{\tau}{2}) \circ f_T(\tau) \circ f_V(\frac{\tau}{2}) \tag{5.2}$$

where $f_V(\tau) : (q,p) \mapsto (q, p + \tau V'(q))$ and $f_T(\tau) : (q,p) \mapsto (q + \tau T'(p), p)$ are trivial symplectic maps (see Appendix B). Here the prime stands for the derivative of the function. The classical map f corresponds to discretization of the continuous Hamiltonian flow for $H(q,p) = T(p) + V(q)$ up to the second order of the discrete time step τ. Thus, the map f has the integrable (continuous) limit $\tau \to 0$, and much the same is true on the quantum map (5.1). Hereafter we take the potential function as $T(p) = p^2/2$ and $V(q) = (k/4\pi^2)\cos(2\pi q)$ where k is the strength of the perturbation. After rescaling as $p \mapsto p/\tau$ and $k\tau^2 = \varepsilon$, the classical map f turns out to be the symmetrized standard map [Chirikov 1969; 1979], and the time evolution by the unitary operator $\hat{U}$ can be interpreted as a single period evolution of a δ-functional periodically forcing Hamiltonian with a period τ.

In the continuous limit $\tau \to 0$, the closed area surrounded by the separatrix is given by $S = \sqrt{k}(2/\pi)^2$. In the following argument, we focus especially on the nearly integrable regime and a proper integrable limit will play an important role as a reference. In most of situations, nonlinearity is controlled by changing the parameter τ, keeping the parameter fixed as $k = k_0 \equiv 0.7458\cdots$.

Figure 5.1 displays classical phase space for typical nearly integrable parameter regions. In the case of

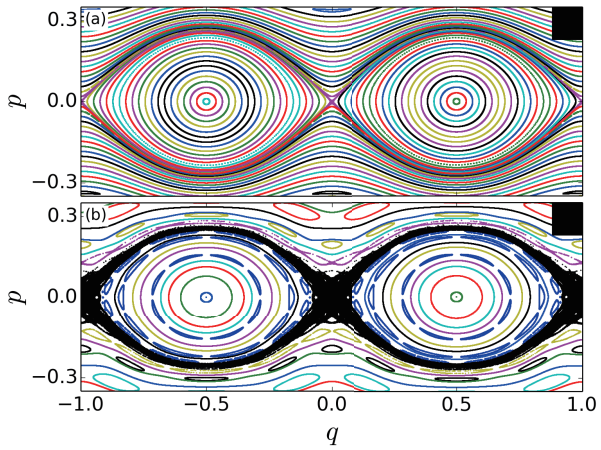

Figure 5.1: Classical phase space for the symmetrized standard map (5.2) with (a) $\tau = 2/3$ and (b) $\tau = 1$. There are no visible resonance chains for $\tau = 2/3$ in the inner tours region while chaotic regions around the unstable fixed point at $(q, p) = (0, 0)$ and some resonance chains ($1 : 8$, $1 : 10$, $1 : 12$,$\cdots$) become visible for $\tau = 1$. They are shown in dark blue. The black box put in the upper right corner indicates the size of the effective Planck's constant for $h = 1/70$.

$\tau = 2/3$, classical phase space is predominantly covered by regular regions and nonlinear resonance chains are not visible in this scale. For $\tau = 1$, small chaotic regions emerge around an unstable fixed point at $(q, p) = (0, 0)$, and Poincaré-Birkhoff chains induced by nonlinear resonances become visible. Relatively large nonlinear resonances in the inner torus region, which represents librational motions in the pendulum Hamiltonian H, are $1 : 8$, $1 : 10$, and $1 : 12$ ones, which are marked in dark blue in Fig. 5.1(b). Below we mainly develop our discussion in the case $\tau = 1$, but essentially the same argument follows for other τ cases.

We numerically solve the eigenvalue problem for the unitary operator $\hat{U}$

$$\hat{U}|\Psi_n\rangle = u_n|\Psi_n\rangle, \tag{5.3}$$

under the periodic boundary condition on the region $(q, p) \in (-1, 1] \times (-1/2\tau, 1/2\tau]$. Let N be the dimension of the Hilbert space space, then to achieve the periodic boundary condition the relation $1/2\tau \times 2/\hbar = 2\pi N$ should hold, which yields the relation $h = 2/N\tau$.

Here u_n is expressed as $u_n = e^{-iE_n\tau/\hbar}$ where E_n $(n = 0, 1, 2, \cdots)$ are quasi-energies, and $|\Psi_n\rangle$ denote the corresponding quasi-eigenstates. Hereafter we focus on the doublet states in bounded states supported

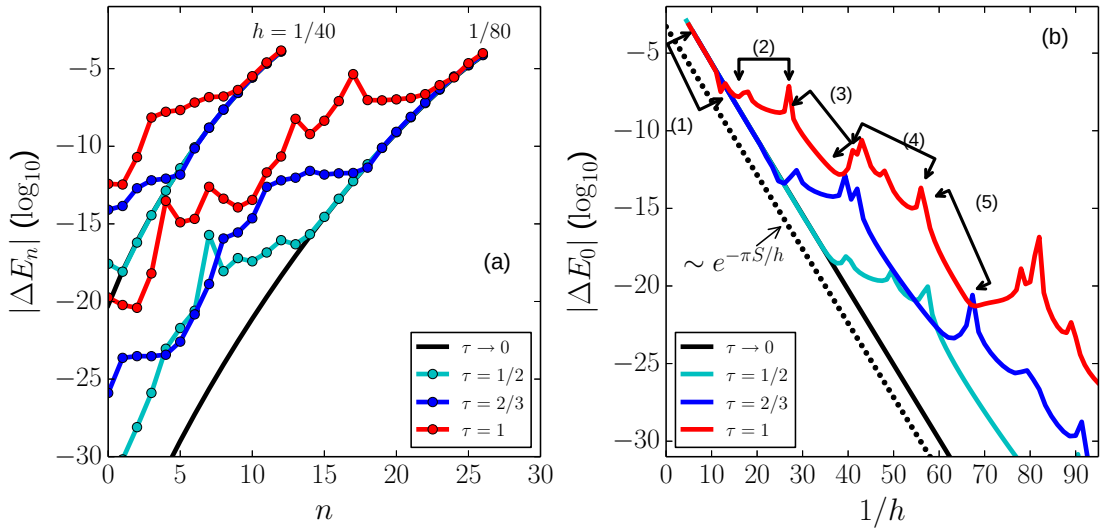

Figure 5.2: (a) The tunneling splitting ΔE_n is plotted as a function of the quantum number n, where n is labeled not for an individual state but for a doublet (see the text). The value of h for each curve is put in the figure. The black curves represent the splitting $\Delta E_n^{(1)}$ in the limit $(\tau \to 0)$ (b) The tunneling splitting ΔE_0 for the lowest doublet $|\Psi_0^{\pm}\rangle$ is shown as a function of $1/h$. The black solid and dotted curves correspond to the splitting $\Delta E_0^{(1)}$ in the limit $(\tau \to 0)$ and the semiclassical prediction (3.13), respectively. In (b), we put the labels (1), (2), $\cdots$, (5) on each characteristic interval: (1) first exponential decay (instanton), (2) first plateau, (3) second steeply decay, (4) second plateau, and (5) third steeply decay regime, respectively.

by the inner torus region, each of which is centered at $(q, p) = (\pm 1/2, 0)$ and energy splittings between them.

Quasi-eigenstates $|\Psi_n\rangle$ have a symmetry with respect to the mirror transformation $\hat{\Pi}_q : q \mapsto -q$, and we hereafter denote the doublet states associated with this symmetry by $|\Psi_n^{\pm}\rangle$ and the corresponding quasi-energies by $E_n^{\pm}$, which form quasi degeneracy. We therefore assign the quantum number n not to an individual quasi-eigenstate but to each doublet[1]. The states $|\Psi_n^{+}\rangle$ and $|\Psi_n^{-}\rangle$ respectively represent symmetric and anti-symmetric states. Note that we have additional symmetry with respect to the translation $\hat{T}_1 : q \mapsto q+1$, originating from the periodic boundary condition in the q-direction. This symmetry does not induce quasi degeneracy in energy, but the states belonging to a different translational symmetry class do not interact with each other even if they have the same mirror symmetry.

In the continuous limit $\tau \to 0$, the eigenvalue equation for the Hamiltonian $H(q, p) = p^2/2 + V(q)$ is

[1] In the vicinity of the energy corresponding to the unstable fixed point at $(q, p) = (0, 0)$, the states $|\Psi_n^{\pm}\rangle$ do not form tunneling doublets, so this numbering rule does not work, but this ambiguity will not cause any serious confusion in the present description.

expressed as

$$\hat{H}(\hat{q},\hat{p})|J_n^{\pm}\rangle = E_n^{\pm,(1)}|J_n^{\pm}\rangle, \tag{5.4}$$

where eigenstates $|J_n^{\pm}\rangle$ are in the same symmetry class as the corresponding $|\Psi_n^{\pm}\rangle$. Here the quantum number n is, as usual, attached in ascending order of eigenvalue $E_n^{\pm,(1)}$, so $|J_n^{\pm}\rangle$ represents the ground state doublet, which we will hereafter focus on.

For the later purpose, we rearrange the quantum number n for the quasi eigenstates $|\Psi_n^{\pm}\rangle$ such that the overlap $|\langle J_n^{\pm}|\Psi_n^{\pm}\rangle|^2$ is maximal. This condition, that is one-to-one correspondence between $|\Psi_n^{\pm}\rangle$ and $|J_n^{\pm}\rangle$ is fulfilled for the values of τ used in the present analysis.

With increase in the value of $1/h$, the tunneling probability between $|\Psi_n^{\pm}\rangle$, which could be measured by the tunneling splitting $\Delta E_n = E_n^+ - E_n^-$, becomes large in several orders of magnitude as compared to those predicted in the continuous limit. The latter is evaluated as $\Delta E_n^{(1)} = E_n^{+,(1)} - E_n^{-,(1)}$. We notice that the overall behavior does not depend on the value of the perturbation strength τ, although the Planck's cell can resolve chaotic regions and nonlinear island chains in the case of $\tau = 1$, whereas this does not the case at all for $\tau = 2/3$. (see Figs. 5.1 and 5.3).

We illustrate such anomalous enhancement of tunneling probability in a nearly integrable regime in two ways. First, as shown in Fig. 5.2(a), the tunneling splitting ΔE_n is plotted as a function of the quantum number n, and in Fig. 5.2(b) the splitting ΔE_0 as a function of $1/h$. The latter is known to be a standard plot often used in the study of RAT [Brodier et al. 2002, Schlagheck et al. 2011] as discussed in section 3.2.

In Fig. 5.2(a) we notice that, in the relatively large n regime, ΔE_n can be fitted by the lines predicted by the formula (3.13), implying that they have completely integrable nature in essence. On the other hand, as n goes down from exited states to the ground state, with a fixed $\hbar$, the law described by the formula (3.13) is violated at certain critical quantum numbers n_c, each of which depends on the value of h [Brodier et al. 2001; 2002, Shudo et al. 2014].

At such a quantum number n_c, the curve for ΔE_n changes its slope and forms the plateau. After a certain plateau interval, as typically seen in $\tau = 1$ and $\tau = 2/3$ for $h = 1/80$, the slope again becomes large, and then forms the second plateau. The emergence of plateaus means the enhancement of the tunneling probability as compared to the integrable (instanton) prediction. It is particularly non-trivial and even paradoxical because this enhancement is relatively stronger in the lower doublets than higher excited ones.

Note also that the critical quantum number n_c becomes large with increase in the value of τ. This sudden departure from integrable tunneling has been pointed out in the study of RAT [Brodier et al. 2001; 2002], and it is called the *instanton-noninstanton* (I-NI) transition [Shudo and Ikeda 2012, Shudo et al. 2014] (see also section 4.2), in which the mechanism behind it has been investigated in a different perspective.

The I-NI transition is similarly observed in the ΔE_n vs $1/h$ plot. As shown in Fig. 5.2(b), the energy splitting ΔE_0 for the lowest doublet $|\Psi_0^{\pm}\rangle$ exhibits a similar behavior. For relatively large values of h, ΔE_0 follows the instanton prediction Eq. (3.13), but deviates from it at certain values of h, each of which depends on the value of τ. The staircase-like structure formed with plateau and steeply decaying intervals again characterize the overall structure. For the purpose of illustration, we call each region in the staircase, (1) first exponential decay (instanton) (2) first plateau, (3) second steeply decay, (4) second plateau, and (5) third steeply decay regime, respectively (see Fig. 5.2(b)).

What is prominent in the latter plot than in the former plot is the appearance of spikes. This is because in the former plot Fig. 5.2(a), we could evaluate tunneling splitting only at integer values (quantum numbers), so may miss spikes even if they exist, whereas we can scan ΔE_0 at more numerous values of $1/h$.

The origin of spikes is a central issue in theory of RAT [Eltschka and Schlagheck 2005, Löck et al. 2010, Schlagheck et al. 2011], in which the effect of nonlinear resonance is incorporated by first constructing local integrable pendulum Hamiltonian classically and then applying quantum perturbation theory. Plotting the energy levels as a function of some parameter, k for example, one can recognize that the mechanism of the enhancement due to RAT is similar to CAT: as the parameter is varied, the states forming the reference doublet, $|\Psi_0^{\pm}\rangle$ in the present case, come close to a third state. They interact with each other, and in the interaction regime the splitting between the reference doublet becomes large, resulting in a spike [Schlagheck et al. 2011]. Note, however, that the staircase structure formed with the plateau and steeply decaying regime has never been found at least in the completely integrable systems studied so far.

5.1.1 Resonance spikes and the third states

Each spike observed in Fig. 5.2(b) appears as a result of energy resonance between the doublet $|\Psi_0^{\pm}\rangle$ and a certain third state. The spikes mostly appear in the plateau regime, but sometimes they are situated in the steeply decaying regime. In Fig. 5.3, we first demonstrate which type of third states are actually involved

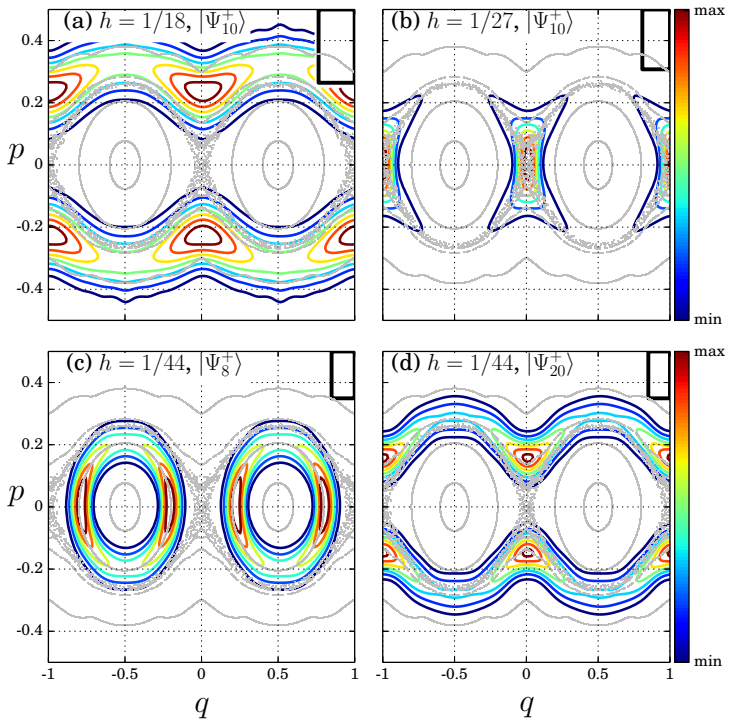

Figure 5.3: Husimi representation of the third states for $\tau = 1$, which resonantly interact with the reference doublet in the first plateau regime: (a) $1/h = 18$ (at the middle of the first plateau), (b) $h = 1/27$ (at the end of first plateau), (c) and (d) $h = 1/44$ (at the second plate regime). In (a), (c) and (d) we only show $|\Psi_n^+\rangle$ states out of each tunneling doublet. In (b), the state $|\Psi_n^+\rangle$ is not the one forming a doublet as mentioned in footnote 1 in this chapter. Upper left box represents the size of effective Planck's cell.

in the creation of spikes. In the original framework of the RAT theory, the predicted spikes are associated with the states supported by nonlinear resonances in the inner torus region, encircling central elliptic fixed points, $(q, p) = (\pm 1/2, 0)$ in the present case. However, two of spikes in the first plateau appear as a result of resonance with the states associated with an outer transversal torus and the spike located at the end of the first plateau $h = 1/27$ is associated with the state localized on the unstable fixed points $(q, p) = (0, 0)$ and $(-1, 0)$ (see Fig. 5.3(b)). This is not surprising since the present eigenstates are Floquet states, so the eigenphase $\tau E_n/\hbar$ of Eq. (5.3) can satisfy the resonance conditions $E_n - E_\ell = mh/\tau$ $(n, \ell, m \in \mathbb{Z})$. Therefore the quasi-energies of our reference doublet can resonate with a state associated with an outer transversal tours. Such situations are out of the scope of the theory of RAT, but as will closely be discussed in section 5.3, the outer torus states play a crucial role in the formation mechanism of the staircase structure.

Figures 5.4(a) and (b) demonstrate the splitting ΔE_0 (in the back panel), together with the behavior of

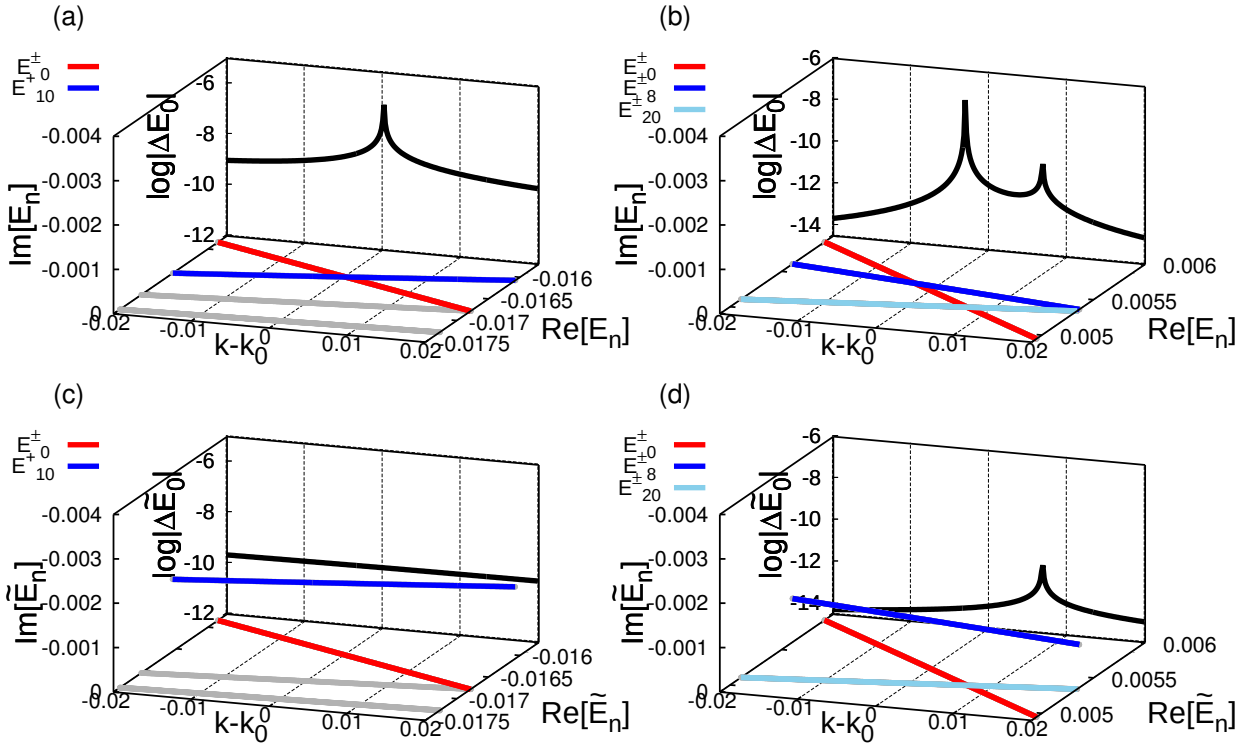

Figure 5.4: Energy splittings ΔE_0 (black lines in the back panel) and the reference doublet (red lines in the floor panel) and the related third state energies (blue and light blue lines in the floor panel) as a function of the parameter k. For each curve, the corresponding energy level is put in the figures. Gray lines indicate energies of the states irrelevant to creating spikes in the upper panels, no absorber was applied for (a) $1/h = 27$ and (b) $1/h = 44$. In the lower panels, the strength of the absorber is set as $\Gamma = 1$ for (c) $1/h = 27$ and (d) $1/h = 44$. The index set L is given as (a) $L = \{10\}$ and (b) $L = \{8\}$.

doublet and the third state energies (in the floor panel) as a function of the parameter k. When a spike appears in the ΔE_0 vs $1/h$ plot, there always exist spikes in the plot of ΔE_0 vs k nearby. However, even if a spike appears in the ΔE_0 vs $1/h$ plot, it does not necessarily mean that one exactly hits a spike in the plot of ΔE_0 vs k. These figures reveal that the third state for $1/h = 27$ (at the end of the first plateau) is the 10-th excited state $|\Psi_{10}^{+}\rangle$ and this state is, as shown in Fig. 5.3 (b), localized on the unstable fixed point $(q, p) = (0, 0)$. On the other hand, $1/h = 44$ (in the middle of the second plateau), there appear two spikes in the range under observation, one is the doublet composed of the 8-th excited states $|\Psi_{8}^{\pm}\rangle$ whose symmetric state is shown in Fig. 5.3 (c), and the other is also given as a doublet of excited states, $|\Psi_{20}^{\pm}\rangle$ whose symmetric state is shown in Fig. 5.3(d). As demonstrated in Figs. 5.3 (c) and (d), both doublets $|\Psi_{8}^{\pm}\rangle$ and $|\Psi_{20}^{\pm}\rangle$ are supported by elliptic inner and transversal outer KAM curves, respectively.

5.2 Staircase structure with resonance spikes

In the previous section, we discussed how the spikes caused as a result of the energy level resonance appear in the splitting curve what third state is involved in each resonance. In this section, we introduce an absorbing operator and show that the enhancement of the tunneling probability has an entirely different origin from the energy level resonance.

5.2.1 Absorbing operator

To discuss the relation between the resonance spikes and the enhancement in the splitting curve, we consider the following absorbing operator

$$\hat{P} = \mathbb{1} - \frac{\Gamma}{2} \sum_{\ell \in L} |J_\ell\rangle\langle J_\ell|. \tag{5.5}$$

introduced by [Kaplan 1999] (see also Ref. [Lippolis et al. 2012]). Here $\Gamma \leq 2$ represents the absorbing strength, and $\mathbb{1}$ the identity operator. The summation runs over a given index set L, which we choose appropriately depending on which states we want to suppress[2]. Below we consider the right eigenvalue problem for the absorbed (non-unitary) evolution operator

$$\hat{U}^\circ |\Psi_n^\circ\rangle = u_n^\circ |\Psi_n^\circ\rangle, \tag{5.6}$$

where

$$\hat{U}^\circ = \hat{P}\hat{U}, \tag{5.7}$$

The following argument holds even if one considers the left eigenvalue problem.

First we will discuss what we can expect in perturbation theory with respect to the absorbing strength Γ. It is easy to show that a standard perturbative calculation up to the second order provides

$$u_n^\circ \simeq u_n \cdot z_n, \tag{5.8}$$

[2]In Eq. (A.3) we drop suffices $\pm$ since the definition of $\hat{P}$ makes sense irrespective of the symmetry.

where

$$z_n = 1 - \frac{\Gamma}{2}\sum_{\ell\in L}|a_{\ell,n}|^2 + \frac{\Gamma^2}{4}\sum_{\ell\in L}\sum_{m\neq n}\frac{|a^*_{\ell,n}a_{\ell,m}|^2}{u_n - u_m}u_m, \tag{5.9}$$

and

$$a_{\ell,n} = \langle J_\ell|\Psi_n\rangle. \tag{5.10}$$

The right (absorbed) eigenstate is also given as

$$\begin{aligned}|\Psi^\circ_n\rangle &= |\Psi_n\rangle - \frac{\Gamma}{2}\sum_{\ell\in L}\sum_{m\neq n}\langle\Psi_n|\frac{|J_\ell\rangle\langle J_\ell|}{u_m - u_n}\hat{U}|\Psi_m\rangle \\ &= |\Psi_n\rangle - \frac{\Gamma}{2}\sum_{\ell\in L}\sum_{m\neq n}\frac{a^*_{\ell,n}a_{\ell,m}}{u_m - u_n}u_m|\Psi_m\rangle.\end{aligned} \tag{5.11}$$

Insert the completeness condition with absorber $\sum_k |J_k\rangle\langle J_k| = \mathbb{1}$, into Eq. (5.11), thus the perturbation result becomes

$$\begin{aligned}|\Psi^\circ_n\rangle &= |\Psi_n\rangle - \frac{\Gamma}{2}\sum_{k}\sum_{m\neq n}B_{m,n}a_{k,m}|J_k\rangle \\ &= |\Psi_n\rangle - \sum_k C_{k,n}|J_k\rangle\end{aligned} \tag{5.12}$$

where

$$C_{k,n} = \frac{\Gamma}{2}\sum_{m\neq n}B_{m,n}a_{k,n}, \qquad B_{m,n} = \sum_{\ell\in L}\frac{a^*_{\ell,m}a_{\ell,n}}{u_n - u_m}u_m. \tag{5.13}$$

For $0 < \Gamma \leq 2$, $|z_n|$, the absorbed quasi-energies are no more real because the second-order term in the perturbation expansion Eq. (5.8) becomes complex while the first-order term is real-valued. The absorbed eigenvalues $|u^\circ_n|$ are inside the unit circle and u°_n is shifted as

$$\arg u^\circ_n = \arg u_n + \arg z_n. \tag{5.14}$$

The absorbed quasi-energy could be expressed as

$$u^\circ_n = e^{-i\frac{\tau}{\hbar}\tilde{E}_n} = e^{-i\frac{\tau}{\hbar}(\tilde{E}^{\mathsf{re}}_n - i\tilde{E}^{\mathsf{im}}_n)} = e^{i\tilde{\varphi}_n}e^{-\frac{\gamma_n}{2}}, \tag{5.15}$$

where γ_n characterizes the decay rate which is given by leading order of perturbation terms

$$\gamma_n \approx \Gamma \sum_{\ell \in L} |\langle J_\ell | \Psi_n \rangle|^2. \tag{5.16}$$

Note that when the eigenstates $|\Psi_n\rangle$ does not overlap with the absorber the eigenstates $|\Psi_n^\circ\rangle$ are not affected by the absorber.

This absorbing method could be regarded as an inverse procedure of what is done in typical perturbation theory such as RAT theory, in which one starts with some unperturbed states $|J_n\rangle$ and build up desired eigenstates $|\Psi_n\rangle$ by adding perturbation terms. The present absorbing method is, in a sense, to subtract perturbed terms $|J_n\rangle$ from the final state $|\Psi_n\rangle$. Therefore, applying the absorber in this way would be a test to check whether the final state $|\Psi_n\rangle$ could be obtained as a result perturbation in terms of unperturbed states $|J_n\rangle$, and, if so, which unperturbed states are involved in the perturbation procedure. The present absorbing method is equivalent to the one used in the open quantum systems, *e.g.*, [Bäcker et al. 2010, Keating et al. 2008, Löck et al. 2010, Mertig 2013], in which the absorbers are adopted as the Heaviside step function $\langle x|J\rangle = H(x)$ or the Dirac delta function $\langle x|J\rangle = \delta(x)$.

The decay rate γ_n defined by the absorbing potential has been studied intensively in the Dresden group [Bäcker et al. 2010, Löck 2009, Löck et al. 2010, Mertig 2013] and they adopt the decay rate γ_n as a definition of tunneling rate. From the relation (5.16) the decay rate γ_n depends strongly on the position and shape of the absorber, therefore we distinguish the decay rate from the tunneling splitting. The relation between the splitting ΔE_n and the decay rate γ_n is closely discussed in Appendix A, in which is uncontrollable propagation driven by an improper absorbing operator is indicated.

Demonstration of the absorbing method

We here demonstrate the efficiency of the absorbing method by taking the integrable base $|J_{10}^+\rangle$ as the absorber. Figure 5.5 shows the eigenvalues of the absorbing quantum map $\hat{U}^\circ$. In the unitary case ($\Gamma = 0$), all the eigenvalues sit on the unit circle. On the other hand, a certain eigenstate $|\Psi_{10}^+\rangle$ (red dot) enters inside the unit circle for $\Gamma > 0$ as expected from the perturbation result (5.8). This absorbed state is $|\Psi_{10}^+\rangle$. The absorber mainly affects only a single state in the present nearly integrable regime. Another eigenvalues keep almost the same positions and it deviations from the unit circle cannot be identified in this scale.

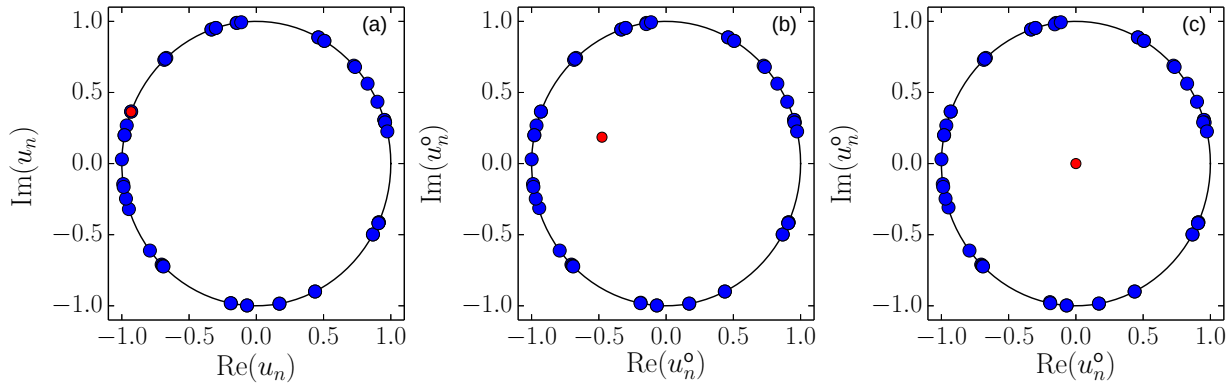

Figure 5.5: (a) The plot of the eigenvalues of the unitary quantum map $\hat{U}$ with $1/h = 27$ in the complex energy plane. The unit circle is drawn as the solid curve. The eigenvalues of the absorbed quantum map $\hat{U}^\circ$ for the absorbing strength (b) $\Gamma = 1$ and (c) $\Gamma = 2$. The red dot located inside the unit circle denotes the eigenvalue of the state $|\Psi_{10}^+\rangle$ which localizes on the chaotic sea (see Fig. 5.3(b)). Here we use the integrable base $|J_{10}^+\rangle$ as the absorber.

By applying the absorber, the coupling between the absorbed and the rest of eigenstates is suppressed as shown in Fig. 5.4(a) and (b). This efficiency of the absorbing method is demonstrated in Figs. 5.4(c) and (d). For absorbed quasi-energies $\tilde{E}_n^\pm$, the tunnel splitting $\Delta\tilde{E}_n$ is defined as $\Delta\tilde{E}_n = \tilde{E}_n^- - \tilde{E}_n^+$, however we note that the quasi-energy $\tilde{E}_n^\pm$ has an imaginary part when $\Gamma > 0$. Each corresponds to the case where the absorber with $\Gamma = 1$ is applied to the case shown in Fig. 5.4(c) and (d), respectively. Here the index set L is chosen as $L = \{10\}$ in the case of $1/h = 27$, and $L = \{8\}$ whose member corresponds to the doublet of the symmetric and anti-symmetric state $|J_8^\pm\rangle$ for $1/h = 44$. Here $\{\ell\}$ represents $|J_\ell^\pm\rangle$, and the member $|J_\ell^\pm\rangle$ in the index set L is chosen in such a way that it maximally overlaps with the third state that is interacting the reference doublet $|\Psi_0^\pm\rangle$ and responsible for creating the spike.

As clearly shown, energies of the associated third states gain certain amount of the imaginary part and pushed out to the complex plane, resulting in vanishing the spikes. The effect to the other states is almost negligible. However, as seen in Fig. 5.4(d), the right-hand peak with shorter height still remains since we have not include the states $|J_{20}^\pm\rangle$ in the absorber. As mentioned in the end of the previous subsection 5.1.1, there are two sets of doublets which are involved in avoided crossings in question.

5.2.2 Staircase structure

In the previous subsection, we have selected out absorbing states by plotting energy levels around each avoided crossing and then judging by hand which states should be included in the set L, that is, it was necessary to refer to the figures like Fig. 5.4. We now introduce a systematic procedure to choose the absorbing states necessary to suppress the observed spikes.

The most natural criterion to achieve this would be to check the energy difference from the reference doublet: $d(E_n^{\pm}) = |E_0^{\pm} - E_n^{\pm}|$ $(n = 1, 2, \cdots)$, because the spikes appear when the reference doublet and a certain third state are energetically close to each other and form avoided crossings. We rearrange the states $|\Psi_n^{\pm}\rangle$ in ascending order of $d(E_n^{\pm})$, and the corresponding integrable base $|J_n^{\pm}\rangle$ as well. The one-to-one correspondence between $|\Psi_n^{\pm}\rangle$ and $|J_n^{\pm}\rangle$ is again ensured since the condition $|\langle J_n^{\pm}|\Psi_n^{\pm}\rangle| \approx 1$ is now satisfied for $\tau = 1$. Then the set of absorbing states containing the first s doublets in the sense of the energy distance reads

$$L_s = \{1, 2, \cdots, s\}, \tag{5.17}$$

where we drop from the list of L_s the states not belonging to the same parity as $|\Psi_0^{\pm}\rangle$. We must recall that the ground state $|\Psi_0^{\pm}\rangle$ has the symmetry with respect to the translation in addition to the mirror transformation.

Note that the set L_s of absorbing states depends on the value of h, so has to be determined for each h. As explained below, the reason why we consider the cases $s > 1$ is that the energetically nearest state L_1 from the reference doublet is not sometimes sufficient for killing the coupling with the reference doublet.

Figure 5.6 plots the splitting of quasi-energy $\tilde{E}_0^{\pm}$ evaluated for the operator $\hat{U}^{\circ}$ as a function of $1/h$. In the $s = 1$ case, we see that some spikes, especially in the first plateau, disappear with increase in Γ. As shown in Fig. 5.4, the absorber pushes the third level into the complex domain, and the coupling with the reference doublet is suppressed.

However, we notice that some spikes still remain in the second plateau regime. This is due to the fact that, as shown in Fig. 5.4(b), some spikes come close to each other in the second plateau and a single absorber is not enough to suppress the interaction with the reference doublet. In the case presented in Fig. 5.4(b), the third state responsible for the left-hand peak is the state supported by an elliptic torus inside the KAM region

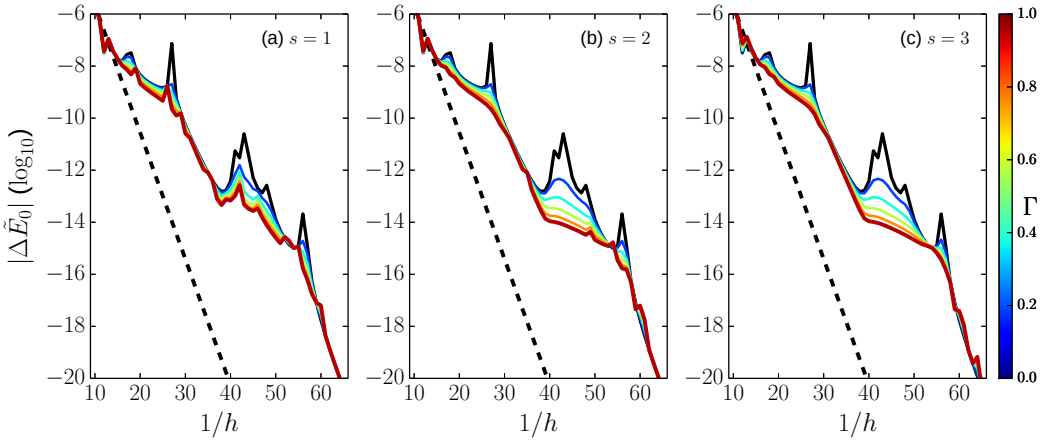

Figure 5.6: Tunneling splittings $\Delta\tilde{E}_0$ for the evolution operator $\hat{U}^\circ$ are plotted as a function of $1/h$. The range of interaction in increased as (a) $s = 1$, (b) $s = 2$, and (c) $s = 3$. Black curves show the unitary case ($\Gamma = 0$) and each colored curve the case with absorber, and the colors distinguish the absorbing strength Γ (see the right-hand color bar). The splitting ΔE_0 in the integrable limit is shown as black dashed lines in each figure.

and the right-hand one is supported by a transversal torus. As we further add the corresponding absorbers in this way, the peaks surviving in the $s = 2$ case gradually disappear, and the curve almost converges at $s = 2$.

It would be worth emphasizing that steeply decaying regions are not affected and robust against the the absorber applied on plateaus. This strongly suggests that the influence of spikes is well localized in each plateau, not like the situation suggested in [Löck et al. 2010]. This observation also supports our hypothesis; the splitting curve should be viewed as a staircase structure accompanied by spikes, not as spikes bringing the staircase.

5.3 Mechanism generating the staircase structure

The main message in the previous section is that the staircase-shaped skeleton is formed in the splitting curves and spikes are superposed on it. In this sense we may say that the origin of the enhancement of the tunneling probability traces back to such a staircase structure. In this section, we study the mechanism creating the staircase structure by introducing the renormalized basis, and show the reason why this only appears in nonintegrable systems.

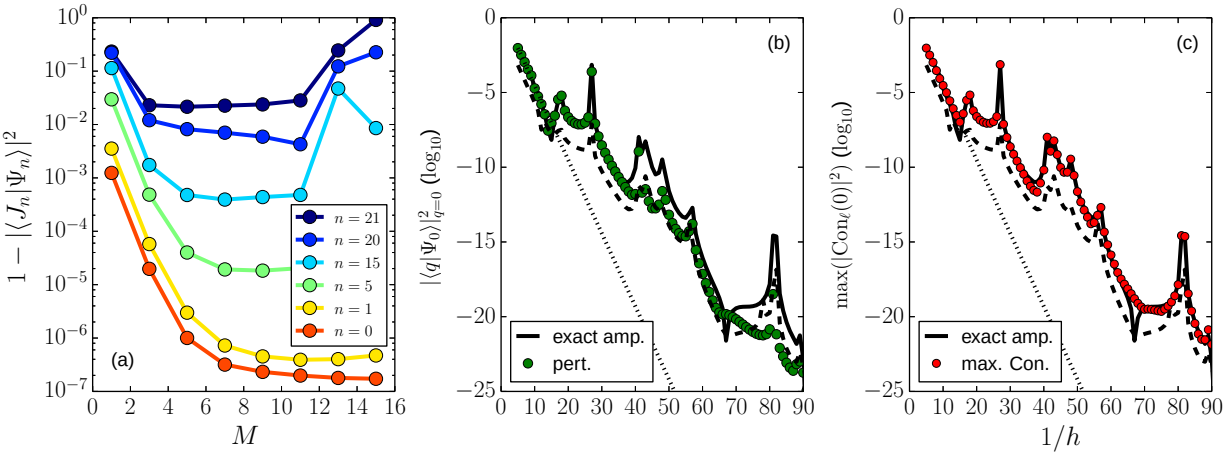

Figure 5.7: (a) Left panel shows the error $1 - |\langle J_n^{(M)}|\Psi_n\rangle|^2$ as a function of the BCH order M in the case of $h = 1/63$. Not only the grand state, $n = 0$, but also excited states up to $n = 21$ are examined. (b1) The amplitude at $q = 0$ of the ground state obtained by the perturbation calculation, and (b2) the amplitude of the maximal mode of the contribution spectrum (see the text). The exact amplitude for the ground state $|\Psi_0\rangle$ at $q = 0$ is shown as blue curves in (b1) and (b2). The solid black dashed and dotted curves show the exact level splitting ΔE_0 and the level splitting $\Delta E_0^{(M)}$ of the integrable basis for reference, respectively.

5.3.1 Instanton-noninstanton transition

As shown in [Shudo et al. 2014], the I-NI transition could be well captured by renormalized perturbation theory. An important finding there was that a remarkable quenching of renormalized transition matrix elements explains the I-NI transition. In particular, without using highly renormalized integrable Hamiltonian as unperturbative bases one could not identify the mechanism behind the transition.

For this reason, we also apply the same perturbation scheme to pursue the origin of the staircase structure. In essence, renormalized perturbation theory makes use of the Baker-Campbell-Hausdorff (BCH) expansion [Scharf 1988, Shudo et al. 2014]:

$$\hat{U} \approx \hat{U}_M \equiv \exp\left[-\frac{i}{\hbar}\tau \hat{H}_{\mathrm{eff}}^{(M)}(\hat{q},\hat{p})\right], \tag{5.18}$$

where

$$\hat{H}_{\mathrm{eff}}^{(M)}(\hat{q},\hat{p}) = \hat{H}_1(\hat{q},\hat{p}) + \sum_{\substack{j=3 \\ (j\in\text{odd int.})}}^{M} \left(\frac{i\tau}{\hbar}\right)^{j-1} \hat{H}_j(\hat{q},\hat{p}). \tag{5.19}$$

Here $\hat{H}_j$ denotes the j-th order term in the BCH series. Explicit forms for the first few terms are found as

$$\hat{H}_1(\hat{q},\hat{p}) = T(\hat{q}) + V(\hat{p}), \tag{5.20a}$$

$$\hat{H}_3(\hat{q},\hat{p}) = \frac{1}{24}\big([T,[T,V]] - [V,[V,T]]\big), \tag{5.20b}$$

$$\vdots$$

where the terms $\hat{H}_j$ for even j are equal to zero thanks to the symmetrized form of $\hat{U}$. The first order BCH Hamiltonian $H_{\text{eff}}^{(1)}$ is identical to the continuous time Hamiltonian and higher order BCH Hamiltonians BCH are expressed as nested commutators. We denote the eigenfunctions of the integrable Hamiltonian $\hat{H}_{\text{eff}}^{(M)}$ by $|J_\ell^{(M)}\rangle$:

$$\hat{H}_{\text{eff}}^{(M)}|J_\ell^{(M)}\rangle = E_\ell^{(M)}|J_\ell^{(M)}\rangle. \tag{5.21}$$

We first check the validity and efficiency of renormalized perturbation bases by examining the error $1 - |\langle J_n^{(M)}|\Psi_n\rangle|^2$ of the approximation. As shown in Fig. 5.7(a), the BCH states becomes better approximation to the corresponding eigenstate $|\Psi_n\rangle$ as the expansion order M increases. Note also that the expansion works for the lower energy eigenstates as compared to the higher excited states. This is, however, not a convergent expansion: the error $1 - |\langle J_n^{(M)}|\Psi_n\rangle|^2$ starts to grow when the expansion order M exceeds a certain optimal order.

Such highly efficient integrable approximation ensures the validity of renormalized perturbation, in which the difference $\Delta\hat{U}_M = \hat{U} - \hat{U}_M$ could be regarded as a perturbation [Shudo et al. 2014]. As also shown in Fig. 5.7(b1), the results of the 1st order perturbation calculation are in an excellent agreement with the exact ones, and even the staircase structure could be reproduced. However we would like to remark that although perturbation theory, not necessarily the present one, works well, this does not tell us anything about the underlying mechanism generating the staircase.

As shown in Fig. 5.7(b1), the splitting ΔE is strongly correlated with the amplitude of the eigenstate at $q = 0$, and characteristic patterns appear around $q = 0$. As seen in Fig. 5.8(a), the eigenstate $|\Psi_0\rangle$ for $\tau = 1$ in the instanton regime is, as expected, well fitted by the one $|J_0^{(M)}\rangle$ in the integrable bases, whereas the integrable approximation does not work any more and further structures appear in other regions. In the first and second plateau, the curve bends in a convex way (see Fig. 5.8(b) and (d)), but in the first steeply decaying

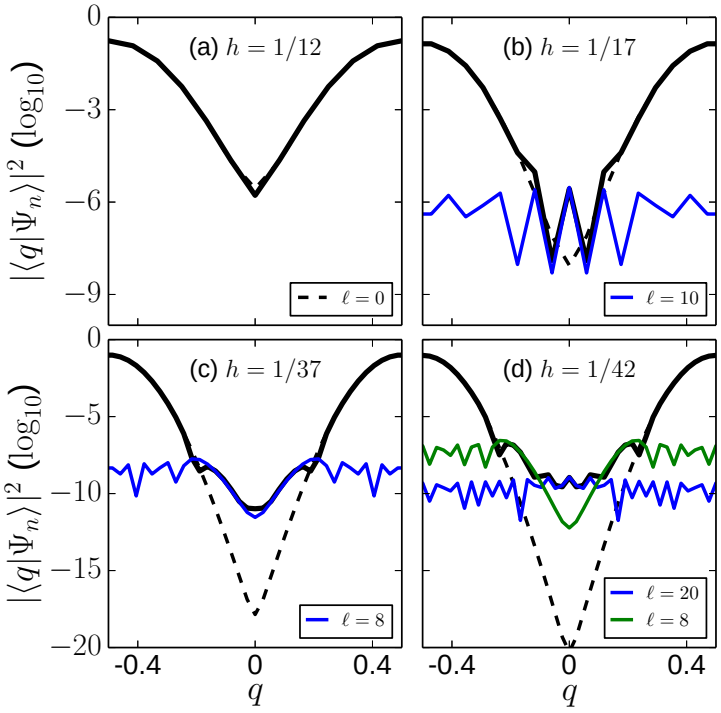

Figure 5.8: The black curve in each figure shows the eigenstate $|\Psi_0\rangle$ for $\tau = 1$ in the (a) instanton, (b) first plateau, (c) second decay and (d) second plateau regime, respectively. The dashed curve displays the integrable eigenstate $\langle q|J_0^{(M)}\rangle$ at the corresponding h value, and colored ones the integrable components $\langle q|J_\ell^{(M)}\rangle\langle J_\ell^{(M)}|\Psi_0\rangle$ at $q = 0$, where the value of ℓ is put in each figure. Note that the structure around $q = 0$ can be well reproduced by the maximal mode(s) of the contribution spectrum (see the text).

region the curve bends in a downward direction at $q = 0$ and takes a concave structure (see Fig. 5.8(c)).

To explore the nature of wavefunctions at $q = 0$, we here introduce a spectrum decomposition at each position q in terms of integrable bases $|J_\ell^{(M)}\rangle$:

$$\langle q|\Psi_0^+\rangle = \sum_{\ell=0}^{N-1} \mathrm{Con}_\ell^{(M)}(q) \tag{5.22}$$

where

$$\mathrm{Con}_\ell^{(M)}(q) = \langle q|J_\ell^{(M)}\rangle\langle J_\ell^{(M)}|\Psi_0^+\rangle. \tag{5.23}$$

We call such a decomposition the *contribution spectrum* [Shudo et al. 2014]. In the following discussion, we focus only on the symmetric ground state $|\Psi_0^+\rangle$. As we mentioned in section 5.1, each eigenstate has a

symmetry with respect to the mirror transformation $\hat{\Pi}_q$ and the translation $\hat{T}_r$. Therefore, the basis $|J_\ell^{(M)}\rangle$ that has the same symmetry as $|\Psi_0^+\rangle$ is only used for the contribution spectrum.

As shown in Fig. 5.7(b2), since the maximal mode of the contribution spectrum quite efficiently describes the behavior of the splitting, we can deduce that the staircase structure must be characterized by the maximal mode. Indeed, in Ref. [Shudo et al. 2014], we have shown that the instanton-noninstanton (I-NI) transition could be explained as the switching behavior of the most dominant component in the contribution spectrum; from the one representing the instanton contribution to broad components supported around the separatrix of a central unstable fixed point. Below, we present that the dominant component controls not only the transition from instanton to noninstanton but overall signatures in the staircase structure. We will explain this by showing contribution spectra for several values of $1/h$, which are presented in Fig. 5.9.

First of all, as mentioned just above, we notice that the contribution spectrum is mainly composed of two peaks with distinct characteristics. The first one is a sharp peak located at $E = E_0^{(M)}$, and the second is composed of many components, whose center is situated around the separatrix energy. A small peak sometimes appears on the broadly spread components as a result of the interaction with a third state. The first sharp peak at $E = E_0^{(M)}$ originates from the instantion contribution that has a maximal overlap with the ground state $|\Psi_0^+\rangle$, so we hereafter call it the instanton peak. We stress again that the instanton peak at $E = E_0^{(M)}$ can be recognized only when we prepare higher order BCH expansions ($M = 7$ for the present calculation), otherwise the instanton peak is not isolated from the others and could not be identified.

In the instanton decay (the first steeply decaying) regime, which is seen in the case of $1/h$ = 12 in Fig. 5.9(a), the instanton peak dominates the other components. As a result the amplitude of the ground state $|\Psi_0^+\rangle$ at $q = 0$ is well described by the integrable Hamiltonian base $|J_0^{+,(M)}\rangle$. Hence the instanton behavior should and is actually observed.

With increase in $1/h$, the height of both peaks, the instanton peak and the broad components centered around the separatrix, gradually drop, but the speed of the former is much higher than that of the latter, eventually resulting in the switching of the role of the dominant contributor from the instanton to the top of broad components. An important remark is that the support of the state associated with the top of the broad components is outside the separatrix, meaning that the ground state is most dominantly coupled with an outside state [Shudo et al. 2014]. We notice in Fig. 5.7(b) that, exactly at this switching moment, the first instanton decay turns to the first plateau, and eigenstates show the convex structure around $q = 0$ (see

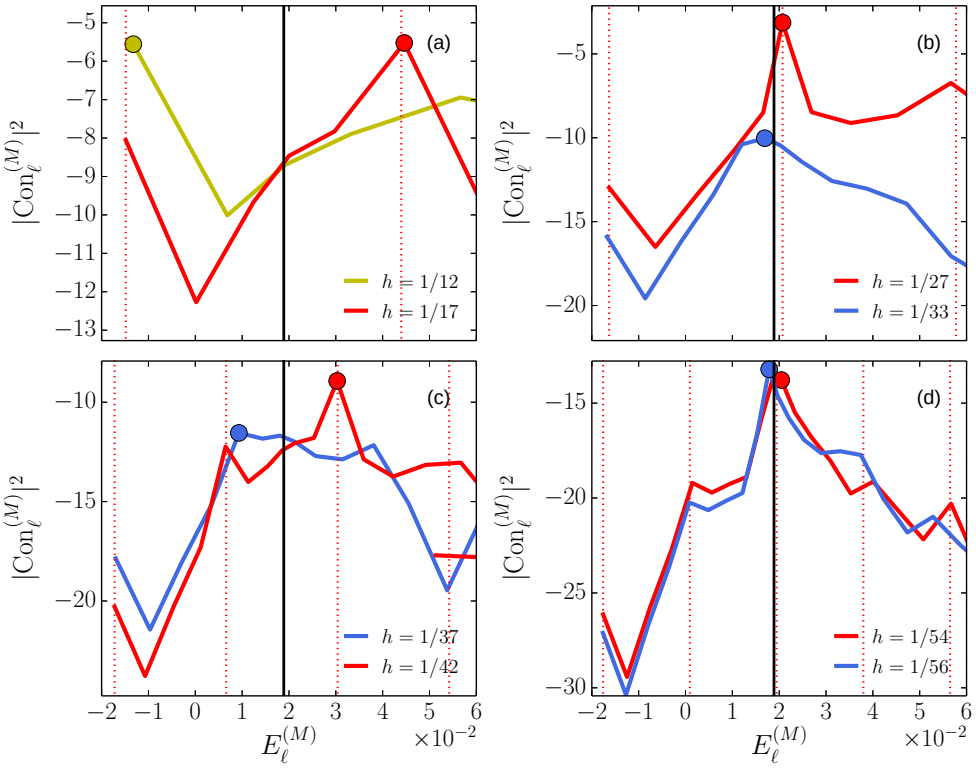

Figure 5.9: The contribution spectrum $\mathrm{Con}_\ell^{(M)}$ (in $\log_{10}$ scale) at $q = 0$ is plotted as a function of the energy $E_\ell^{(M)}$. The BCH order $M = 7$ was used. The values of h are indicated in each figure. Each panel respectively shows the case (a) before (yellow) and after (red) I-NI transition, (b) before (red) and after (blue) the transition from the first plateau to the second decaying, (c) before (blue) and after (red) the transition from the second decaying to the second plateau, (d) before (red) and after (blue) the transition from the second plateau to third steep decaying regime. The dot represents the maximal mode in each spectrum. We have used a yellow-colored curve in the region where the maximal mode is given by the instanton contribution, a red-colored when the maximal mode energy is above the separatrix energy, and a blue-colored below the separatrix energy. The thick solid line represents the separatrix energy and red dotted lines the energies satisfying the condition $E = E_0^{(M)} + mh/\tau$ $(m = 0, 1, 2, \cdots)$ (see the discussion in subsection 5.3.2).

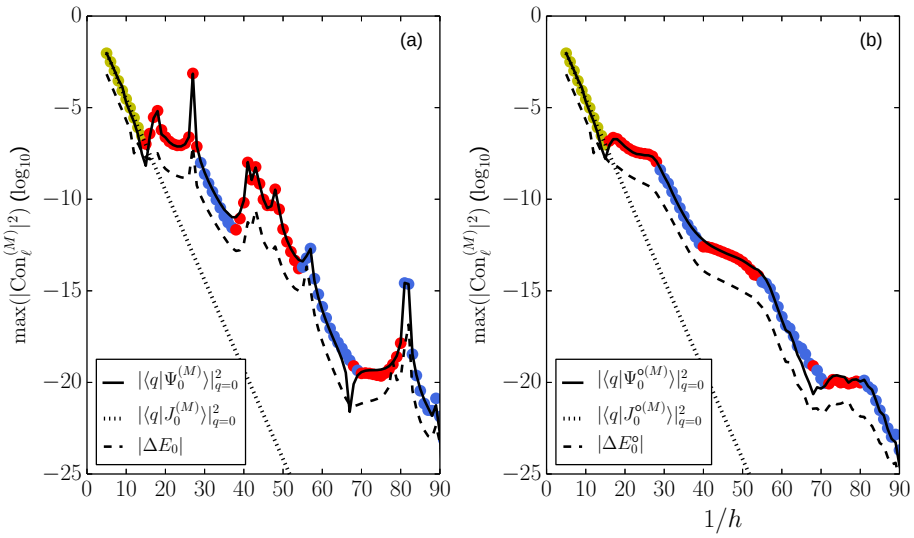

Figure 5.10: (a) Maximal modes plotted as a function of the inverse Planck's constant $1/h$. We have used yellow-colored dots in the region where the maximal mode is given by the instanton contribution, red-colored ones when the maximal mode energy is above the separatrix energy, and blue-colored below the separatrix energy. (b) Maximal modes for the absorbed eigenstates $|\tilde{\Psi}_n\rangle$. The absorption procedure is the same as that introduced in section 5.2. Here we use the integrable bases $|J_\ell^{(M)}\rangle$ as the absorber, and the absorption parameters are chosen as $s = 3$ and $\Gamma = 0.4$. The rule for color coding is the same as in (a). In both calculations, the BCH order $M = 7$ was used. In (a) the exact eigenfunction $\langle q|\Psi_0^+\rangle$ at $q = 0$, integrable basis $\langle q|J_n^{(M)}\rangle$, and energy splitting ΔE_0 are shown as solid, dotted and broken curves, respectively. In (b) the solid curve represents the absorbed eigenfunction $\langle q|\tilde{\Psi}_0^+\rangle$ at $q = 0$, and dotted and broken ones are the same as in (a).

Fig. 5.8(b)). In the perturbation calculation, it is also crucial to include outer torus states into unperturbed bases to reproduce the convex structure at $q = 0$, otherwise the resulting wavefunction cannot bend upward at $q = 0$ since it is merely a superposition of exponentially decaying states. It is important to note that not only such a convex structure just after the transition but also neighboring structures around $q = 0$ could be well reproduced only by the maximal mode in the spectrum $\mathrm{Con}_\ell^{(M)}$ (see Fig. 5.7(b2)).

In any case, the maximal mode in the spectrum $\mathrm{Con}_\ell^{(M)}$ can be a good indicator for the value of eigenstates at $q = 0$ and thereby the splitting ΔE. The maximal mode in the contribution spectrum $\mathrm{Con}_\ell^{(M)}$, which is shown using color-coded dots in the Fig. 5.10, well traces the staircase structure of the exact splitting ΔE_n, and the value of eigenstates $|\langle q|\Psi_n\rangle|^2_{q=0}$ at $q = 0$ as well. We will fully make use of this fact hereafter.

As we further increase in $1/h$, the instanton peak is completely overtaken by the broadly spread components (see Fig. 5.9(b)) and this ordering is fixed and never turned over. We also emphasize that the estimation of the critical Planck's constant h_c at which the I-NI transition occurs becomes a bit imprecise if we use the lower order BCH series.

As we increase $1/h$ after the I-NI transition, the support for the maximal mode of the contribution spectrum further approaches the separatrix, which is shown as in Fig. 5.9(b), and eventually it goes into the inner tours region in excess of the separatrix. At this moment, we realize that the splitting curve changes the behavior from the first plateau to the second steeply decaying regime (see Fig. 5.7(b)). At the same time, the structure of eigenstates at $q = 0$ changes from the convex to concave shape (see Fig. 5.8(c)).

With further increase in $1/h$ the maximal mode also shifts to the left. On the other hand, another peak is born at the right-hand edge of broad components, and now the competition comes into issue between the those peaks, the one playing a major role in the I-NI transition, and the new one at the right-hand edge. As noticed in Fig. 5.9(c), the switching of the dominant contributor again takes place between these two peaks, and at this moment the splitting curve turns from the second steeply decaying to the the second plateau regime.

After such a transition, the overtaken peak, the one playing a role in the I-NI transition, is gradually absorbed into the spectrum envelope. However it leaves a clear trace in wavefunction: As shown in Fig. 5.8(d), the shoulder or bulge observed in the neighboring region around $q = 0$ is well reproduced by the component that has played a role in the I-NI transition. The convex structure observed in the first plateau is pushed outward by the newly born component, and then it appears as shoulders. In other words, the history of the staircase structure in the splitting plot is properly recoded in the tail of wavefunction, not necessarily at $q = 0$.

The staircase structure in the splitting plot could therefore be explained by the successive switching process of maximal modes, and passing through the separatrix, that is, whether the support of the maximal mode is inside or outside the separatrix. Figure 5.10 illustrates that the staircase structure of the splitting curve can be understood by the position of the maximal mode: whether its support is outside or inside the separatrix.

We have verified, as shown in Fig. 5.10(b), that even if we suppress the peak standing on the broad peak

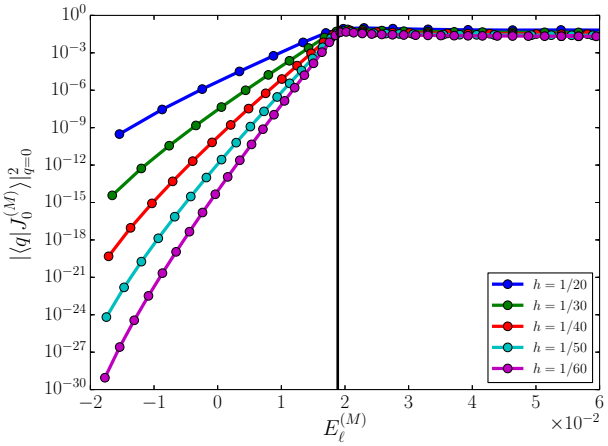

Figure 5.11: Amplitude of the integrable eigenfunction $\langle q|J_\ell^{(M)}\rangle$ at $q = 0$. The 7th order BCH Hamiltonian was used. The black vertical line shows the energy of separatrix.

components using the same absorber technique in subsection 5.2.1, this switching process still survive[3]. This implies that the switching does not occur specifically between the resonance peaks appearing in the contribution spectrum, but overall deformation of broad peak components controls it. We could identify at least the third and fourth transition and confirmed the same scenario applies.

5.3.2 Anomaly of eigenfunctions in the action representation

As shown above, we could attribute the emergence of the staircase structure to the successive switching of the dominant component in the contribution spectrum. In this subsection, we explain why the quantum number of the dominant component gradually shifts with increase in $1/h$, passing through the separatrix, and also explain why this causes the change in the slope of the splitting curve.

For this purpose, we examine the behavior of the expansion coefficient $\langle J_\ell^{(M)}|\Psi_0\rangle$ and the integrable eigenfunction $\langle q|J_\ell^{(M)}\rangle$ at $q = 0$ separately. Note that the product of these two terms constitutes each component in the contribution spectrum $\mathrm{Con}_\ell^{(M)}$. We here call $\langle J_\ell^{(M)}|\Psi_0\rangle$ the eigenfunction in the action representation.

First of all we remark that the value h/τ becomes a fundamental energy unit in our system. This is

[3]For the $1/h < 10$ regime, we only apply the absorber to the nearest eigenstate ($s = 1$), because there are few eigenstates which have same symmetry as the ground state.

because the present system is driven by the periodic force with period τ, so $2\pi/\tau \times \hbar = h/\tau$ becomes a fundamental energy unit, and the energies specified as $E_\ell^{(M)} = E_0^{(M)} + mh/\tau \ \ (m = 0, 1, 2, \cdots)$ may invoke quantum mechanical resonances. In Fig. 5.9, we have shown such energies as dotted red lines. In the following, we first describe a signature of $\langle q|J_\ell^{(M)}\rangle$ at $q = 0$ and then discuss anomaly found in $\langle J_\ell^{(M}|\Psi_0\rangle$. Combining these, we finally explain the mechanism of successive switching in the contribution spectrum.

As shown in Fig. 5.11, the amplitude of the integrable eigenfunction $\langle q|J_\ell^{(M)}\rangle$ at $q = 0$ shows exponential dependence on the energy $E_\ell^{(M)}$ as far as the energy is less than that of the separatrix (left side of the thick black line in Fig. 5.11). When plotting $\langle q|J_\ell^{(M)}\rangle$ with a fixed energy one also finds exponential decay as a function of $1/h$ (see Fig. 5.10(b)). This is an expected behavior since $\langle q|J_\ell^{(M)}\rangle$ is just an eigenfunction of an integrable Hamiltonian, no matter large the expansion order M is.

On the other hand, above the separatrix energy (right side of the thick black line), we see that the amplitude of the integrable eigenfunction $\langle q|J_\ell^{(M)}\rangle$ keeps almost constant. This is also reasonable because each $\langle q|J_\ell^{(M)}\rangle$ has its supports on a transversal invariant torus outside the separatrix, so the connection is not made via tunneling but real classical processes, thus resulting in no decay as a function of the energy.

In contrast, the nature of the eigenfunction $\langle J_\ell^{(M)}|\Psi_0\rangle$ in the action representation is highly nontrivial. As shown in Fig. 5.12(a), there exists a sharp peak at $E_0^{(M)}$, which represents the instanton contribution, and then the value of $\langle J_\ell^{(M)}|\Psi_0\rangle$ suddenly drops to reach a small level. Then it forms a *non-decaying region* in which the value of $\langle J_\ell^{(M)}|\Psi_0\rangle$ does not decrease, rather increases gradually until a small peak which is close to the energy which is specified by the relation $E = E_0^{(M)} + h/\tau$ [Hanada et al. in preparation, Shudo et al. in preparation]. This peak originates from the resonance of the associated states with the periodic forcing inherent in our model. The non-decaying region means that as long as the eigenphase difference is less than h/τ the contribution from the associated integrable basis states is almost equal. It is beyond this resonance that the exponential decay common in the ordinary tunneling tail takes place. As presented in Figs. 5.12(b)-(c), the presence of non-decaying region is not limited to the ground state but appears in exited states as well. Also note that overall features are reproduced by just one-step time evolved wavefunciton which is expressed as $\langle J_\ell^{(M)}|\Delta U_M|J_n^{(M)}\rangle$. The latter is consistent with the observation that perturbation theory based on the BCH basis works well (see Fig. 5.7(b)). We emphasize that these are all observed only when the order M of the BCH approximation is large enough and also universally appear in the eigenfunction of quantum maps [Hanada et al. in preparation, Shudo et al. 2014; in preparation].

A particularly important fact is, as shown in Fig. 5.13, that the decay rate of the height of the non-decaying region as a function of $1/h$ is extremely slow, as compared to the region $E_\ell^{(M)} > h/\tau$. This clearly distinguishes and characterizes the two regions, below and above the resonance energy $E = E_0^{(M)} + h/\tau$. We should make clear the underlying reason behind the observed power law decay in both regions, but the observed energy, so the corresponding classical structure as well, moves with increase in $1/h$ in the current setting, which makes difficult to apply a straightforward semiclassical argument.

In addition to the resonance peak at $E = E_0^{(M)} + h/\tau$, a sequence of peaks implying the higher order resonances appear at $E = E_0^{(M)} + mh/\tau$ (m integer) (see Fig. 5.12(a)). In conjunction with resonance peaks, there also exist narrow non-decaying regions just below each peak as the non-decaying region appearing in the region $E - E_0^{(M)} < h/\tau$. Such a sequence of non-decaying region is not so sharply identified in Fig. 5.12(a), but it becomes clearly visible as we increase $1/h$. We can therefore divide each sector $E_0^{(M)} + mh/\tau < E < E_0^{(M)} + (m+1)h/\tau$ into two characteristic regions; the one showing faster decay with $1/h$ and the other having quite slow decaying character. A detailed explanation will be presented in our forthcoming paper [Hanada et al. in preparation], and we just show in Fig. 5.13 the difference of the decay rate by measuring it in the middle energy in each sector. As is seen, the decay rate in the region $E_0^{(M)} + h/\tau < E < E_0^{(M)} + 2h/\tau$ is much slower than in the next sector $E_0^{(M)} + 2h/\tau < E < E_0^{(M)} + 3h/\tau$. Although we do not specify in which characteristic region the middle point energies used to measure the decay rate is contained, it is enough, in the following argument, to notice that the decay rate much differs in each sector. Also note that such resonance peaks with the same nature also appear in exited states as also shown in Fig. 5.12(b)-(c).

Putting all the pieces together, we can now understand why successive switching in the contribution spectrum generates the staircase structure. In the first decaying (instanton) region, the instanton is the most dominant and broadly spread components provide only negligible contributions, as explained in the previous subsection. The height of the instanton peak decays exponentially with $1/h$ as expected. However, in this region, the largest component in the broadly spread components is outside the separatrix (see the yellow curve in Fig. 5.11(a)), meaning that the separatrix energy is contained in the non decaying region of $\langle J_\ell^{(M)} | \Psi_0 \rangle$. Since $\langle q | J_\ell^{(M)} \rangle$ keeps constant when the position q is outside the separatrix and the decaying speed of $\langle J_\ell^{(M)} | \Psi_0 \rangle$ is so slow as shown in Fig. 5.13, its product $\mathrm{Con}_\ell^{(M)}$ also decays much slower than the instantion peak. Thus, at a certain critical $1/h_c$, the instanton component is overtaken by the dominant

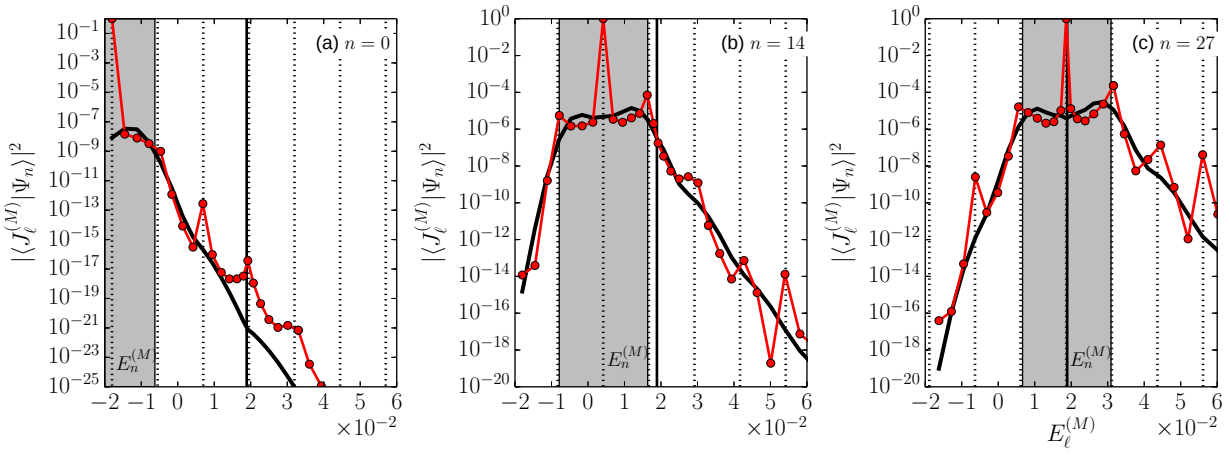

Figure 5.12: Eigenstates $\langle J_\ell^{(M)}|\Psi_n\rangle$ in the action representation plotted as a function of $E_\ell^{(M)}$ for $h = 1/80$ for (a) $n = 10$, (b) $n = 15$ and (c) $n = 25$, respectively. The black curves show the matrix elements $\langle J_\ell^{(M)}|\Delta\hat{U}|J_n^{(M)}\rangle$. Here we used the 7-th order BCH Hamiltonian as the basis $|J_\ell^{(M)}\rangle$. The black solid line and dotted lines respectively show the separatrix energy, and the energies satisfying the condition $E = E_0^{(M)} + mh/\tau$ $(m = 0, 1, 2, \cdots)$.

component in the broadly spread components. This is nothing but the I-NI transition [Shudo et al. 2014].

After the I-NI transition, as long as the position of the dominant contribution in the broadly spread components is outside the separatrix, the decaying behavior in the plateau of $\langle J_\ell^{(M)}|\Psi_0\rangle$ controls the product $\langle q|J_\ell^{(M)}\rangle\langle J_\ell^{(M)}|\Psi_0\rangle$. This explains the presence of plateau in the splitting curve.

However, note that the position of the dominant component is determined by the edge of the plateau of $\langle J_\ell^{(M)}|\Psi_0\rangle$, and this edge is located around the value h/τ. As a result, at a certain value of $1/h$, the position of the dominant contribution passes through the separatrix (see Fig. 5.9(b)). If such an event occurs, the separatrix energy is then situated in the region where $\langle J_\ell^{(M)}|\Psi_0\rangle$ shows faster decay. This is exactly the moment when the splitting curve turns from the first plateau to the second steeply decaying region.

The mechanism generating the next plateau is understood by observing $\langle J_\ell^{(M)}|\Psi_0\rangle$ in a wider range. As shown in Fig. 5.12(a), a sequence of peaks appears at integer multiples of the fundamental energy unit h/τ, and the decay rate of $\langle J_\ell^{(M)}|\Psi_0\rangle$ just below each resonance peak is again very slow as compared in the next sector, as demonstrated in Fig. 5.13. Hence the same switching process takes place repeatedly. We have actually checked that the mechanism explained here works at least until the third plateau, but we expect that this continues in larger $1/h$ regimes.

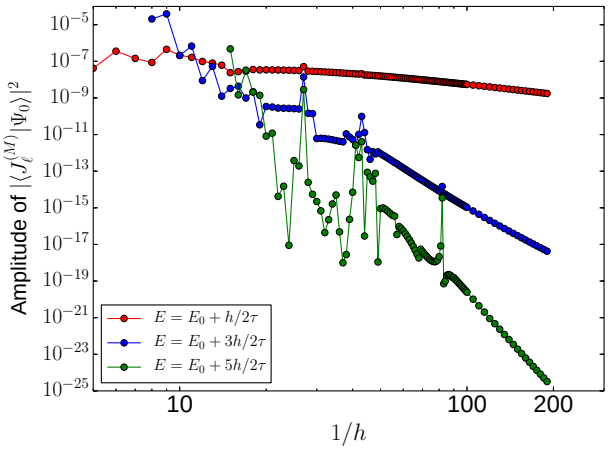

Figure 5.13: The inverse Planck's constant $1/h$ dependence of $\langle J_\ell^{(M)}|\Psi_0\rangle$. Difference of colors distinguishes the energy at which the value of $\langle J_\ell^{(M)}|\Psi_0\rangle$ is evaluated (see the inner panel).

In this way, we could explain the emergence of the staircase structure based on the nature of the action representation, which seems to be closely connected with the fundamental energy sequence whose unit is given as h/τ. As was checked above, the fundamental energy sequence can induce quantum resonances, resulting in the spikes in the splitting curve. However, it should be noted that the appearance of quantum resonances is not a necessary condition for the presence of the staircase structure, as discussed in the subsection 5.2.2 and 5.3.1. In other words, even if the resonance condition is not satisfied, a broadly spread or mild peak, whose width is almost comparable to the fundamental energy unit h/τ, survives around the fundamental energy sequence. This is quite an anomalous situation because such a broad peak implies the existence of periodic oscillation of period τ accompanied by a rapid decaying process whose life time is comparable to the oscillation period itself [Shudo et al. in preparation].

We also characterize this anomaly from the viewpoint of semiclassical theory. If the leading-order semiclassical approximation works, the matrix element $\langle J_\ell^{(M)}|\Delta\hat{U}_M|J_0^{(M)}\rangle$ should take a form of $\Psi \sim \sum_\gamma A_\gamma e^{-iS_\gamma/\hbar}$, where A_γ and S_γ respectively stand for the amplitude and classical action, and the sum γ is taken over complex classical orbits satisfying given initial and final conditions. In the semiclassical regime, we may neglect the $\hbar$ dependence in the amplitude A_γ, so the matrix element $\langle J_\ell^{(M)}|\Delta\hat{U}_M|J_0^{(M)}\rangle$ is approximately expressed using the minimum imaginary action $\mathrm{Im}\, S_{\gamma_0}$ as $\Psi \sim e^{-\mathrm{Im}\, S_{\gamma_0}/\hbar}$. Since $\mathrm{Im}\, S_{\gamma_0}$ is a purely classical quantity, the form $\hbar \ln\langle J_\ell^{(M)}|\Delta\hat{U}_M|J_0^{(M)}\rangle$ should not depend on $\hbar$. As will be shown in Fig. 5.17, this is indeed the case in the integrable system. On the other hand, Fig. 5.14 shows that the

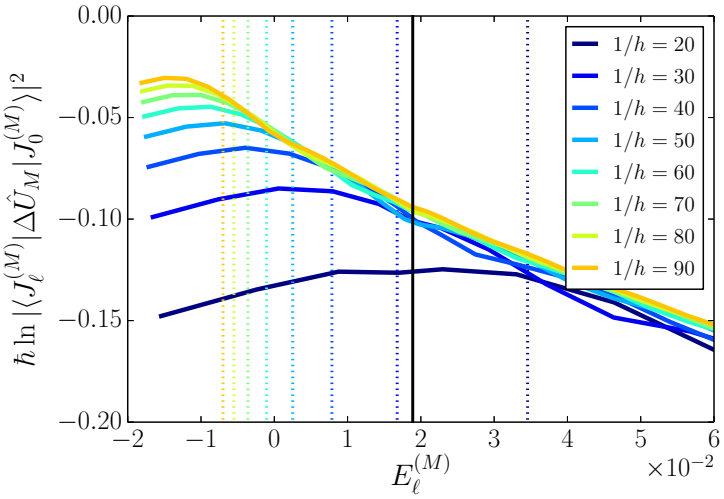

Figure 5.14: Scaled wavefunction $\hbar \ln |\langle J_\ell^{(M)}|\Delta U|J_\ell^{(M)}\rangle|^2$ as a function of $E_\ell^{(M)}$ for several effective Planck's constant h. The black solid line and dotted lines respectively show the separatrix energy, and the energies satisfying the condition $E = E_0^{(M)} + h/\tau$

matrix element $\langle J_\ell^{(M)}|\Delta\hat{U}_M|J_0^{(M)}\rangle$ does not follow the semiclassical ansatz in the non-decaying region, whereas the leading-order semiclassical prediction seems to work well beyond the non-decaying region. Although it is necessary to check whether or not the leading-order semiclassical approximation indeed breaks in the non-decaying region, the observed sharp distinction would be an important signature characterizing anomaly.

According to these speculations, we are currently taking two approaches to understand what was observed in the eigenstate $\langle J_\ell^{(M)}|\Psi_0\rangle$ in the action representation; one is a real semiclassical analysis which is based on the so-called classical-quantum correspondence principle. This could extract anomalous components hidden in classical dynamics generated by the BCH Hamiltonian, and actually reproduce anomalous decay tails [Shudo et al. in preparation]. Another approach is to take into account higher-order effects in the semiclassical analysis. Since similar non-decaying or anomalous behaviors have been found in the model with discontinuity in phase space, observed phenomena might be liked to or have at least close similarity with diffraction [Ishikawa et al. 2012]. This naturally leads us to the semiclassical treatment beyond the leading order. In any case, these are out of the scope of the present paper, and will be reported closely in our forthcoming paper [Hanada et al. in preparation].

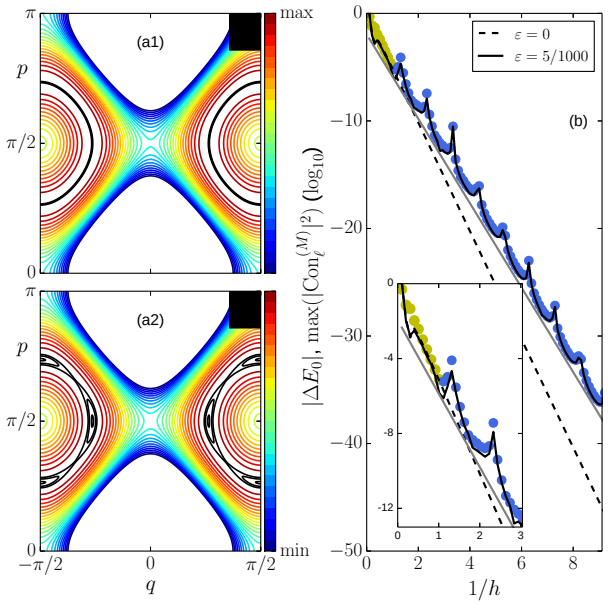

Figure 5.15: Phase space portrait for the Hamiltonian (5.24) for $a = -0.55$ and (a1) $\varepsilon = 0$ and (a2) $\varepsilon = 5/1000$. The black curves show the energy contour whose energy value is close to the maximum one. The black box put in the upper right corner represents the size of effective Planck's constant for $h = 1/5$. (b) The splitting ΔE_0 (in $\log_{10}$ scale) as a function of $1/h$ in the cases of $\varepsilon = 0$ (black dashed line) and $\varepsilon = 5/1000$ (black solid line). Yellow ad blue dots represent the maximal mode of the contribution spectrum $\mathrm{Con}_\ell^{(M)}$ at $q = 0$ for $\ell = 0$ and for $0 < \ell/N < 1/2$, respectively. The gray line shows the slope of the splitting curve for $\varepsilon = 5/1000$. The inset is magnification of a small $1/h$ regime.

5.4 Splitting curves in integrable systems

In the previous subsection, we discussed the underlying mechanism controlling the staircase structure of the splitting curve and found that anomalous tails in eigenfunctions in the action representation play a key role. If such a feature is shared only in nonintegrable maps, we would not expect the enhancement of the tunneling probability in the completely integrable system. Below we shall explain, the nature of the splitting curve in the integrable system is totally different, although a seemingly common behavior is observed.

For this purpose, let us consider the following classically integrable Hamiltonian [Le Deunff et al. 2013]

$$H(q,p) = H_0(q,p) + \varepsilon H_1(q,p) \tag{5.24}$$

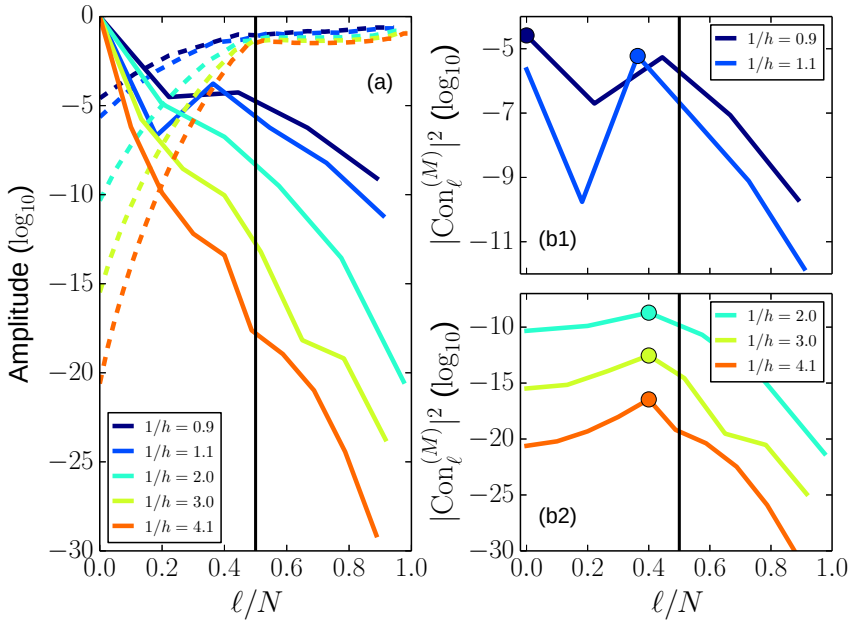

Figure 5.16: (a) The amplitude of $\langle q|\Psi_\ell\rangle$ at $q = 0$ (dashed curves) and the action representation $\langle J_n|\Psi_0\rangle$ (solid curves) as a function of the normalized quantum number ℓ/N. Right panels give the contribution spectrum $\mathrm{Con}_\ell^{(M)}$ ($\log_{10}$) as a function of the normalized quantum number ℓ/N for (b1) a small $1/h$ regime, and (b2) a semiclassical regime.

with

$$H_0(q,p) = (\cos^2 q + \cos^2 p)/2 + a(\cos^2 q + \cos^2 p)^2, \tag{5.25a}$$

$$H_1(q,p) = \cos^4 p - 6\cos^2 p \cos^2 q + \cos^4 q. \tag{5.25b}$$

as discussed in section 3.3[4].

We impose the periodic boundary condition on the region $(q,p) \in (-\pi,\pi] \times (0,\pi]$, and solve the eigenvalue problem

$$\hat{H}(\hat{q},\hat{p})|\Psi_n^\pm\rangle = E_n^\pm|\Psi_n^\pm\rangle. \tag{5.26}$$

We then consider the splitting $\Delta E_0 = E_0^+ - E_0^-$ of the ground and first exited states, both localizing in the inner well. Here we take the innermost state in the inner well as the ground state and arrange the eigenstates in the same order as the standard map.

[4]Here we take $\phi = 0$

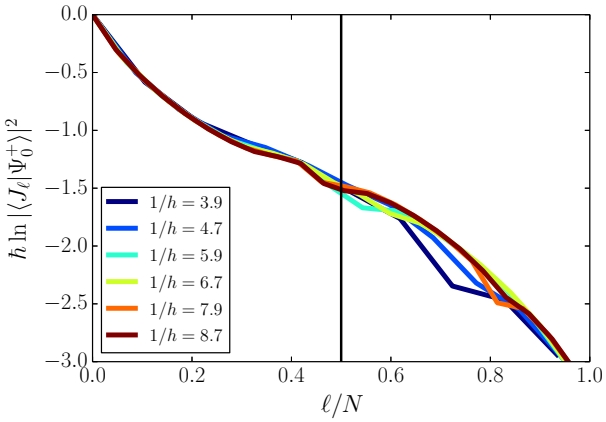

Figure 5.17: Scaled wavefunciton $\hbar \ln |\langle J_\ell|\Psi_0^+\rangle|^2$ as a function ℓ/N for several effective Planck's constant h, each of which is taken at the values of off resonance positions in Fig. 5.16(b).

Figure 5.15(b) gives the splitting ΔE_0 as a function of $1/h$. As discussed in section 3.3, the splitting curve has a crossover and decays exponentially accompanied with periodic spikes. Such a crossover or the change of the slope of the splitting curve reminds us of the plateau discussed in the nonintegrable situation. However, the origin and the underlying mechanism entirely differs from the previous one. This can be confirmed again by examining the contribution spectrum. Here we use the eigenstates $|J_n\rangle$ as the basis states for the contribution spectrum, where $\hat{H}_0(\hat{q},\hat{p})|J_n\rangle = E_n^{(0)}|J_n\rangle$.

As shown in Fig. 5.16(b1), a switching from the instanton to another mode also occurs, like the standard map case. However, in the integrable case, the position of the peak sits at the same value of ℓ/N and does not move even if the value of $1/h$ is changed, while remember that it depends on $1/h$ and shift leftwards in case of the standard map. Note here that ℓ/N can be identified with the action coordinate. The reason for the peak position being fixed is simple; the peak appears as a result of the coupling between inner and outer surface, which is expected to occur in the RAT scenario. Alternatively stated, the origin of coupling is purely classical. Furthermore, as shown in Fig. 5.17, the leading-order semiclassical anstaz, which was discussed in the previous section, works quite well for the eigenfunction in the action representation. These results make a sharp contrast to the standard map case. We can see in Fig. 5.18 that the maximal mode in the contribution spectrum well reproduces the structure of eigenfunction around $q = 0$, and its support is exactly an invariant curve with the same energy as that of the ground state.

As discussed in section 3.3, there exist two different complex paths with different imaginary actions. One

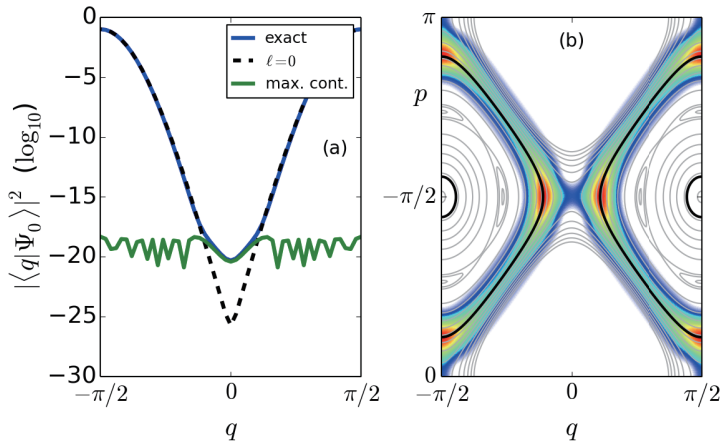

Figure 5.18: (a) The eigenfunction $|\Psi_0\rangle$ in the q-representation for $\varepsilon = 5/1000$ (blue), the eigenfunction $|J_0\rangle$ (dotted) and the maximal mode in the contribution spectrum at $q = 0$ (green), respectively. (b) The maximal mode state in the Husimi representation for $h = 1/5$. The black thick curves represent inner and outer invariant curves with the same energy $E = E_0$.

corresponds to the ordinary instanton path, which runs from one well to another directly and the other is the path bypassing the classical resonance chain. In the semiclassical regime, since the latter one has a smaller imaginary action. On the other hand, in a small ε regime, it can happen that the instanton contribution is larger than that from the bypassing one, in spite of the magnitude relation of imaginary actions. This is because the prefactor, more precisely the coupling amplitude due to tunneling, comes into play in a relatively small $1/h$ regime. The observed crossover would be understood by taking into account not only the imaginary action but the coupling amplitude. This argument suggests that, in a larger ε regime, the coupling with bypassing path gets larger, and the crossover point disappears when the value of ε exceeds a certain threshold. Note, however that the splitting curve cannot form the staircase structure since we have at most two possible complex paths, and the underlying mechanism generating spikes has a purely classical origin as stated above.

Chapter 6

Summary and outlook

In this thesis we have discussed essential differences of quantum tunneling in integrable and non-integrable systems and discussed the origin of the enhancement of tunneling probability in non-integrable systems. We especially measured the tunneling probability by observing tunneling splittings plotted as a function of the inverse Planck's constant or the quantum number. Typical features of the splitting curve commonly observed in nonintegrable quantum maps are the existence of spikes and persistent departure of the splitting curve from the one predicted by the instanton.

So far these have been discussed in the framework of RAT theory, but here we took a different perspective: the splitting curve is composed of the staircase-shaped backbone accompanied by spikes. We have observed that, by introducing the absorber composed of integrable bases, spikes could be selectively suppressed if states interacting with the reference doublet are absorbed. More precisely, we have shown that the interacting or third state could be decoupled from the reference doublet when we take an integrable state that has maximally overlap with the corresponding eigenstate as the absorber. The eigenenergy of such eigenstates responsible for generating spikes are pushed out to the complex plane, and spikes disappear. Our observation was that even though all the third states which resonate energetically with the reference doublet are suppressed in such a way the staircase structure survives. Note that the efficiency of the present absorber comes from the fact that the regime we consider is close enough to the integrable limit, otherwise the absorber may affect irrelevant states in an uncontrollable way.

The result strongly suggests the existence of non-trivial broad interaction between the reference doublet

and other states. This was indeed confirmed by introducing renormalized Hamiltonian, which is constructed using the BCH expansion, and used as basis states by which the reference state is expanded. In particular, we focus on the contribution spectrum at the origin $q = 0$ since the amplitude of eigenfunctions at the origin follows the behavior of tunneling splitting. Here the contribution spectrum introduced in [Shudo et al. 2014] represents components of renormalized states in the reference state.

The contribution spectrum analysis clearly revealed that, in addition to the self component representing the instanton, there certainly exists broad interaction, and the behavior of such broadly spread components controls the staircase structure in the splitting curve. There are two key ingredients to explain the emergence of the staircase: one is the behavior of the most dominant state in broad components, the other is anomalous tail observed in the eigenfunction in the action representation. Note that the renormalized bases are crucially important to capture these features, otherwise one could not explain the existence of the staircase structure and the anomalous tail part in the action representation as well.

The dominant contributor in the broadly spread components switches from one to another, which was observed in the contribution spectrum. Such a switching phenomenon is driven by and liked to the existence of the fundamental energy sequence, which is further enhanced when the quantum resonance between unperturbed system and the periodic driving occurs.

The origin of anomalous part in the action representation should be explored more closely, which will become a primary subject of our future works. The semiclassical analysis based on the correspondence principle, in which not complex but real classical orbits are used as input information. This efficiently works and turns out to extract anomalous components in classical dynamics of the BCH Hamiltonian [Shudo et al. in preparation]. The analogy with the system modeling the diffraction, together with some speculations on anomalous behaviors of caustics appearing in the semiclassical analysis will be another approach [Hanada et al. in preparation]. The latter suggests that observed phenomena in the eigenfunction in the action representation are beyond the leading semiclassical description.

These two key characteristics are, by their very nature, absent in the completely integrable system. Therefore, one could predict that the staircase structure does not appear in the completely integrable. We have confirmed this for a normal form Hamiltonian system, for which the validity of RAT theory was recently investigated. We have shown that a sharp contrast exists between integrable and nonintegrable systems and verified that the dominant contributor in the contribution spectrum for the integrable system sits at the same

position and does not move as in the nonintegrable case. The absence of the staircase structure could simply be interpreted by the fact that there exists a unique dominant complex path in the semiclassical regime.

We would like to emphasize the importance of observing wavefunctions in the whole range, not focusing only on the amplitude at a specific point, like the origin $q = 0$ in the present case. As discussed in subsection 5.3.1, with increase in $1/h$, the convex structure around the origin, appearing in the first plateau, is pushed outward and forms shoulders in both sides. The same process happens repeatedly as one further increases $1/h$, that is, similar shoulders appear one after another. In this sense, we can find the trace of the staircase of the splitting curve in the tail pattern of wavefunction. This is also true for wavefunction in the action representation. There exists a significant difference between inner and outer tunneling tail, and this exactly results in different slopes of the splitting curve and thus staircase skeleton.

Appendices

Appendix A

Absorbing operator for quantum map

The absorbing operator is used for various purposes, but an improper setting may induce unfavorable or uncontrollable effects caused by diffraction. In this appendix, we discuss side effects of the absorber by testing several types of absorbers. The organization of this appendix is as follows: In section A.1, we introduce the absorbing operator and show how the absorber affects the nature of wave functions, in particular for one-step time evolved wave function. In section A.2, we consider the eigenvalue problem for the absorbing operator. In the last section A.3, we discuss the relation between the decay rate and the splitting.

A.1 Time evolution with absorbing operator

The quantum map is often used to discuss the quantum manifestation of classical chaos not only in the closed system such as the standard map but also in the open system such as the Hénon map. The latter systems need to absorb wave packets near the edges of boundary when one performs numerical calculations. The quantum map with the absorbing operator is expressed as

$$\hat{U}^{\circ} = \hat{P}\hat{U}, \quad \text{or} \quad \hat{U}^{\circ} = \hat{P}\hat{U}\hat{P}, \tag{A.1}$$

where the absorbing operator is expressed as $\hat{P} = e^{-\hat{V}^{\circ}(x)/\hbar}$ using a complex potential

$$V^{\circ}(x) = -if(x), \quad \text{or} \quad V^{\circ}(x) = -if(x)\theta(x - x_c) \tag{A.2}$$

where θ is the step (or smoothed step) function which is 1 for $x > x_c$ and 0 for $x < x_c$. Such a complex potential (A.2) is widely used for many purposes in scattering theory and is generally called the *optical potential*. The choice of the functional form of $f(x)$ is the most important. The function $f(x)$ has to grow smoothly and rather slowly with x in order to prevent unphysical refraction or diffraction [Vibok and Balint-Kurti 1992].

For a N-dimensional quantum map $\hat{U}$, we take the leading order expression for the absorbing operator as

$$\hat{P} := \mathbb{1} - \hat{V}^{\circ}, \tag{A.3}$$

where $\mathbb{1}$ is the identity operator. Let $|\alpha\rangle$ be an arbitrary function or an orthogonal basis ($\sum_{\ell=0}^{N-1} |\alpha_\ell\rangle\langle\alpha_\ell| = \mathbb{1}$), the complex potential is then introduced as

$$\hat{V}^{\circ} = \frac{\Gamma}{2}|\alpha\rangle\langle\alpha|, \quad \text{or} \quad \hat{V}^{\circ} = \frac{\Gamma}{2}\sum_{\ell\in L}|\alpha_\ell\rangle\langle\alpha_\ell|, \tag{A.4}$$

where the summation ℓ runs over a given index set $L = \{\ell : \ell \text{ is an integer in } 0 < \ell < N-1\}$ and $\Gamma \leq 2$ represents the absorbing strength. This type of the absorbing operator was discussed in chapter 5 (see also also Kaplan [1999]).

We consider the (non-unitary) time evolution operator with the absorbing operator,

$$\hat{U}^{\circ} = \hat{P}\hat{U}, \tag{A.5}$$

and give the propagator as

$$\begin{aligned}\langle q'|\hat{P}\hat{U}|p\rangle &= \langle q'|\hat{U}|p\rangle - \frac{\Gamma}{2}\sum_{\ell\in L}\langle q'|\alpha_\ell\rangle\langle\alpha_\ell|\hat{U}|p\rangle, \\ &= \langle q'|\hat{U}|p\rangle - \frac{\Gamma}{2}\sum_{\ell\in L}\sum_{q''}\langle q'|\alpha_\ell\rangle\langle\alpha_\ell|q''\rangle\langle q''|\hat{U}|p\rangle.\end{aligned} \tag{A.6}$$

If the absorber is the delta function $\langle q|\alpha_\ell\rangle = \delta(q - q_\ell)$, the propagator takes the form as

$$\begin{aligned}\langle q'|\hat{P}\hat{U}|q\rangle &= \langle q'|\hat{U}|q\rangle - \frac{\Gamma}{2}\sum_{\ell\in L}\sum_{q''}\delta_{q',q''}\langle q''|\hat{U}|q\rangle, \\ &= \begin{cases} \langle q'|\hat{U}|q\rangle & (q' \neq q_\ell), \\ \langle q'|\hat{U}|q\rangle - \frac{\Gamma}{2}\langle q'|\hat{U}|q\rangle & (q' = q_\ell). \end{cases}\end{aligned} \tag{A.7}$$

As we can see from Eq. (A.7), the transition amplitude from q to q' vanishes. Especially, this is exactly zero when the absorbing strength is set to $\Gamma = 2$. In the following examples, we consider the symmetrized standard map

$$\hat{U} = e^{-\frac{i}{\hbar}V(q)\frac{\tau}{2}}e^{-\frac{i}{\hbar}T(p)\tau}e^{-\frac{i}{\hbar}V(q)\frac{\tau}{2}} \tag{A.8}$$

where $T(p) = p^2/2$, $V(q) = k\cos(q)$ and parameters $k = 1$, $\tau = 1$ are used.

Delta function-type absorber

Let us consider the case where the delta function $\langle q|\alpha\rangle = \delta(q)$ is taken as the absorber. The one-step time evolution with absorbing operator is given as

$$|\psi_1\rangle = \hat{U}^{\circ}|\psi_0\rangle. \tag{A.9}$$

Here we take a minimum packet as the initial wave packet

$$\langle q|\psi_0\rangle = \left(\frac{1}{\pi\hbar^2}\right)^{1/4} e^{-(q-q_c)^2/2\hbar + ip_c(q-q_c)/\hbar}, \tag{A.10}$$

whose its center is chosen as $(q_c, p_c) = (-0.8, 0.8)$ and the periodic boundary condition on $q \in (-\pi, \pi]$ is imposed. Figures A.1(a)-(c) show the Husimi-representation of the initial packet, the one-step time evolution driven by $\hat{U}$ and $\hat{U}^{\circ}$, respectively. As we seen in Figs. A.1(b) and (c), we cannot identify the effects of the absorbing operator in the Husimi-representation in the normal scale[1], but it can be seen in the wave function in the q-representation.

As shown in Fig. A.2, the amplitude at $q = 0$ drops gradually to zero with increase in the absorbing

[1] the absorbing effect could identify in log scale.

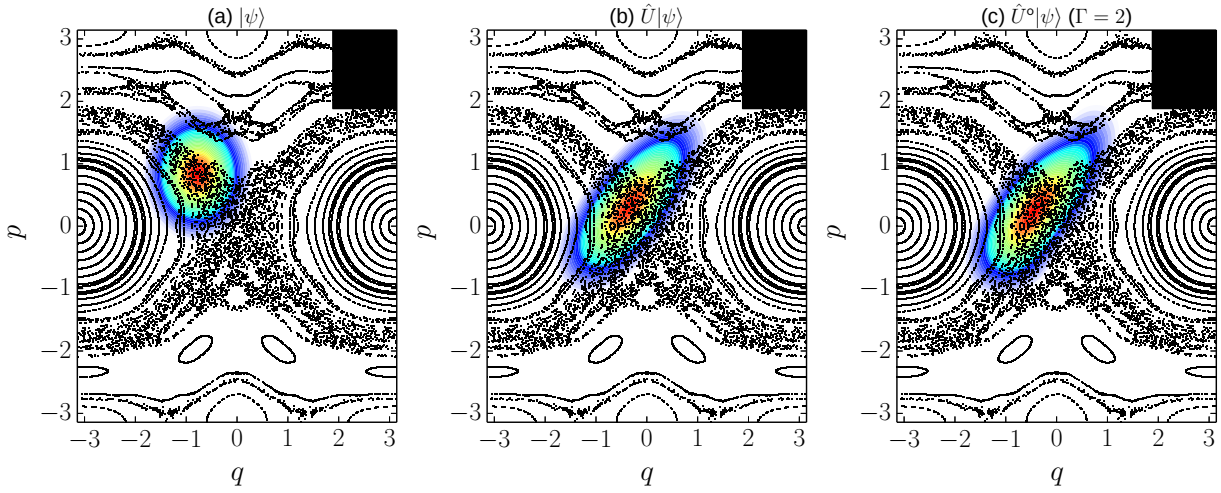

Figure A.1: The Husimi-representation of (a) the initial condition, (b) 1 step time evolution driven by $\hat{U}$ and (c) 1 step time evolution driven by $\hat{U}^{\circ}$ in which the absorber strength is chosen as $\Gamma = 2$. Black boxes put in the upper right corner indicate the size of the effective Planck's constant $h = 2\pi \times 8\pi/100$. Here we use the delta function $\langle q|\alpha\rangle = \delta(q)$ as the absorber.

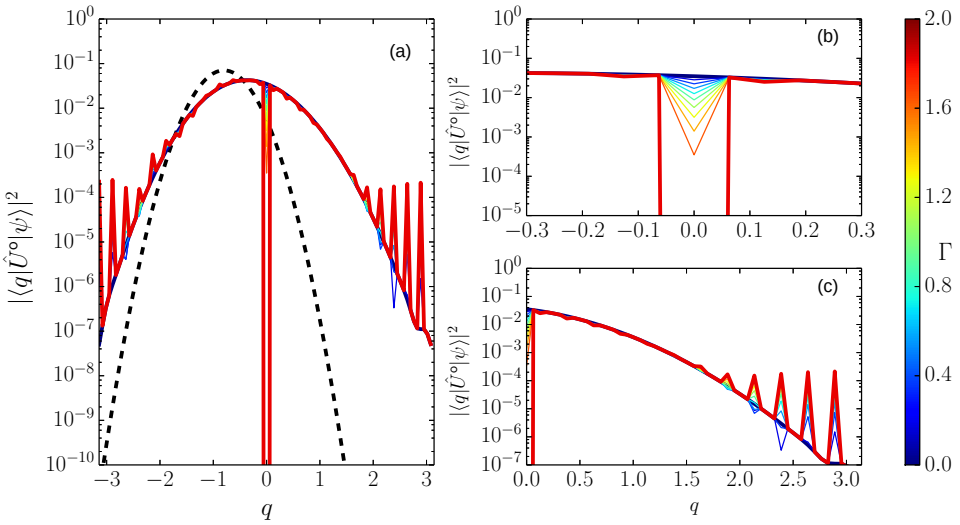

Figure A.2: (a) The wave function in the q-representation after the one-step time evolution by $\hat{U}^{\circ}$. The magnification (b) in the neighborhood of $q = 0$ and (c) for the regime $q > 0$. Each colored curve distinguishes the absorbing strength Γ (see the right-hand color bar). The initial wave function is drawn as the black dashed curve in the panel (a). Here we use the delta function $\langle q|\alpha\rangle = \delta(q)$ as the absorber.

strength Γ and it becomes exactly zero for $\Gamma = 2$ as expected. For $q \neq 0$, the amplitude of wave function oscillates and its height becomes larger with increase in the absorbing strength Γ. This oscillation is not a numerical artifact but has a definite origin in the nature of absorbing operator. The wave function in the p-representation for the one-step time evolution becomes quite singular. As can be seen in Fig. A.3, the wave packet in the asymptotic regime $|p| \gg 1$ should decay exponentially because the transition process is supposed to occur as tunneling. For $\Gamma > 0$ cases, on the other hand, the amplitude of the wave function $|p| \gg 1$ is larger than the unitary ($\Gamma = 0$) case.

The effect induced by the absorbing operator becomes clearer when one considers the difference between the unitary and absorbed time evolution

$$|\Delta\psi_1\rangle = \hat{U}|\psi_0\rangle - \hat{U}^{\circ}|\psi_0\rangle. \tag{A.11}$$

Figures A.1(b) and (c) demonstrate the Husimi-representation of the difference $|\Delta\psi_1\rangle$ of the wave functions. We can clearly identify that the wave function propagates in the $p = 0$ direction. This result tells us that the delta function absorber invokes an artificial propagation of wave packet, which is not brought by the original dynamics. Such a propagation should be distinguished from the dynamical tunneling process. This phenomenon always occurs irrespective of underlying classical dynamics, whether the system is integrable or not. This obviously originates from diffraction induced by discontinuous nature of the delta function.

Local absorption

The delta function type absorber induces the diffraction which propagates over the whole phase space. By choosing the absorber in a proper way, however, we may suppress the effect induced by diffraction. Here we consider the local absorption using minimum packets.

Let the minimum wave packet Eq. (A.10) be the absorber $|\alpha\rangle$ whose center is chosen as $(q_c, p_c) = (0.0)$. We then consider the one-step time evolution driven by $\hat{U}^{\circ}$. Figures A.4(a) and (b) respectively show a time-evolved wave function $\hat{U}^{\circ}|\psi\rangle$ in q- and p-representations for which initial condition is taken as the same in the previous demonstration. With increase in the absorbing strength Γ, the amplitude around $q = 0$ and $p = 0$ gradually drops to a certain value, however, it seems not to vanish completely. On the other hand, the amplitude of the overlapping with the absorber $\langle\alpha|\hat{U}^{\circ}|\psi\rangle$ drops to zero exactly for the absorbing

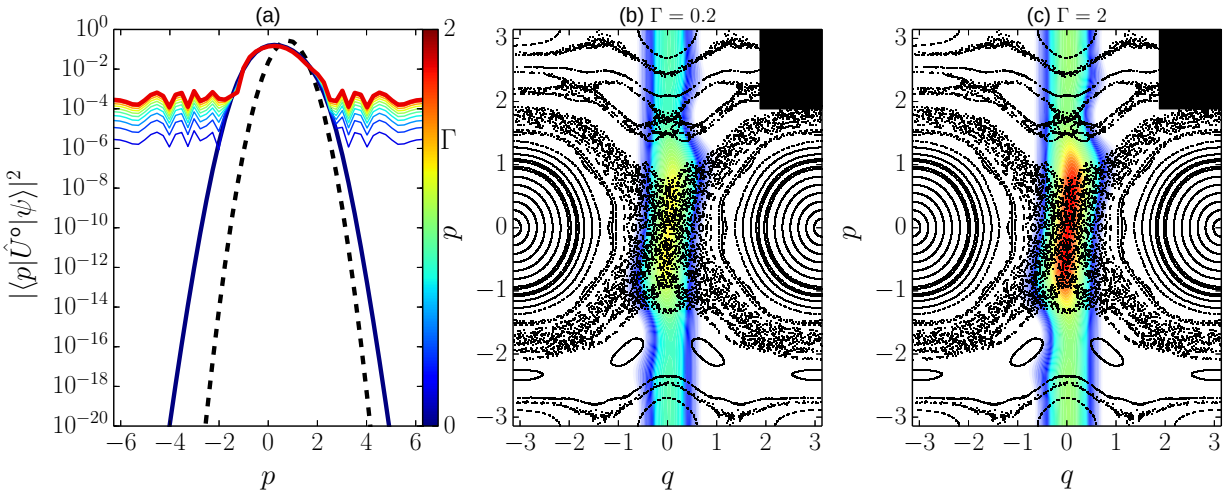

Figure A.3: (a) The wave function in p-representation after the one-step time evolution by $\hat{U}^{\circ}$. Each colored curve distinguishes the absorbing strength Γ (see the right-hand color bar). The Husimi-representation of difference of wave functions defined by Eq. (A.11) (b) for the perturbation strength $\Gamma = 0.2$ and (c) $\Gamma = 2$. Here we use the delta function $\langle q|\alpha\rangle = \delta(q)$ as the absorber.

strength $\Gamma = 2$ as expected. These behaviors seem not to be consistent with each other, but there is a pitfall: the representation of the wave function. The wave function in the Husimi-representation makes the absorbing effect clearer. As shown in Figs. A.5(a) and (b), the amplitude of the Husimi-representation at $(q, p) = (0, 0)$ gradually disappears with increase in the absorbing strength Γ. As compared to the unitary ($\Gamma = 0$) case (see Fig. A.1(b)), we also notice that the wave function propagates around the side of the absorber, which propagation is indicated by the white arrow in Fig. A.5(b). This propagation should be also attributed to also due to diffraction induced by the absorber. This diffractive propagation is the reason why the amplitude around $q = 0$ or $p = 0$ does not completely vanish. In other words, the absorber acts as not only the absorber but also the scatterer. As seen from the Husimi-representation for the difference of wave functions defined by Eq. (A.11), the absorbing effects well localize around $(q, p) = (0, 0)$ compared with the delta function type absorber.

A.2 Eigenvalue problem with absorbing operator

In the previous section, we discussed the advantage and disadvantage when applying the absorbing operator and also stressed the importance of the representation we observe. In this section, we consider the eigenvalue

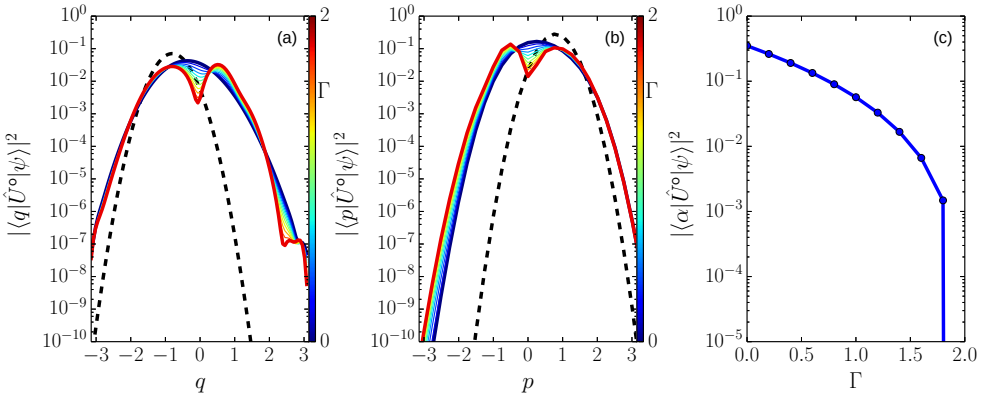

Figure A.4: Wave function in the (a) q- and (b) p-representation after the one-step time evolution by $\hat{U}^{\circ}$, respectively. Each colored curve distinguishes the absorbing strength Γ (see the right-hand color bar). (c) The overlapping amplitude with absorber $|\alpha\rangle$ as a function of Γ. Here we use the minimum packet centered at $(q_c, p_c) = (0, 0)$ as the absorber.

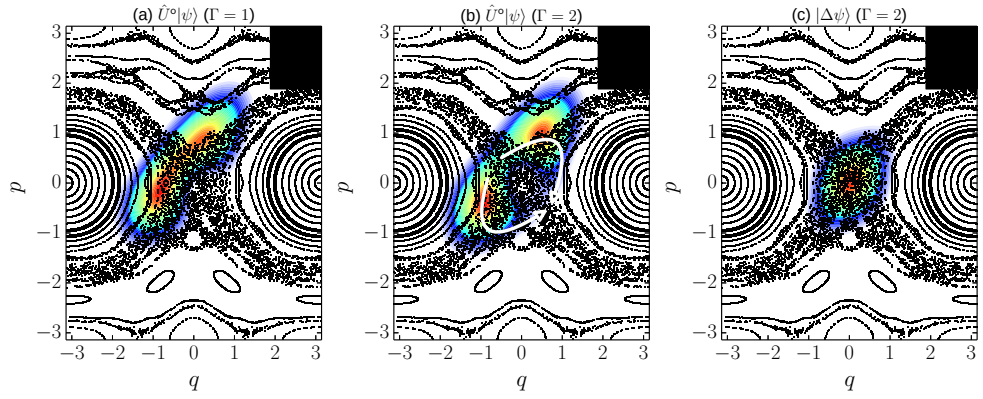

Figure A.5: The Husimi-representation after the one-step time evolution by $\hat{U}^{\circ}$ whose the absorbing strength (a) $\Gamma = 1$ and (b) $\Gamma = 2$, respectively. (c) The difference of wave functions in the Husimi-representation defined by Eq. (A.11). Here we use the minimum packet centered at $(q_c, p_c) = (0, 0)$ as the absorber.

problem for the absorbed (non-unitary) time evolution operator $\hat{U}^\circ$

$$\hat{U}^\circ|\Psi_n^\circ\rangle = u_n^\circ|\Psi_n^\circ\rangle. \tag{A.12}$$

The absorbing effect is understood by the standard perturbation theory as discussed in section 5.2.1.

First of all, we introduce the delta function-type absorber $\langle q|\alpha\rangle = \delta(q)$, and numerically solve the eigenvalue problem under the periodic boundary condition $(q,p) \in (-\pi,\pi] \times (-\pi,\pi]$. Figure A.6 shows the absorbed eigenstate of the ground state $n = 0$. The amplitude at $q = 0$ of the eigenstate in the q-representation gradually drops to zero with increase in the absorbing strength Γ and the absorber does not seem to affect the wave function at $q \neq 0$. On the other hand, the eigenstate in the p-representation at $|p| \gg 1$ is clearly affected by the absorber in a similar way as in the time domain case. It is helpful to see the difference of wave functions

$$|\Delta\Psi_n\rangle = |\Psi_n\rangle - a|\Psi_n^\circ\rangle, \tag{A.13}$$

where coefficient $a = \langle\Psi_n|\Psi_n^\circ\rangle$. As shown in Fig. A.7, the position influenced by the absorber does not localize at $q = 0$ but propagates in some directions. This propagating pattern is different from the one-step time evolution. The Husimi-representation of Eq. (A.13) does not localize on $q = 0$ but it seems to propagate over the whole phase space. As pointed out above, the absorber plays a role of the scatter, but it can generally invoke a complicated propagation, so it is not easy to understand how the pattern of the Husimi-representation is deformed as a result of such an effect. In any case, we can at least say the delta function type absorber is not suitable for the study of tunneling effect.

Next, we examine the absorbed eigenfunction $|\Psi_0^\circ\rangle$ for the ground state. Here we use the minimum packet centered at $(q,p) = (0,0)$ as the absorber. Figures A.8(a) and (b) show absorbed eigenstates in q- and p-representation. The amplitude in the q-representation around $q = 0$ drops to a certain value with increase in the absorbing strength Γ. Even if $\Gamma = 2$, the amplitude $q = 0$ does not vanish. This is also due to the representation problem as discussed in the previous section A.1. Therefore, the overlap with the absorber $\langle\alpha|\Psi_0^\circ\rangle$ drops to zero when $\Gamma = 2$ as shown in Fig A.8(c). Besides, as shown in Fig. A.9, the difference of wave functions defined by Eq. (A.13) shows that the absorber effect well localizes on around $(q,p) = (0,0)$ compared with the delta function absorber.

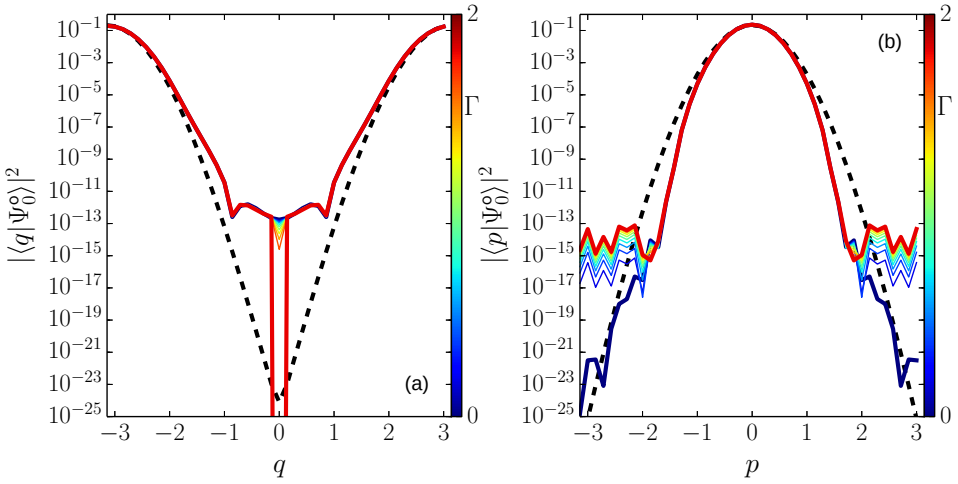

Figure A.6: The absorbed eigenfunction for the ground state $|\Psi_0^\circ\rangle$ in (a) q-representation and in (b) p-representation. Each colored curve distinguishes the absorbing strength Γ (see the right-hand color bar). Here we use the delta function $\langle q|\alpha\rangle = \delta(q)$ as the absorber.

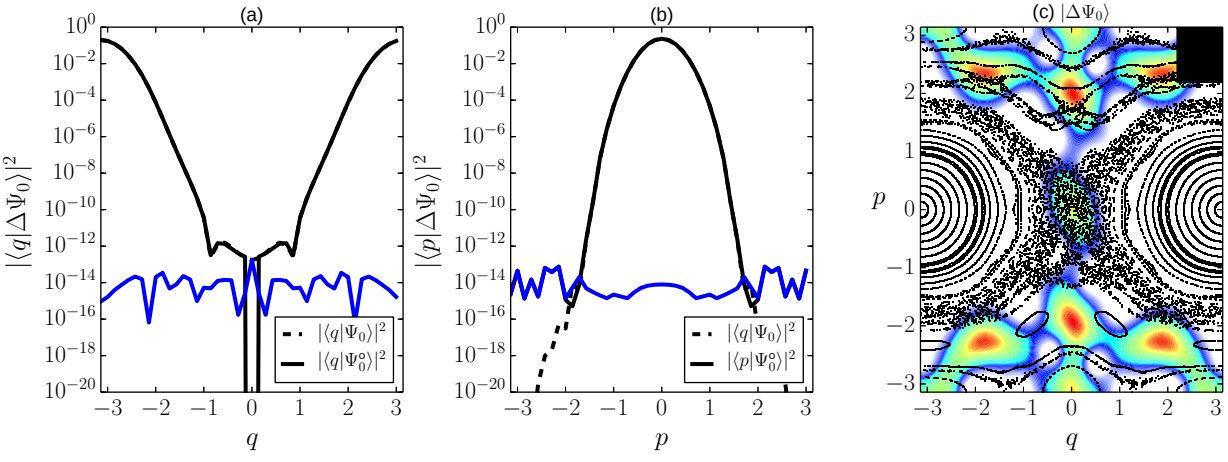

Figure A.7: The difference $|\Delta\Psi_0\rangle$ of the wave functions in (a) q-representation, (b) the p-representation, and (c) Husimi-representation. Here we use the delta function $\langle q|\alpha\rangle = \delta(q)$ as the absorber.

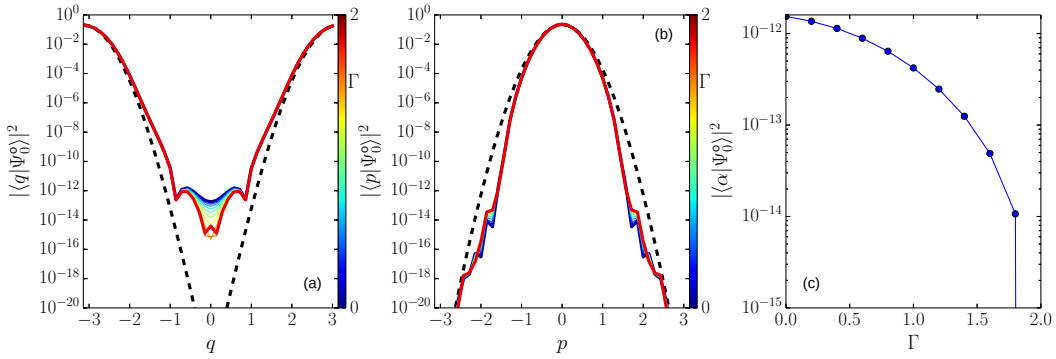

Figure A.8: The absorbed eigenfunctions for the ground state $|\Psi_0^\circ\rangle$ in (a) q-representation and (b) p-representation. The each colored curve distinguishes the absorbing strength Γ (see the right-hand color bar). (c) The overlapping amplitude with absorber α as a function of Γ. Here we use the minimum packet centered at $(q_c, p_c) = (0, 0)$ as the absorber.

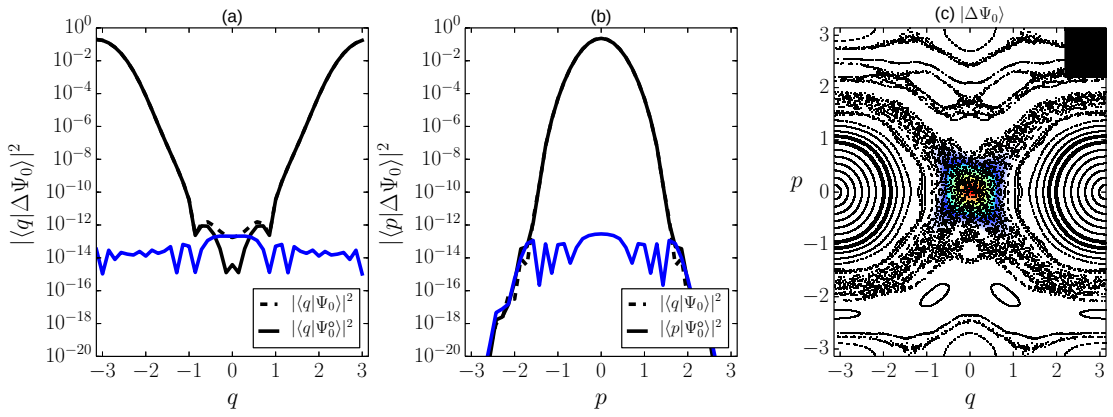

Figure A.9: The difference $|\Delta\Psi_0\rangle$ of wave functions in (a) q-representation, (b) p-representation, and (c) Husimi-representation. Here we use the minimum packet centered at $(q_c, p_c) = (0, 0)$ as the absorber.

A.3 The relation between the decay rate and tunneling splitting

The decay rate γ_n which is defined by the absorbing operator, has been studied intensively in the Dresden group [Bäcker et al. 2010, Löck 2009, Löck et al. 2010, Mertig 2013] and they adopt the decay rate γ_n as a definition of the tunneling rate. As discussed in section 5.2.1, the decay rate γ_n depends strongly on the position and the shape of the absorber. In this sense, the decay rate γ_n would not be a canonical observable for the tunneling probability. However, as we discussed in the previous sections, the tunneling splitting ΔE_n is correlated with the amplitude at the position between symmetric wells, *i.e.*, $q = 0$. So if we introduce the delta function type absorber $\langle q|\alpha\rangle = \delta(q)$, the decay rate γ_n could become comparable to the splitting ΔE_0.

As discussed in section 3.1, the tunneling splitting ΔE_n correlates with the amplitude $\langle q|\Psi_n^+\rangle$ at $q = 0$. Besides, the decay rate γ_0 is determined by Eq. (5.16). If we use the delta function $\langle q|\alpha\rangle = \delta(q)$ at $q = 0$ as the absorber, the decay rate γ_n may become comparable to the splitting ΔE_n *i.e.*,

$$\gamma_n \sim |\Delta E_n|. \tag{A.14}$$

A good agreement between the splitting ΔE_0 and the decay rate γ_0 and the robustness property of the decay rate against the position of the absorber was demonstrated in Chapter 3 of Ref. [Mertig 2013], as far as the absorber is placed on the chaotic sea. However, such stability against the shift of the absorber position is not guaranteed and is gradually broken as the position of the absorber approaches the tours region; the decay rate γ_0 becomes greater than the splitting, $\gamma > |\Delta E_0|$, especially for the large $\hbar$ regime. It is probably because the absorber touches the exponential decaying tail of $\langle q|\Psi_n\rangle$ and the decay rate $\gamma_n \sim \sum_\ell \langle \alpha_\ell|\Psi_n\rangle$ grows. In any case, the delta function-type absorber induces the diffractive propagation along the p-direction. Therefore, it is necessary to make a careful consideration and prepare a proper absorber in order to detect tunneling effects as purely as possible.

Since our result presented above suggests that the minimum packet is better than the delta function as the absorber and can suppress anomalous effects induced by diffraction. However, as shown below, the minimum packet is not the best absorber for the study of the splitting. We here explain why it is so. Figures A.10(a) and (b) we draw the eigenvalues of the unitary case ($\Gamma = 0$) and non-unitary case ($\Gamma = 1$) respectively. In this example, we use the absorber $|\alpha\rangle$ as a minimum packet (A.10) centered at $(q, p) = (0, 0)$. All of the eigenvalues of $\hat{U}$ are located on the unit circle as expected. For descriptive

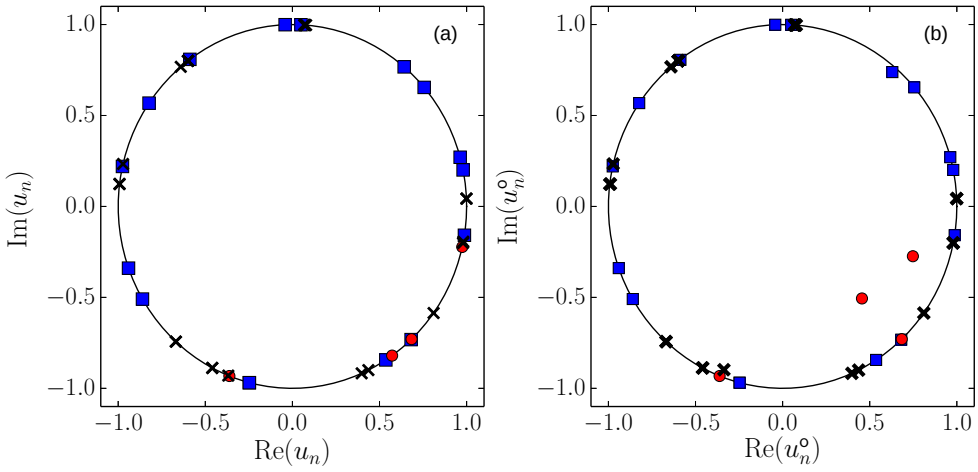

Figure A.10: (a) The eigenvalues of the unitary quantum map $\hat{U}$ with $h = 4\pi^2/44$ are located on the unitary circle. The state localized on the elliptic tours around $(q,p) = (\pm\pi, 0)$ and around the chaotic region $(q,p) = (0,0)$ is marked by the blue square mark, and red dot mark. The state localized on the transversal tours region is marked by black crosses. (b) The eigenvalues of the absorbed quantum map $\hat{U}^\circ$ are located inside the unit circle. Here we use the minimum packet centered at $(q_c, p_c) = (0,0)$ as the absorber.

purposes, we roughly classify the eigenvalues into 3 groups: the eigenstates localizing on (square blue mark) the elliptic tours region around $(q,p) = (\pm\pi, 0)$, (red dot mark) the chaotic region around $(q,p) = (0,0)$ and (black cross mark) the transversal tours region. We note that several eigenvalues of $\hat{U}^\circ$ are located inside the unit circle, which means that the effects of the spread over a large region compared with Fig. 5.5 As we can see from Fig. A.10(b), the most affected eigenvalue is the red dot marked one whose state is close to the absorber at $(q,p) = (0,0)$. We notice that some of the red dot marks are located on the unit circle. This is because the overlap with absorber $\langle a|\Psi_n\rangle$ is zero due to the symmetry.

Next we consider the splitting behavior by introducing the absorbing operator for which we use the absorber $|\alpha\rangle$ as the minimum packet (A.10) centered at $(q,p) = (0,0)$. Figure A.11 shows the behavior of the real and imaginary part of the splitting. Note that the absorber $|\alpha\rangle$ has an effect on the several states which have the same symmetry as that of the ground state $|\Psi_0^+\rangle$. When observing the splitting, we can find that a specific spike disappears in the real part of the splitting curve. Such a spike is indicated as the black arrow in Fig. A.11(b). This is exactly because the absorber suppresses the energy level resonance with third state which is localized on $(q,p) = (0,0)$ in this case. However, the minimum packet is not suitable for the study of the splitting for the reason stated below.

Figure A.11(c) shows the splitting curves drawn in the complex energy plain. The imaginary part of the splitting is roughly fitted by the exponential decay until $1/h \sim 1$, then it switches to the splitting curve of the unitary case (see black curve in Fig. A.11). This behavior is easily understood by recalling the relation (5.16). Since the absorber has only an effect on $|\Psi_0^+\rangle$, the imaginary part of energy is evaluated as $\tilde{E}_0^{\mathsf{im}} = \frac{\hbar}{2\tau}\gamma_0 \sim \frac{\hbar}{2\tau}\Gamma\langle\alpha|\Psi_0^+\rangle$. In a small $1/h$ regime, the variance of the Gaussian for the absorber $|\alpha\rangle$ is large. The ground state $|\Psi_0^+\rangle$ has also a large variance, so the overlap $\langle\alpha|\Psi_0^+\rangle$ is quite large. Therefore, the imaginary part or the decay rate overwhelms the splitting:

$$\gamma_n \sim |\langle\alpha|\Psi_0^+\rangle|^2 > |\langle q|\Psi_0^+\rangle|^2_{q=0} \sim |\Delta E_0|. \tag{A.15}$$

As $1/h$ becomes large, the absorber $|\alpha\rangle$ becomes much narrower, so the overlap between the absorber and ground state is comparable in its magnitude to the amplitude at $q = 0$, *i.e.*, $|\langle\alpha|\Psi_0^+\rangle|^2 \sim |\langle q|\Psi_0^+\rangle|^2_{q=0}$. Hence, the imaginary part of the splitting curve follows the splitting curve of the unitary case. The relation $\gamma_n > |\Delta E_n|$ implies that the wave function decays faster than characteristic tunneling time $T = \hbar/\Delta E$. In other words, the splitting curve in Figs. A.11(c) or (d) shows a crossover from the region determined by the decaying rate to that reflecting the tunneling splitting, each of which has an entirely different origin. Therefore, the absorber should be introduced to satisfy the condition $\gamma_n \leq |\Delta E_n|$.

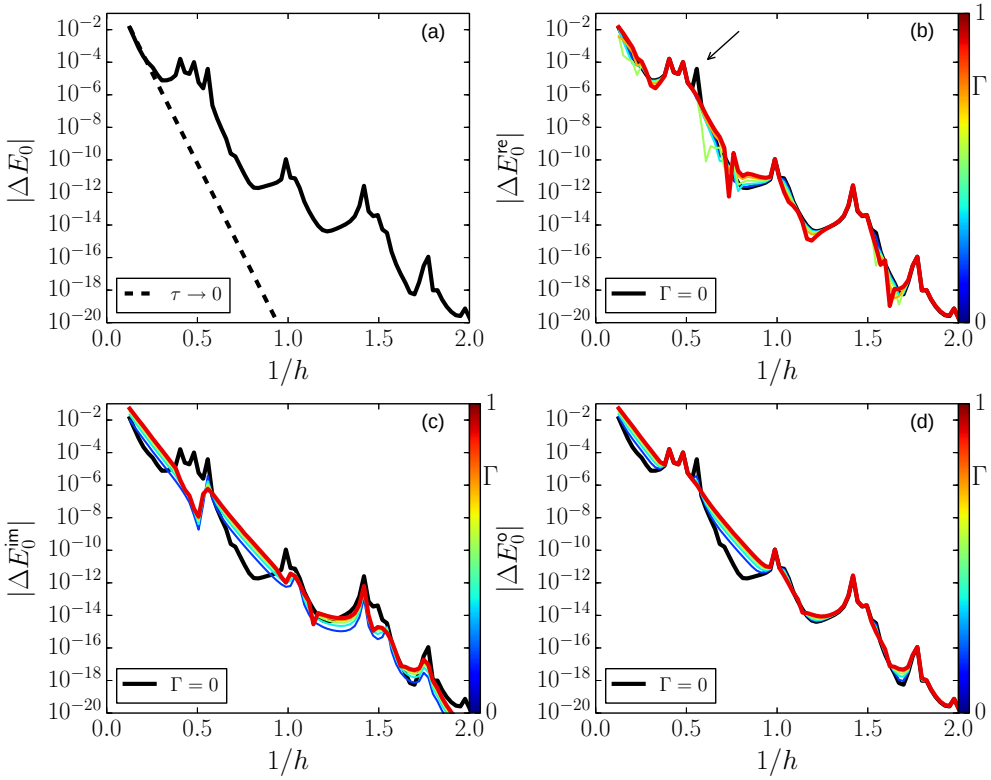

Figure A.11: The energy splitting of the ground state $(n = 0)$ as a function of the inverse Planck's constant $1/h$ (a) for the unitary case (black curve) and for its integrable approximation (dashed line). In the absorbed case $(\Gamma > 0)$, each panel shows the (b) real part distance $|\tilde{E}_0^{\mathsf{re},+} - \tilde{E}_0^{\mathsf{re},-}|$ defined by Eq. (5.15) (c) imaginary part distance $|\tilde{E}_0^{\mathsf{im},+} - \tilde{E}_0^{\mathsf{im},-}|$, and (d) distance in the complex domain. Each colored curve distinguishes the absorbing strength Γ (see the right-hand color bar). For the reference, in the panels (c) and (d) the splitting curves in the non-unitary case (black solid curve) are drawn.

Appendix B

Symplectic integrator for Hamiltonian systems

The development of numerical methods to solve ordinary differential equation has a long history [Hairer et al.]. In this appendix, we review the numerical integration scheme referred to as the symplectic integrator. We consider the one-dimensional Hamiltonian in the following form

$$H(q,p) = T(p) + V(q). \tag{B.1}$$

Using the Poisson bracket, the Hamilton's equations of motion are written as

$$\frac{d}{dt}z = \{z, H\}, \tag{B.2}$$

where we write a set of canonical variable as $z = (p, q)$. Here, we introduce a differential operator $\mathcal{D}_H$ defined by $\mathcal{D}_H z \equiv \{z, H\}$, and write the Hamilton's equations as

$$\frac{d}{dt}z = \mathcal{D}_H z. \tag{B.3}$$

The formal (exact) solution $z(t)$ from $t = 0$ to $t = \tau$ is given by

$$z(\tau) = e^{\tau \mathcal{D}_H} z(0). \tag{B.4}$$

For the Hamiltonian of the form (B.1), $\mathcal{D}_H = \mathcal{D}_T + \mathcal{D}_V$, and $\mathcal{D}_T$, $\mathcal{D}_V$ do not commute with each other. Here the $\mathcal{D}_T$ and $\mathcal{D}_V$ are respectively defined by using Poisson bracket $\mathcal{D}_T z \equiv \{z, T\}$ and $\mathcal{D}_V z \equiv \{z, V\}$. The so-called 1st order (Euler) symplectic integrator (scheme) [Vogelaere 1956]

$$p_{n+1} = p_n - \tau \frac{dT(p_n)}{dp}, \quad q_{n+1} = q_n + \tau \frac{dV(q_{n+1})}{dq}, \tag{B.5}$$

coincides with the Taylor expansion of the exact flow up to the 1st order of τ. Note that the map (B.5) conserves the symplectic structure $dp_{n+1} \wedge dq_{n+1} = dp_n \wedge dq_n$. We notice that the symplectic integrator (B.5) is is written as a composition of the two trivial symplectic mappings [Yoshida 1993]

$$f_V(c_i\tau): \begin{array}{ll} p' & = p - c_i\tau \frac{dV(q)}{dq}, \\ q' & = q, \end{array} \qquad f_T(d_i\tau): \begin{array}{ll} p' & = p, \\ q' & = q + d_i\tau \frac{dT(p)}{dp}, \end{array} \tag{B.6}$$

i.e., the 1st order symplectic integrator is expressed as $f^{(1)}(\tau) = f_T(\tau) \circ f_V(\tau)$ where the coefficients are $(c_i, d_i) = (1, 1)$. Using a differential operators $\mathcal{D}_T$ and $\mathcal{D}_V$ the trivial symplectic mappings are expressed as

$$\begin{aligned} f_V(c\tau) : z' &= (\mathbb{1} + c_i\tau\mathcal{D}_V)z \qquad & f_T(d_i\tau) : z' &= (\mathbb{1} + d_i\tau\mathcal{D}_T)z \\ &= e^{c_i\tau\mathcal{D}_V} z, & &= e^{d_i\tau\mathcal{D}_T} z. \end{aligned} \tag{B.7}$$

Here $\mathbb{1}$ denotes the identity matrix. Note that ${\mathcal{D}_T}^2 z = {\mathcal{D}_\mathcal{V}}^2 z = 0$. Thus the 1st order symplectic integrator is related with the exact Hamiltonian flow as

$$e^{\tau(\mathcal{D}_T + \mathcal{D}_V)} = e^{\tau\mathcal{D}_T} e^{\tau\mathcal{D}_V} + o(\tau^2). \tag{B.8}$$

The 2nd order symplectic integrator [Störmer 1907, Verlet 1967] is given as $f^{(2)}(\tau) \equiv f_V(\frac{\tau}{2}) \circ f_T(\tau) \circ f_V(\frac{\tau}{2})$, which corresponds to the exact Hamiltonian flow up to the second order Taylor expansion

$$e^{\tau(\mathcal{D}_T + \mathcal{D}_V)} = e^{\frac{\tau}{2}\mathcal{D}_V} e^{\tau\mathcal{D}_T} e^{\frac{\tau}{2}\mathcal{D}_V} + o(\tau^3). \tag{B.9}$$

In general, the n-th order symplectic integrator can be expressed as a product of the trivial symplectic

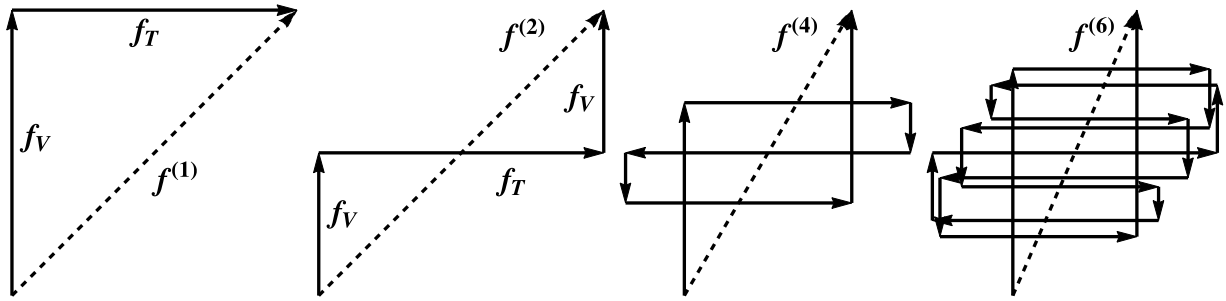

Figure B.1: The schematic images of symplectic integrators. The vertical and horizontal arrows denote the time evolution with f_V and f_T, respectively. The dashed arrows denotes the time evolution of the n-th order symplectic integrator. The down-arrows and the left-arrows imply the backwards time evolution.

mappings

$$e^{\tau(\mathcal{D}_T+\mathcal{D}_V)} = \prod_{i=1}^{n} e^{c_i,\tau\mathcal{D}_T} e^{d_i\tau\mathcal{D}_V} + o(\tau^{n+1}). \tag{B.10}$$

Moreover, [Yoshida 1990] pointed out that the higher order symplectic integrator is given as a composition of the lower order ones; the $(2n+2)$-th order symplectic integrator can be written as

$$f^{(2n+2)}(\tau) = f^{(2n)}(x_1\tau) \circ f^{(2n)}(x_0\tau) \circ f^{(2n)}(x_1\tau), \tag{B.11}$$

where the coefficients were derived as

$$x_0 = \frac{-2^{1/2n+1}}{2-2^{1/2n+1}}, \qquad x_1 = \frac{1}{2-2^{1/2n+1}}. \tag{B.12}$$

In this way, we can easily construct the higher order integration scheme to solve the Hamiltonian equations of motion. Figure B.1 shows the schematic images of the time evolution of the n-th order symplectic integrator.

Although the symplectic integrators do not conserve the original Hamiltonian H at each step, the error does not grow secularly as long as $\tau \ll 1$ [Yoshida 1993]. This behavior can be explained by the fact that the symplectic integrator exactly describes the τ time step evolution of an associated perturbed (shadow) Hamiltonian $H_{\rm eff}$ [Yoshida 1993], which is close to the original Hamiltonian H. By applying the Baker-Campbell-Hausdorff (BCH) formula, we can express the 1st order symplectic integrator as

$$\exp(\tau\mathcal{D}_T)\exp(\tau\mathcal{D}_V) = \exp\tau D_{H_{\rm eff}}. \tag{B.13}$$

Here the associated perturbed Hamiltonian H_{eff} is expressed as a formal power series in τ

$$H_{\text{eff}} = H_1 + \tau H_2 + \tau^2 H_3 + \tau^3 H_4 + \cdots , \tag{B.14}$$

where the each H_j comes from the BCH formula

$$H_1 = T + V, \qquad H_2 = \frac{1}{2}\{V, T\}, \qquad H_3 = \frac{1}{12}\Big(\{\{T, V\}, V\} + \{\{V, T\}, T\}\Big), \quad \cdots . \tag{B.15}$$

In particular, the symplectic integrator (B.5) exactly follows the dynamics of H_{eff} in Eq. (B.14). However, the series (B.14) diverges in general, so the H_{eff} does not a conserved quantity [Kobayashi 2007, Suzuki 1994, Yoshida 1993; 2001]. Even so, the higher order effective integrable (BCH) Hamiltonian

$$H_{\text{eff}}^{(M)} = \sum_{j=1}^{M} \tau^{j-1} H_j, \tag{B.16}$$

in which the expansion is truncated at the order M, whose terms consist of up to the order M and higher terms are neglected, provides an approximation for the symplectic integrator (B.5).

As can be seen from the Eq. (B.14), for large τ, the associated perturbed Hamiltonian $H_{\text{eff}}^{(M)}$ is not close to the original Hamiltonian. Moreover, the symplectic integrators generate chaotic orbits, which cannot be generated by the finite series (B.16) since $H_{\text{eff}}^{(M)}$ is completely integrable. For example, let us consider the simple pendulum Hamiltonian

$$H(q, p) = \frac{p^2}{2} + k \cos q. \tag{B.17}$$

The 1st order symplectic integrator is given as

$$p_{n+1} = p_n + k\tau \sin q_n, \qquad q_{n+1} = q_n + \tau p_{n+1}. \tag{B.18}$$

This map is equivalent to the standard map as discussed in section 2.2.

Figure B.2 shows the phase space portrait for the standard map and the contour curves of the higher order effective integrable (BCH) Hamiltonian $H_{\text{eff}}^{(M)}$ defined by Eq. (B.16). Here we take the parameter $\tau = 1$ and $M = 7$. As shown in Fig. B.2(b1), the effective integrable Hamiltonian $H_{\text{eff}}^{(M)}$ well approximates the phase space portrait of the standard map. However, the effective integrable Hamiltonian $H_{\text{eff}}^{(M)}$ cannot reproduce

chaotic orbits or classical resonances. This discrepancy becomes larger with increase in k.

We also notice that the quantum map corresponding to the 1st order classical map could be expanded by using BCH formula

$$\hat{U} = \exp\left(-\frac{i}{\hbar}\tau\hat{T}(\hat{p})\right)\exp\left(-\frac{i}{\hbar}\tau\hat{V}(\hat{q})\right) = \exp\left(-\frac{i}{\hbar}\tau\hat{H}_{\rm eff}\right). \tag{B.19}$$

Here the associated perturbed Hamiltonian $\hat{H}_{\rm eff}$ is expressed as

$$\hat{H}_{\rm eff} = \hat{H}_1 + \left(-\frac{i\tau}{\hbar}\right)\hat{H}_2 + \left(-\frac{i\tau}{\hbar}\right)^2\hat{H}_3 + \cdots, \tag{B.20}$$

where the each $\hat{H}_j$ is determined by the BCH formula. The quantum version of the higher order effective integrable Hamiltonian

$$\hat{H}_{\rm eff}^{(M)} = \sum_{j=1}^{M}\left(-\frac{i\tau}{\hbar}\right)^{j-1}\hat{H}_j, \tag{B.21}$$

also provides an approximation for the quantum map.

To demonstrate this, let us consider the eigenvalues problem for the standard map ($T(p) = p^2/2, V(q) = k\cos q$) and associated integrable approximation

$$\hat{U}|\Psi_n\rangle = u_n|\Psi_n\rangle, \qquad \hat{H}_{\rm eff}^{(M)}|J_n^{(M)}\rangle = E_n^{(M)}|J_n^{(M)}\rangle. \tag{B.22}$$

Figure B.3 shows the Hurimi-representation of the eigenstate $|\Psi_n\rangle$ and the eigenstates $|J_n^{(M)}\rangle$ of the the associated effective integrable Hamiltonian. As shown in Fig. B.3(a1) and (b1), the eigenstate localizing on KAM curve are well approximated by the associated integrable eigenstates $|J_n^{(M)}\rangle$. On the other hand, the eigenstate $|\Psi_n\rangle$ localizing on the classical resonance cannot be represented by integrable eigenstate $|J_n^{(M)}\rangle$. This is because the effective integrable Hamiltonian $\hat{H}_{\rm eff}^{(M)}$ does not incorporate the classical resonances or chaotic motions and. The situation is the same as the classical one.

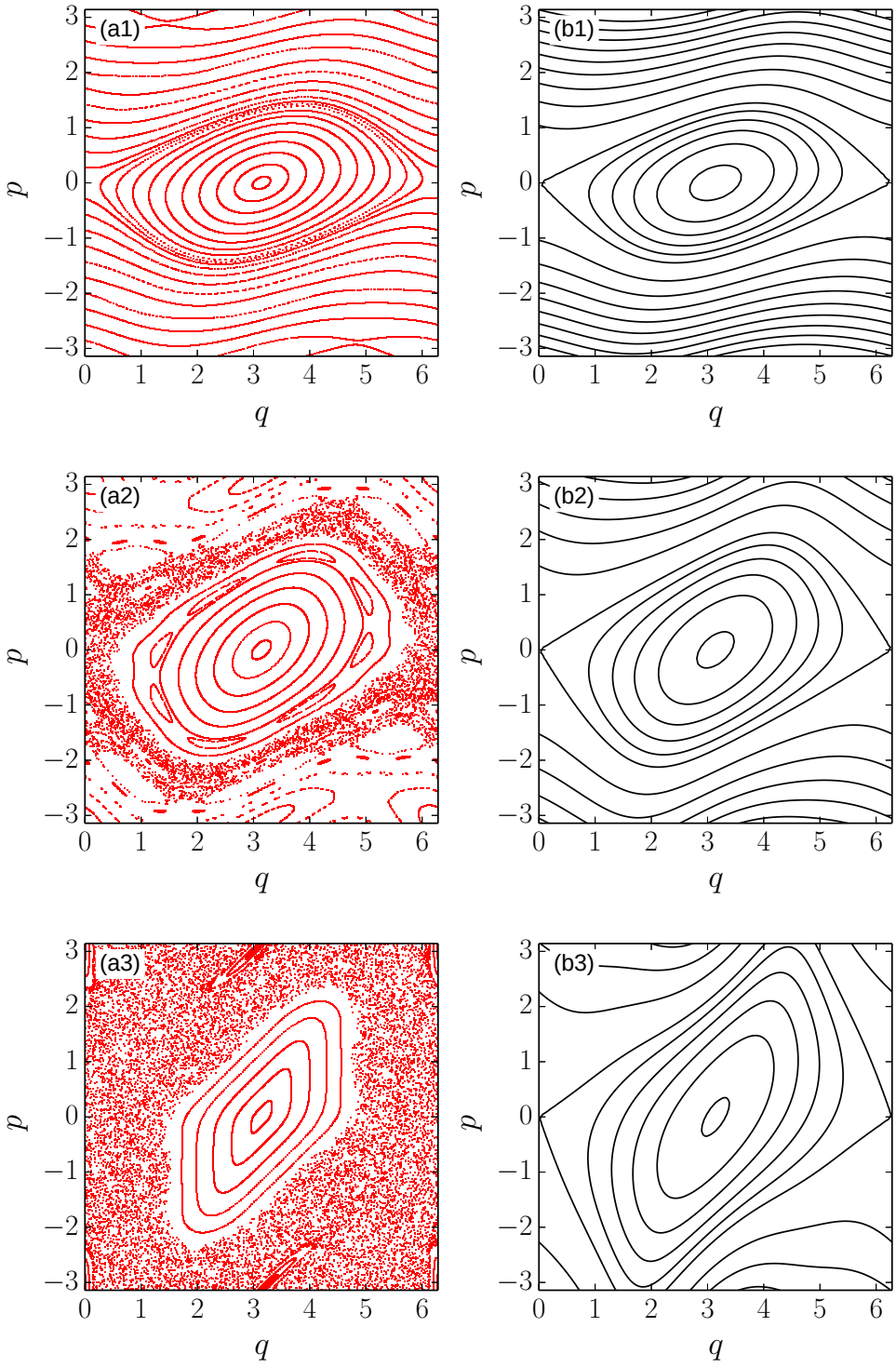

Figure B.2: Classical phase space for the standard map (B.18) with (a1) $k = 1/2$, (a2) $k = 1$ and (a3) $k = 2$ and the contour curves of the effective integrable Hamiltonian $H_{\rm eff}^{(M)}$ with (b1) $k = 1/2$, (b2) $k = 1$ and (b3) $k = 2$. Here we use the parameter $\tau = 1$ and $M = 7$.

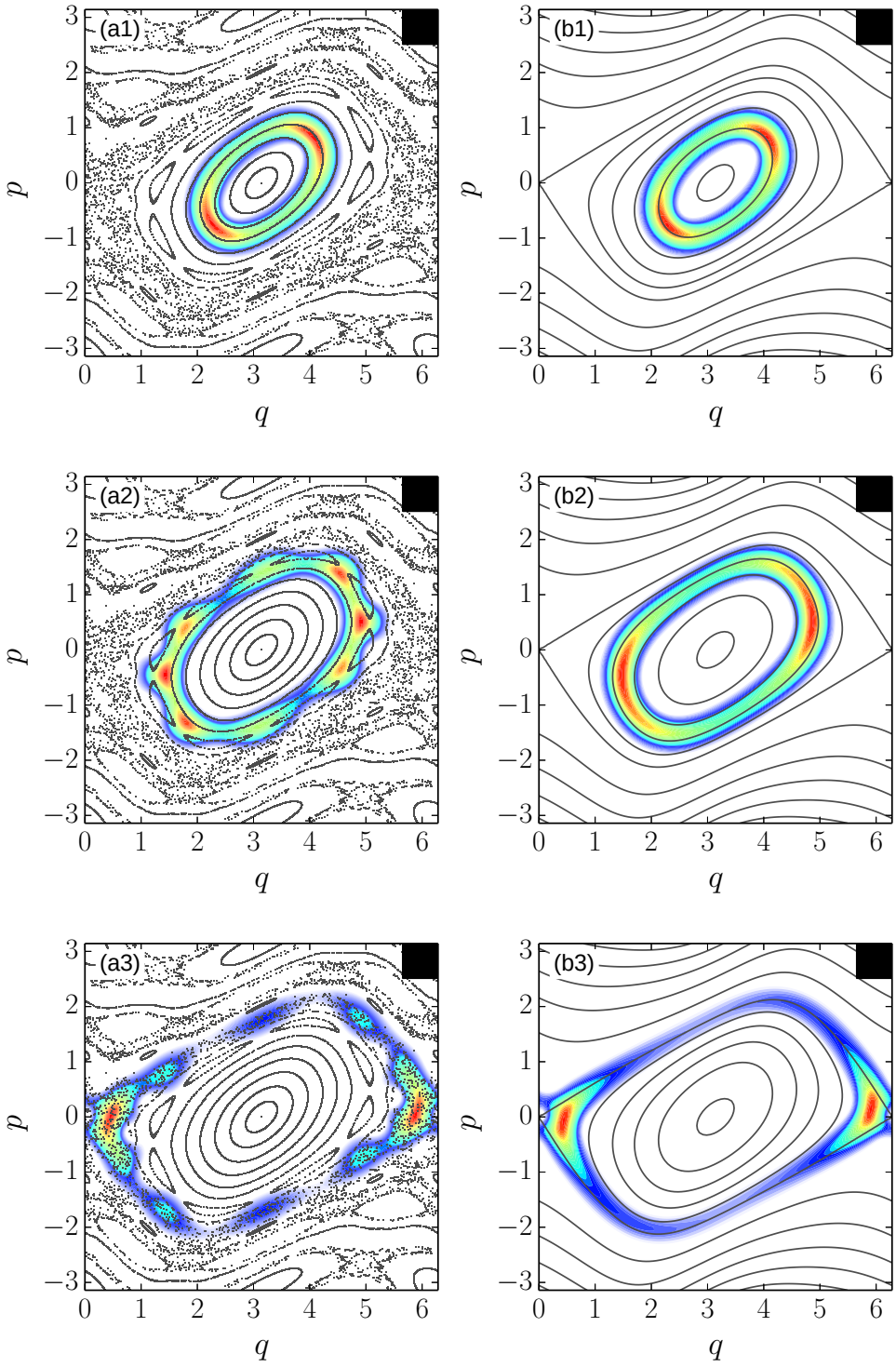

Figure B.3: The Husimi-representation of the eigenstate $|\Psi_n\rangle$ for the quantized standard map with (a1) $n = 7$, (a2) $n = 18$ and (a3) $n = 39$. The right panels shows the Husimi-representation of the eigenstate for the 7-th order effective integrable Hamiltonian with (b1) $n = 7$, (b2) $n = 18$ and (b3) $n = 39$. Upper right boxes represents the size of effective Planck's cell h.

Acknowledgements

I would like to express my sincere thanks to my supervisor Professor Akira Shudo for providing me with the opportunity to write PhD. thesis. I am truly grateful for his cordial supports and all aspects of help during the course of PhD. student. I am grateful to Professor T. Hotta, Professor H. Mori, and Professor E. Arahata for careful reading of this thesis.

I would like to thank present members of Nonlinear Physics Group, Mr. H. Harada, Ms. R. Ohashi, Mr. K. Aoki, Mr. K. Yoshida and Mr. S. Sugawara, for numerous discussion and their kindness. Especially, I am grateful to Dr. A. Tanaka for fruitful discussion on quantum mechanics and for advice on numerical computations. I especially thank Dr. N. Mertig for his helpful comments and fruitful discussion on tunneling. I am grateful to Professor N. Fuchigami for insightful comments in our group seminar. I also would like to thank the past members of our group, especially, Dr. T. Onishi, Dr. T. Okushima, Dr. A. Akaishi and Dr. A. Ishikawa, Mr. K. Tanaka, Mr. Y. Uno, Mr. M. Kanai, Mr. A. Ishii, Mr. Y. Hodoshima, Ms. Y. Sugiyama and Mr. I. Maeda, for stimulating discussions.

I would like to thank Professor K. S. Ikeda, Mr. T. Oya and Mr. F. Matsui for fruitful discussion on tunneling and quantum chaos. I am grateful to Professor Y. Aizawa and his group members, especially, Professor T. Miyaguchi, Dr. T. Akimoto, Dr. S. Shinkai, Dr. T. Mitsui Dr. M. Nakagawa, Dr. M. Shiraishi and Dr. S. Tugawa for stimulating discussion and their kind hospitality in several conferences. I would like to thank my colleagues, especially, Dr. N. Watanabe, Dr. R. Miyazaki and Dr. T. Shimizu, for the encouragement. Finally, I thank my parents for continuing support and understanding.

Bibliography

V. I. Arnold. *Mathematical Methods of Classical Mechanics*. Springer, 2nd edition. 1997.

S. Aubry. "The New Concept of Transitions by Breaking of Analyticity in a Crystallographic Model". In A.R.Bishop T. Schneider, editor, *Solitons and Condensed Matter Physics*, Springer Series in Solid-State Sciences, page 264. Springer Berlin Heidelberg, 1978.

A. Bäcker, R. Ketzmerick, and S. Löck. "Direct regular-to-chaotic tunneling rates using the fictitious-integrable-system approach". *Physical Review E*, **82** page 056208, 2010.

A. Berretti and L. Chierchia. "On the complex analytic structure of the golden invariant curve for the standard map". *Nonlinearity*, **3** page 39, 1990.

A. Berretti, A. Celletti, L. Chierchia, and C. Falcolini. "Natural boundaries for area-preserving twist maps". *Journal of Statistical Physics*, **66** page 1613, 1992.

M. V. Berry. "Regular and irregular semiclassical wavefunctions". *Journal of Physics A*, **10** page 2083, 1977.

M. V Berry, N. L Balazs, M Tabor, and A Voros. "Quantum maps". *Annals of Physics*, **122** page 26, 1979.

O. Bohigas, S. Tomsovic, and D. Ullmo. "Classical transport effects on chaotic levels". *Physical Review Letters*, **65** page 5, 1990.

O. Bohigas, D. Boosé, R. E. de Carvalho, and V. Marvulle. "Quantum tunneling and chaotic dynamics". *Nucl. Phys. A*, **560** page 197, 1993a.

O. Bohigas, S. Tomsovic, and D. Ullmo. "Manifestations of classical phase space structures in quantum mechanics". *Physics Reports*, **223** page 43, 1993b.

L. Bonci, A. Farusi, P. Grigolini, and R. Roncaglia. "Tunneling rate fluctuations induced by nonlinear resonances: A quantitative treatment based on semiclassical arguments". *Physical Review E*, **58** page 5689, 1998.

O. Brodier, P. Schlagheck, and D. Ullmo. "Resonance-Assisted Tunneling in Near-Integrable Systems". *Physical Review Letters*, **87** page 064101, 2001.

O. Brodier, P. Schlagheck, and D. Ullmo. "Resonance-Assisted Tunneling". *Annals of Physics*, **300** page 88, 2002.

G. Casati, B. V. Chirikov, F. M. Izraelev, and J. Ford. *"Stochastic Behavior of A Quantum Pendulum Under A Periodic Perturbation"*, volume 93 of *Lecture Notes in Physics*. Springer-Verlag, Berlin/Heidelberg, 1979.

B. V. Chirikov. "Research concerning the theory of nonlinear resonance and stochasticity". *Institute of Nuclear Physics, Novosibirsk*, 1969.

B. V. Chirikov. "A universal instability of many-dimensional oscillator systems". *Physics Reports*, **52** page 263, 1979.

S. Coleman. "The uses of instanton". In *Aspect of Symmetry*, chapter 7, page 265. Cambridge University Press, 1988.

S. C. Creagh. "Tunneling in two dimensions". In S. Tomsovic, editor, *Tunneling in complex systems*, page 35. World Scientific, 1998.

M. J. Davis and E. J. Heller. "Quantum dynamical tunneling in bound states". *The Journal of Chemical Physics*, **75** page 246, 1981.

C. Eltschka and P. Schlagheck. "Resonance- and Chaos-Assisted Tunneling in Mixed Regular-Chaotic Systems". *Physical Review Letters*, **94** page 014101, 2005.

R. P. Feynman and A. R. Hibbs. *Quantum Mechanics and Path Integrals*. McGraw-Hill Companies, New York. 1965.

J. M. Greene. "A method for determining a stochastic transition". *Journal of Mathematical Physics*, **20** page 1183, 1979.

J. M. Greene and I. C. Percival. “Hamiltonian maps in the complex plane”. *Physica D*, **3** page 530, 1981.

F. Haake. *Quantum Signatures of Chaos*. Springer-Verlag, 3rd edition. 2010.

E. Hairer, C. Lubich, and G. Wanner. *Geometric Numerical Integration: Structure-Preserving Algorithms for Ordinary Differential Equations*. Springer, Heidelberg ; New York, 2nd edition. 2010.

Y. Hanada, A. Shudo, and K. S. Ikeda. “Origin of the enhancement of tunneling probability in the nearly integrable system”. submitted to Physical Reviews E.

Y. Hanada, A. Shudo, and K. S. Ikeda, in preparation.

H. Harada and A. Shudo, private communications.

H. Harada and A. Shudo. “Non-linear resonances and singularity structures of complex classical dynamics”. *Advances in Science, Technology and Environmentology. Special issue : ASTE (Waseda University)*, 2015. to be published.

A. Ishikawa, A. Tanaka, K. S. Ikeda, and A. Shudo. “Diffraction and tunneling in systems with mixed phase space”. *Physical Review E*, **86** page 036208, 2012.

L. Kaplan. “Scar and antiscar quantum effects in open chaotic systems”. *Physical Review E*, **59** page 5325, 1999.

J. P. Keating, S. Nonnenmacher, M. Novaes, and M. Sieber. “On the resonance eigenstates of an open quantum baker map”. *Nonlinearity*, **21** page 2591, 2008.

S. Keshavamurthy and P. Schlagheck, editors. *Dynamical Tunneling: Theory and Experiment*. CRC Press, 2011.

Srihari Keshavamurthy. “On dynamical tunneling and classical resonances”. *The Journal of Chemical Physics*, **122** page 114109, 2005.

H. Kobayashi. “Anomaly in symplectic integrator”. *Physics Letters A*, **371** page 360, 2007.

L. D. Landau and E. M. Lifshits. *Quantum mechanics non-relativistic theory*. Butterworth Heinemann. 1977.

J. Le Deunff and A. Mouchet. "Instantons re-examined: Dynamical tunneling and resonant tunneling". *Physical Review E*, **81** page 046205, 2010.

J. Le Deunff, A. Mouchet, and P. Schlagheck. "Semiclassical description of resonance-assisted tunneling in one-dimensional integrable models". *Physical Review E*, **88** page 042927, 2013.

A. J. Lichtenberg and M. A. Lieberman. *Regular and Chaotic Dynamics*. Springer New York, 2nd revised edition. 1992.

W. A. Lin and L. E. Ballentine. "Quantum tunneling and chaos in a driven anharmonic oscillator". *Physical Review Letters*, **65** page 2927, 1990.

D. Lippolis, J.-W. Ryu, S.-Y. Lee, and S. W. Kim. "On-manifold localization in open quantum maps". *Physical Review E*, **86** page 066213, 2012.

S. Löck. *"Dynamical Tunneling in Systems with a Mixed Phase Space"*. PhD thesis, Institut für Theoretische Physik Fachrichtung Physik Fakultät für Mathematik und Naturwissenschaften Technische Universität Dresden, 2009.

S. Löck, A. Bäcker, R. Ketzmerick, and P. Schlagheck. "Regular-to-Chaotic Tunneling Rates: From the Quantum to the Semiclassical Regime". *Physical Review Letters*, **104** page 114101, 2010.

R. S. MacKay. "A renormalization approach to invariant circles in area-preserving maps". *Physica D*, **7** page 283, 1983.

R. S. Mackay, J. D. Meiss, and I.C. Percival. "Transport in Hamiltonian systems". *Physica D*, **13** page 55, 1984.

N. Mertig. *"Complex Paths for Regular-to-Chaotic Tunneling Rates"*. PhD thesis, Institut für Theoretische Physik Fachrichtung Physik Fakultät für Mathematik und Naturwissenschaften Technische Universität Dresden, 2013.

A. Mouchet, C. Eltschka, and P. Schlagheck. "Influence of classical resonances on chaotic tunneling". *Physical Review E*, **74** page 026211, 2006.

T. Onishi, A. Shudo, K. S. Ikeda, and K. Takahashi. "Semiclassical study on tunneling processes via complex-domain chaos". *Physical Review E*, **68** page 056211, 2003.

Y. Onuki and H. Yoshida. *Rikigaku*. Iwanamishoten. 2001. (Japanese)

A. M. Ozorio de Almeida. "Tunneling and the semiclassical spectrum for an isolated classical resonance". *The Journal of Physical Chemistry*, **88** page 6139, 1984.

I. C Percival. "Variational principles for invariant tori and cantori". *AIP Conference Proceedings*, **57** page 302, 1980.

I. C. Percival. "Regular and irregular spectra". *Journal of Physics B*, **6** page L229, 1973.

H. Poincaré. *Les méthodes nouvelles de la mécanique céleste*. Paris : Gauthier-Villars, 1892.

L. E. Reichl. *The Transition to Chaos: Conservative Classical Systems and Quantum Manifestations*. Springer New York, 2nd edition. 2012.

R. Roncaglia, L. Bonci, F. M. Izrailev, B. J. West, and P. Grigolini. "Tunneling versus Chaos in the Kicked Harper Model". *Physical Review Letters*, **73** page 802, 1994.

T. Saito. *Joubibun Houteishiki I*. Iwanamishoten. 1976. (Japanese)

R. Scharf. "The Campbell-Baker-Hausdorff expansion for classical and quantum kicked dynamics". *Journal of Physics A*, **21** page 2007, 1988.

P. Schlagheck, A. Mouchet, and D. Ullmo. "Resonance-Assisted Tunneling in Mixed Regular-Chaotic Systems". In *Dynamical Tunneling: Theory and Experiment*, chapter 8, page 177. CRC Press, 2011.

L. S. Schulman. *Techniques and Applications of Path Integration*. Wiley. 1981.

M. Sheinman, S. Fishman, I. Guarneri, and L. Rebuzzini. "Decay of quantum accelerator modes". *Physical Review A*, **73** page 052110, 2006.

J. R. Shewell. "On the Formation of Quantum-Mechanical Operators". *American Journal of Physics*, **27** page 16, 1959.

R. Shiromoto, A. Shudo, and K. S. Ikeda. unpublished works.

A. Shudo and K. Ikeda. "Toward the Classical Understanding of Quantum Chaological Phenomena". *Progress of Theoretical Physics Supplement*, **116** page 283, 1994.

A. Shudo and K. S. Ikeda. "Complex Classical Trajectories and Chaotic Tunneling". *Physical Review Letters*, **74** page 682, 1995.

A. Shudo and K. S. Ikeda. "Chaotic tunneling: A remarkable manifestation of complex classical dynamics in non-integrable quantum phenomena". *Physica D*, **115** page 234, 1998.

A. Shudo and K. S. Ikeda. "Tunneling Effect and the Natural Boundary of Invariant Tori". *Physical Review Letters*, **109** page 154102, 2012.

A. Shudo, Y. Ishii, and K. S. Ikeda. "Julia sets and chaotic tunneling: I". *Journal of Physics A*, **42** page 265101, 2009a.

A. Shudo, Y. Ishii, and K. S. Ikeda. "Julia sets and chaotic tunneling: II". *Journal of Physics A*, **42** page 265102, 2009b.

A. Shudo, Y. Hanada, T. Okushima, and K. S. Ikeda. "Instanton-noninstanton transition in nonintegrable tunneling processes: A renormalized perturbation approach". *Europhysics Letters*, **108** page 50004, 2014.

A. Shudo, Y. Hanada, T. Okushima, and K. S. Ikeda, in preparation.

C. Störmer. "Sur les trajectoires des corpuscules électrisés". *Arch. sci. phys. nat., Genév*, **24** page 5–18, 113–158, 221–247, 1907.

M. Suzuki. Convergence of general decompositions of exponential operators. *Communications in Mathematical Physics*, **163** page 491, 1994.

M. Tabor. *Chaos and Integrability in Nonlinear Dynamics: An Introduction*. Wiley-Interscience, 1st edition. 1989.

S. Tomsovic and D. Ullmo. "Chaos-assisted tunneling". *Physical Review E*, **50** page 145, 1994.

L. Verlet. "Computer "Experiments" on Classical Fluids. I. Thermodynamical Properties of Lennard-Jones Molecules". *Physical Review*, **159** page 98, 1967.

A. Vibok and G. G. Balint-Kurti. "Parametrization of complex absorbing potentials for time-dependent quantum dynamics". *The Journal of Physical Chemistry*, **96** page 8712, 1992.

R. de Vogelaere. "Method of integration which preserve the contact transformation property of the Hamiltonian equations". *Report No 4, Dept. Math., Univ. of Notre Dame*, 1956.

H. Weyl. *The Theory of Groups and Quantum Mechanics*. Dover Publications, New York. 1950.

M. Wilkinson. "Tunnelling between tori in phase space". *Physica D*, **21** page 341, 1986.

H. Yoshida. "Recent Progress in the Theory and Application of Symplectic Integrators". *Celestial Mechanics and Dynamical Astronomy*, **56** page 27, 1993.

H. Yoshida. "Non-existence of the modified first integral by symplectic integration methods". *Physics Letters A*, **282** page 276, 2001.

H. Yoshida. "Construction of higher order symplectic integrators". *Physics Letters A*, **150** page 262, 1990.